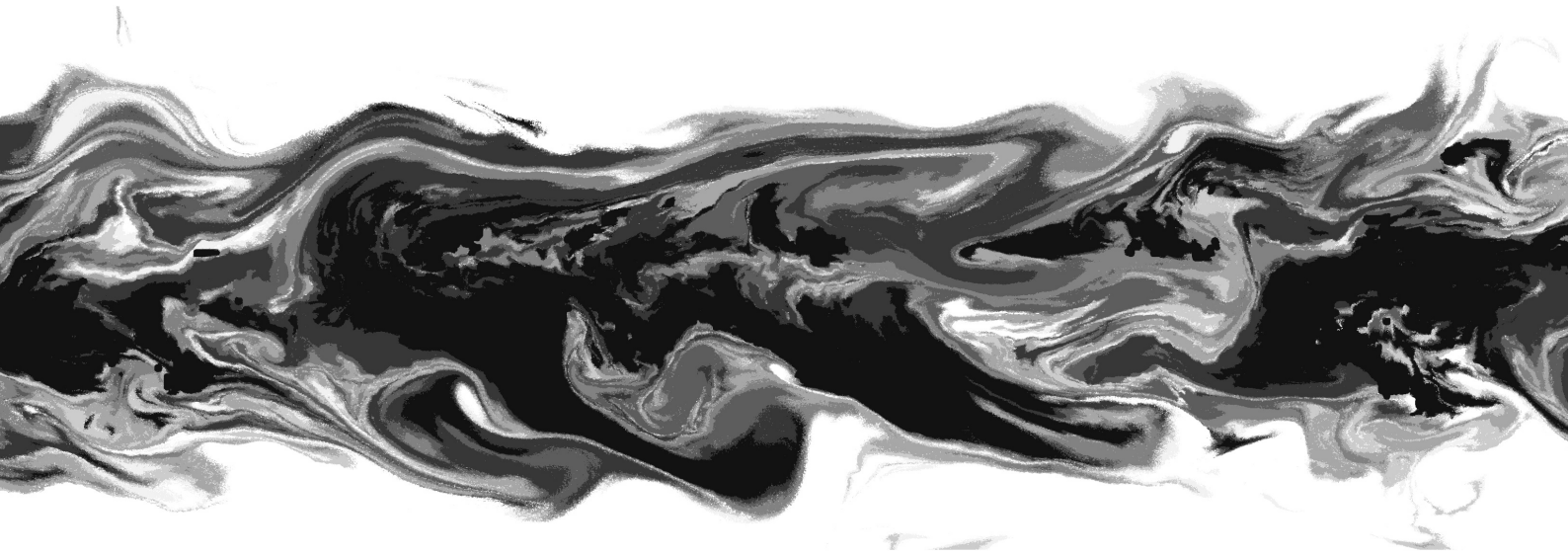
The evolution of cirrus clouds from deep convection

George Horner



Submitted in part fulfilment of the requirements of the degree of Doctor of Philosophy in Physics at the Department of Physics, Imperial College London, August 2024

Supervised by Dr. Edward Gryspeerdt and Prof. Helen Brindley

Abstract

Aerosols significantly impact the climate through their interactions with clouds, where the magnitude and uncertainty of the radiative forcing of aerosol-cloud interactions vary by cloud type. This uncertainty is particularly pronounced for deep convective clouds. Tropical deep convection and its associated cirrus outflows have a near-zero net cloud radiative effect (CRE) due to the offset between shortwave cooling and longwave warming. Therefore, minor changes in the properties of deep convection or associated anvil cirrus, such as those caused by aerosols, could impact the net CRE. Understanding what controls the radiative evolution of deep convection is vital to better constrain aerosol-cloud interactions.

This thesis introduces a novel method to examine the evolution of deep convective clouds, from the short-lived, optically-thick convective cores to the thin detrained cirrus that can persist for days after the initial convection has dissipated. The radiative evolution of clouds along trajectories from deep convection is investigated, revealing a positive total high cloud CRE. The anvil cirrus lifetime is calculated, with longer lifetimes observed for detrained cirrus from oceanic rather than terrestrial convection. Longer lifetimes increase the total high cloud CRE.

It is found that stronger convection produces detrained cirrus with greater warming over their entire lifetime, primarily driven by changes in the SW CRE due to diurnal variability in convection. Finally, the sensitivity of the detrained cirrus CRE to the convective strength is linked to the sensitivity of the high cloud top pressure to the aerosol optical depth, accounting for the non-local impact aerosols may have on detrained cirrus some distance away from the initial convection. This thesis provides an upper bound on aerosol impacts on tropical high cloud CRE. By introducing a novel equation to quantify non-local aerosol effects, it provides a framework for assessing such impacts under various scenarios, enhancing our understanding of aerosol-cloud interactions.

Acknowledgements

This thesis wouldn't have been possible without the help and support of a great many people. Firstly, I would like to thank my supervisor, Ed Gryspeerdt, for his guidance and tireless enthusiasm over the past few years. His passion for science is infectious, and I have learnt so much from him. I would also like to thank Helen Brindley for her co-supervision.

I would also like to say thank you to all my colleagues in the department, past and present. In particular, I would like to thank Anna and Oli for always saying yes to the pub after a long day in the office, to Rebecca, with whom I shared my entire PhD journey, and to Goeff and Sophie. Thank you to the other office, Liam, Sanjee, Michaela, and Jamie, for some great lunchtime conversations. Finally, thank you to Marie and Laura, who provided lots of support when I was just starting my PhD.

Thank you to my flatmates, Jack, Molly, and Finley, for all their support, friendship, and laughs over the past four years. Thank you also to my surrogate flatmates, Lara, Luke, Sam, and Emma, for adopting me into their flat and providing me with many lovely dinners.

Thank you to my friends, in particular Uri, Nick, Alex, Cassie, Jamie, Flossie, Biz, Lara, and Kate, for all the welcome distractions from my PhD - many of which occurred via group chats, when I should have been working.

Thank you to my family for always supporting and encouraging me, not just throughout my PhD, but in all my endeavours. Finally, thank you to Sarah. Without her support, writing this thesis would have been a lot more difficult.

Statement of Originality

The following thesis is the product of my own research. All results or information taken from other work has been acknowledged and referenced appropriately.

Copyright Declaration

The copyright of this thesis rests with the author. Unless otherwise indicated, its contents are licensed under a Creative Commons Attribution-Non Commercial 4.0 International License (CC BY-NC). Under this license, you may copy and redistribute the material in any medium or format. You may also create and distribute modified versions of the work. This is on the condition that: you credit the author and do not use it, or any derivative works, for commercial purpose. When reusing or sharing this work, ensure you make the licence terms clear to others by naming the licence and linking to the licence text. Where a work has been adapted, you should indicate that the work has been changed and describe those changes. Please seek permissions from the copyright holder for uses of this work that are not included in this licence or permitted under UK Copyright Law.

Contents

Abstract **2**

1 Introduction **18**

1.1 Clouds and climate change 18

1.1.1 Role of clouds in the Earth's radiative balance 18

1.2 Aerosols 21

1.2.1 Aerosol optical depth 22

1.2.2 Direct effect 22

1.3 Aerosol cloud interactions 23

1.4 Total radiative forcing 26

1.5 Deep convection 28

1.5.1 Tropical deep convection 28

1.5.2 Convective invigoration 29

1.5.3 Anvil cirrus 33

1.5.4 Temporal evolution of deep convection and anvil cirrus 36

1.6 Summary . . . 39

1.7 Thesis Structure . . . 40

2 Data **42**

2.1 ISCCP-H . . . 42

2.2 CERES . . . 45

2.3 DARDAR . . . 46

2.4 MODIS . . . 47

3 Time Since Convection **49**

3.1 Introduction . . . 50

3.2 Method . . . 53

3.2.1 Data . . . 53

3.2.2 Deep convective core identification . . . 53

3.2.3 Time Since Convection . . . 55

3.2.4 Detrained v in situ cirrus . . . 57

3.2.5 Evaluation of TSC . . . 58

3.2.6 Comparison with HYSPLIT trajectories . . . 59

3.2.7 Cloud Properties . . . 62

3.3 Results . . . 64

3.3.1 Regional distribution of Time Since Convection. . . . 64

3.3.2 Evolution of ISCCP cloud properties 65
3.3.3 Evolution of cloud properties 68
3.3.4 Vertical profile evolution 70
3.3.5 TSC as a function of latitude 73
3.3.6 Cloud radiative effects 76
3.4 Discussion 78
3.5 Conclusion 80

4 Lifetime extension of detrained cirrus **83**

4.1 Introduction 84
4.2 Methods 88
4.2.1 Cirrus Type Flag: Land/Ocean origin 88
4.2.2 High Cloud Radiative Effect 89
4.3 Results 91
4.3.1 TSC distribution 91
4.3.2 Cloud radiative effect - detrained versus in situ 98
4.3.3 Cloud Radiative Effect - Land versus Ocean 100
4.3.4 Lifetime adjustments 102
4.4 Discussion 105
4.5 Conclusion 110

5 Sensitivity of the detrained cirrus CRE to AOD at convection 114

5.1 Introduction . . . 115

5.2 Methods . . . 117

5.2.1 Convective strength flag . . . 122

5.2.2 Sensitivity of detrained cirrus CRE to initial convective CTP . . . 123

5.2.3 Sensitivity of CTP to AOD . . . 123

5.3 Results . . . 124

5.3.1 Convective strength contrasts . . . 124

5.3.2 Diurnal cycle of land and oceanic convection . . . 126

5.3.3 Relationship between convective strength and detrained cirrus CRE . . . 130

5.3.4 Sensitivity of CRE to initial CTP . . . 137

5.3.5 Trends in the CRE-CTP sensitivity . . . 140

5.3.6 Sensitivity of CTP to AOD . . . 147

5.3.7 Constraining changes in the detrained cirrus CRE with aerosol . 150

5.4 Discussion . . . 152

5.5 Conclusion . . . 154

6 Conclusion 157

6.1 Conclusion . . . 159

6.2 Summary . . . 165

6.3 Future Work 166

6.3.1 Representation of deep convection in climate models 166

6.3.2 The impact of convective strength on other observed cloud properties 167

6.3.3 Quantifying non-local impacts of local changes 168

A Chapter 4 Supplementary **170**

Bibliography **170**

List of Figures

1.1 ISCCP Cloud Classifications from cloud optical depth and cloud top pressure joint histograms (Rossow and Schiffer, 1999) 19

1.2 Annual mean TOA (a) shortwave (SW), (b) longwave (LW) and (c) Net cloud radiative effect relative to clear-sky conditions calculated from CERES satellite data for the period 2001–2011. Adapted from (Boucher et al., 2013) 21

1.3 Schematic showing aerosol cloud effects and adjustments for liquid clouds and ice clouds, taken from Christensen et al. (2014). 25

1.4 Radiative forcing of individual bottom-up components from Bellouin et al. (2020), compared to the top-down estimates from Stevens (2015). . 26

1.5 Convective cloud growth and decay in both pristine (top) and polluted (bottom) environments, showing the effect of aerosol CCN invigoration (Rosenfeld et al., 2008). Reprinted with permission from AAAS. 29

1.6 TOA cloud radiative forcing in the CTH-COD space (Koren et al., 2010b) 35

2.1 The constellation of geostationary satellites used at the equator for ISCCP B1, from Knapp et al. (2011). © American Meteorological Society. Used with permission. 44

3.1 Relative frequency of occurrence (RFO) of the convective core regime from between 2007-2010. Red bands show the boundaries of the tropics (30S-30N). 55

3.2 Schematic diagram of the advection process in one dimension, assuming all locations start with no TSC value. Red values indicate where either a divergence or convergence of pixels occurs. The purple boxes show new convection occuring, and the arrows highlight the advection of convective air into new gridboxes between timesteps. The values of the TSC are shown in each box. 56

3.3 a) Tropical mean Time Since Convection (TSC) for 2007 and 2008, with 10th-90th percentiles highlighted. The top right histogram shows the normalised distribution of TSC values over the 2 year period, excluding the spin up time. There is little variation in the mean TSC between the years after the initial spin up period in 2007. b) Histogram of TSC values between 2007-2010 between 0 and 500 hours. Red indicates the fraction of gridboxes that contain detrained cirrus, blue are candidates for in situ cirrus formation. Right axis shows the cumulative distribution in percentage of all TSC values. >99% of TSC values are less than 500 hours. 60

3.4 Median TSC values (y-axis) along HYSPLIT trajectories (x-axis), for all trajectories and for trajectories that are stopped once they reach new convection. Error range between maximum to minimum trajectory values. Straight line indicates an exact relationship between trajectory age and TSC value. 61

3.5 a) Snapshot of the TSC 30S-30N at 00:30UTC 26th July 2008. b) Mean TSC for between 2008-2010. c) RFO of deep convection between 2008-2010. 64

3.6 ISCCP-H joint histograms showing the distribution of the CTP, and τ_c and cloud fraction as a function of days since convection. The rightmost column shows the absolute percentage change between days. Day 0 is the first 0-24 hours since convection, day 1 is 24-48 hours since convection, and so on. High CF values for upper right gridboxes would indicate a distribution skewed towards optically thick, high altitude clouds, and the opposite (optically thin, low altitude), for bottom left. Note that the top left bin also contains unreliable data, so gives an unrealistically large cloud fraction. 66

3.7 ISCCP cloud properties as a function of TSC. The normalised distribution represents the probability of finding clouds with a particular CTP or τ_c for a given TSC value. The black line indicates the mean value. Left-hand column shows the CTP and τ_c for all clouds, and right-hand column for high clouds only. 68

3.8 Vertical evolution of DARDAR cloud properties as a function of TSC. a) Cloud fraction up to 120 hours from convection. b) Cloud fraction up to 500 hours from convection. c) N_i for particles larger than 5μm. d) N_i^5 anomaly for 120 hours from convection. e) N_i for particles larger than 100μm. f) N_i^{100} anomaly from mean value for 120 hours from convection. Anomaly here refers to the difference in the N_i at a given TSC to the mean N_i at that altitude for the tropics. 71

3.9 Zonally averaged DARDAR vertical cloud amount for a given TSC bin. TSC bins are given in the top right corner. 74

3.10 Cloud Radiative Effect (CRE) as a function of TSC. a) All cloud and high cloud LW, SW and Net CRE up to 500 hours from convection. b) High cloud LW, SW and Net CRE up to 120 hours from convection with normalised joint histogram showing the probability of finding a particular CRE value (LW in red, SW in blue) for a given TSC value. 75

4.1 Sample TSC snapshot from April 9th 2008, 00:30UTC. (a) Time since convection (TSC) (b) In situ versus detrained cirrus flag values (c) land versus ocean convective origin flag. (d-f) 2008 annual mean for (a-c). 89

4.2 Snapshot of (a) All sky SW CRE for 12:00UTC 02/03/2008, (b) Monthly mean background SW CRE (March), (c) High cloud SW CRE for 12:00UTC 02/03/2008. 92

4.3 Distribution of detrained and in situ cirrus flags as a function of TSC. (a) The count of each flag as a fraction of the total TSC distribution. (b) The total distribution of each flag. 94

4.4 Diurnal cycle of tropical deep convection, normalised such that the maxima of each cycle is one, for (a) the entire globe, (b) land origin convection (c) ocean origin convection. The error bars correspond to the standard deviation of the interannual variability between 1984 and 2016. . . 95

4.5 Total distribution of the lifetimes of ocean-origin and land-origin. 96

4.6 Lifetime of detrained cirrus as a function of the timing of the initial convection for all, land, and ocean origin cirrus. The error bars represent the interannual variability over the study period. 97

4.7 The cloud radiative effects (Net, LW, SW) as a function of the TSC for both detrained, in situ air parcels, and the weighted sum of both. The vertical line shows the modal lifetime of the detrained cirrus. Note that in situ values at TSC less than 6 hours are unreliable due to the small number of data points. 99

4.8 Total LW, SW and Net CRE as a function of TSC. Dotted lines show the land-origin CRE and solid lines show the ocean-origin CRE. The vertical lines show the modal lifetimes of the ocean and land detrained cirrus. . 100

4.9 The fractional distribution of the detrained versus in situ air parcels. Dotted lines represent various distributions when the detrained cirrus are extended by a percentage. 103

4.10 Change in CRE for all, land and ocean origin air parcels for a given percentage increase in the lifetime of the detrained cirrus clouds. 104

4.11 Total net (left axis) and LW and SW (right axis) CRE as a function of TSC.The dashed and dotted lines represent a 50% and 100% increase in the lifetime of detrained cirrus respectively. Note the separate axis for Net, LW and SW radiatve effects, introduced here to show the changes in CRE for each lifetime extension more clearly. 106

5.1 Schematic showing how the AOD-CTP sensitivity, which exists in convective space c, can be linked to the CRE-CTP in detrained space d. . . . 118

5.2 Schematic showing a) convection occurring at some location, and b) the associated probability of finding convection, given that some convection occurred at a). 119

5.3 Heatmap of the probability of finding detrained cirrus which originated from 10x10°gridboxes between (a) (0N-10N, 60E-70E), (b) (20S-10S, 120E-130E), (c) (20S-10S, 10E-20E). These maps are for the year 2002. 120

5.4 Probability density of the cloud top pressure of convection between 1984-2017. The coloured bins represent the convective strength bins used in the TSC dataset. 125

5.5 (a,b,d,e) shows the regional probability density of detrained cirrus originating from each convective strength bin. (c,f,g,h,i) shows the difference between the probability density for specific convective strength bins. The probability density is normalised such that each map adds up to one, allowing for a direct comparison between bins that contain different amounts of detrained cirrus. 126

5.6 The diurnal cycle of convection, binned by convective strength, for a) all convection, b) land convection, and c) ocean convection. The diurnal cycles are normalised such that they all sum to 1, to allow for direct comparison between different weighted bins. 127

5.7 The modal local solar time of convection for a) all convection. b) the weakest convective strength bin. c) the strongest convective strength bin. 130

5.8 Net, LW, SW CRE as a function of TSC for all origin (a,b,c), land-origin (d,e,f), and ocean-origin (g,h,i) detrained cirrus in each convective strength bin. Note the TSC is only up to 30 hours, as this is where the majority of the difference in the CRE occurs. 131

5.9 LW and SW lifetime detrained cirrus CRE binned by local solar time of convective initiation. 134

5.10 Sensitivity of detrained cirrus net CRE to deep convective CTP for a) all origin, b) land-origin, and c) ocean-origin. As above for d,e,f) LW CRE and g,h,i) SW CRE. 136

5.11 Timeseries of the CRE-CTP sensitivity for all origin (black), land-origin (orange line), and ocean-origin (blue) detrained cirrus. The shaded area represents the uncertainty on the linear fit for each year (Note: excluded 2009 data is interpolated). 141

5.12 Timeseries of the net, LW, SW, CRE for each convective strength bin, for land-origin and ocean-origin detrained cirrus. Results are normalised to a baseline where the CRE in 2000=0 (Note: excluded 2009 data is interpolated). 142

5.13 Diurnal cycle for low SW CRE years (2005-2011), and all other years. a) Strongest oceanic convection bin. b) Weakest oceanic convection bin. c) Strongest land convection bin. d) Weakest land convection bin 145

5.14 Difference in the mean normalised probability density of deep convection for 2005-2011 and the outer years of the study period. The distributions are normalised such that for each period the maps sum to one to account for the fact that there is a varying amount of absolute convection between the periods. 146

5.15 a) Sensitivity of the log of the cloud top pressure CTP to the log of the aerosol optical depth AOD. b) Same as a) for high cloud. c) A given change in the log of the AOD according to Bellouin et al. (2020). d) The f_{det} term, described in the methods section, which maps the dCRE/dCTP sensitivity to the detrained space. e) The change in the CRE for a given change in the AOD. f) Same as e) but for high cloud. 148

5.16 The change in the CRE for a given aerosol change, as for Figure 5.15e) and f), but using the separate land and ocean CRE-CTP sensitivity values from Figure 5.10b) and c). Note the scale on panel (b) is half that of panel (a). 151

A.1 Histogram of the lifetimes of detrained cirrus using a 20% threshold and a 10% threshold for the lifetime cutoff point. 170

A.2 Change in the lifetime extension CRE using the two different calculated cutoffs from Figure A.1. 171

Chapter 1

Introduction

1.1 Clouds and climate change

1.1.1 Role of clouds in the Earth's radiative balance

Clouds play a fundamental role in balancing the Earth's radiative budget through the absorption and reflection of solar and terrestrial radiation. Depending on their size, location, and optical properties, clouds can cool or warm the atmosphere and, as part of large-scale circulations, transport water and energy in the form of latent heat to different latitudes and longitudes (Lohmann et al., 2016). Clouds are inevitably influenced by their environment, and these systems create complex feedbacks that regulate the planet's energy budget and can be perturbed significantly by anthropogenic aerosol emissions (Kristjánsson et al., 2005).

The response of clouds to their environment depends on their properties, most importantly their optical depth (a measure of how opaque they are to incoming solar radiation), liquid water content, and their height. It is useful to split up clouds by type to assess their individual radiative properties, record their frequency, and simplify our

understanding of how different types of clouds interact with their environment. Luke Howard first attempted this qualitatively in 1803 (Howard, 1803), with modern cloud classifications being performed by cloud climatology projects such as the International
20 Satellite Cloud Climatology Project, ISCCP (Schiffer and Rossow, 1983). Rossow and Schiffer (1999) classified clouds by cloud optical depth and cloud top pressure into the ISCCP categories shown in Fig 1.1:

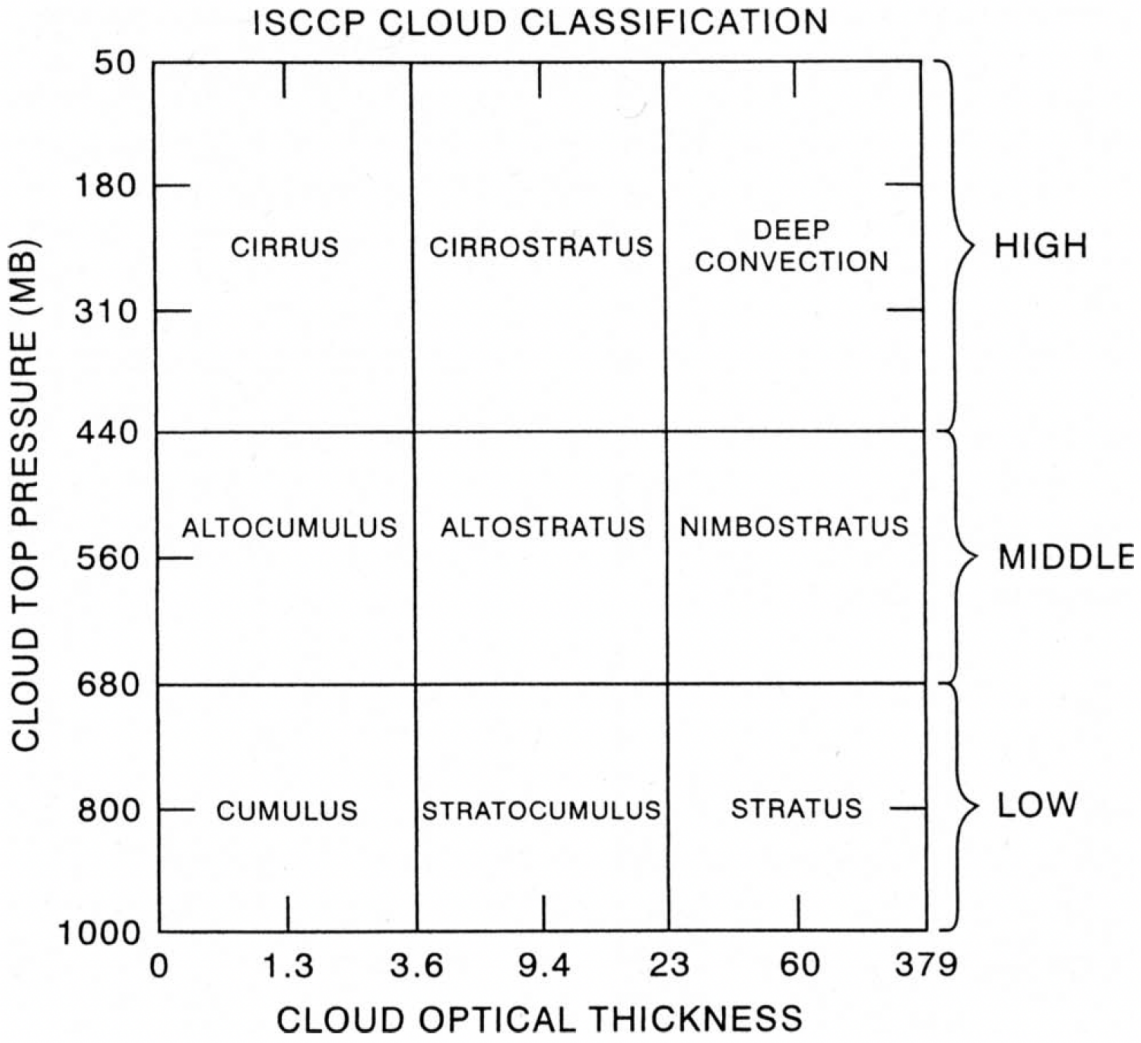


Figure 1.1: ISCCP Cloud Classifications from cloud optical depth and cloud top pressure joint histograms (Rossow and Schiffer, 1999)

Radiative effects of clouds

Clouds cool the atmosphere by reflecting incoming solar shortwave (SW) radiation back into space and warm it through the absorption and re-emission of longwave (LW) terrestrial radiation, reducing the amount of LW radiation that is allowed to escape to space relative to clear sky. The albedo of a cloud determines how much solar radiation it reflects back to space. The albedo of a cloud is governed by its optical depth (τ), which in turn is determined by its liquid water path (LWP) and droplet number concentration (N_c) (Platnick and Twomey, 1994).

Optically thick, warm-top clouds, such as stratocumulus, are highly reflective (high albedo) and cool the atmosphere because their LW warming is small. Much of the albedo cooling effect also comes from deep convective clouds in the tropics and stratus clouds in the mid-high latitudes (Hartmann et al., 1992). On the other hand, optically thinner ($\tau < 10$), high-altitude cirrus clouds may warm the atmosphere in much the same way as greenhouse gases. By trapping outgoing LW radiation from the surface of the Earth without reflecting much solar SW radiation, cirrus clouds can have a net warming effect (Choi and Ho, 2006). In the tropics, Hartmann et al. (1992) and Futyan et al. (2004) suggest these two SW and LW effects, whilst individually large, generally cancel out, leading to a net zero cloud radiative effect (CRE) in the region. Figure 1.2 shows the LW, SW and net top of atmosphere, TOA, CRE (Boucher et al., 2013). The global mean CRE is -20Wm^{-2}, composed of a SW cooling of -50Wm^{-2} and a smaller LW warming of 30Wm^{-2}. Importantly, because the SW and LW effects are large in the tropics, any small percentage change in the individual components, due to aerosol for example, can greatly impact the net CRE.

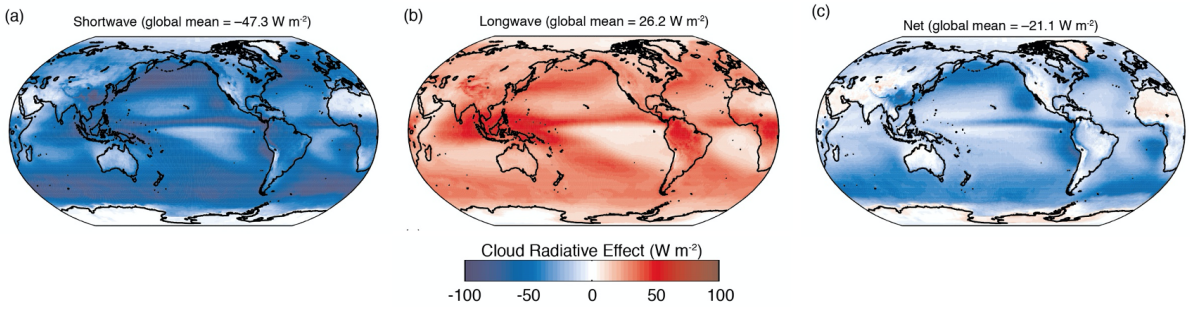


Figure 1.2: Annual mean TOA (a) shortwave (SW), (b) longwave (LW) and (c) Net cloud radiative effect relative to clear-sky conditions calculated from CERES satellite data for the period 2001–2011. Adapted from (Boucher et al., 2013)

1.2 Aerosols

Aerosols are very small (nm to μm scale) solid and liquid particles suspended in the air. Also known as particulate matter, they have a range of anthropogenic and natural sources. Anthropogenic aerosols, such as sulfur dioxide, are emitted from transportation or from industrial activity. Natural aerosols also have a variety of sources, from sea salt spray to desert dust (Andreae and Rosenfeld, 2008). Aerosols are removed through the atmosphere through wet and dry deposition. Wet deposition removes aerosols from the atmosphere with precipitation and dominates compared to dry deposition (Textor et al., 2006). Dry deposition occurs when aerosols are removed from the atmosphere through gravity. Aerosols affect the radiative budget of the atmosphere through their direct effect (absorption and scattering of incoming shortwave solar and outgoing longwave terrestrial radiation) and their indirect effect (through the altering of cloud microphysical properties and precipitation efficiencies that alter the radiative effects of clouds (Forster et al., 2021)). The concentration of aerosols in the atmosphere is highly spatio-temporally heterogeneous, owing to the different lifetimes of aerosols and their varying sources and sinks (Remer et al., 2008). As such, their direct radiative

effects are also much more regionally and temporally variable than greenhouse gases, which have a much more homogeneous radiative forcing (Grandey et al., 2018).

1.2.1 Aerosol optical depth

The aerosol optical depth (AOD) is one of the most useful remote sensing parameters for measuring the total amount of aerosol in the atmosphere due to it's large spatial coverage in satellites. The AOD measures the extinction of light within a column of aerosol in the atmosphere. An optical depth of around 0.4 or above is considered a polluted or hazy environment. As the name suggests, AOD is a vertically integrated optical property of the aerosol, so tells us a limited amount about the chemical and physical properties of the aerosol (Stier, 2016). These properties influence not only the radiative effect of the aerosol but also how they interact with clouds.

1.2.2 Direct effect

Aerosols have a direct overall cooling effect on the Earth's radiative budget through the scattering and absorption of solar radiation. The amount of scattering and absorption, and thus the amount of cooling or warming, depends on the size and distribution of the aerosols as well as molecular properties such as aerosol optical depth (τ), single scattering albedo ($\overline{\omega_0}$) and the refractive index (Hansen et al., 1997). Black carbon, for example, will absorb solar radiation more than highly reflective sulfates and, as such, warm the layer of the atmosphere they are in whilst cooling the surface. Attempts have been made to bound the total anthropogenic direct aerosol forcing, RF_{ari}, (radiative forcing from aerosol-radiation interactions) with Bellouin et al. (2020) giving a value for the RF_{ari} between -0.45 Wm^{-2} and -0.05 Wm^{-2}.

Adjustments to aerosol-radiation interaction

Aerosol perturbations to the atmosphere's radiative properties also affect cloud microphysical properties and evolution (Wang, 2013; Rosenfeld et al., 2014), as well as changes to the composition of the atmosphere. These are the adjustments to the aerosol radiation interaction (ARI) and contribute some of the largest uncertainties in climate forcing (Forster et al., 2021). Many of these adjustments come from absorbing aerosols. In contrast to aerosols that act as cloud condensation nuclei (CCN), absorbing aerosols such as black carbon (BC) significantly warm the layer of the atmosphere they reside in through absorption and cool the surface through both absorption and scattering of radiation (Wang, 2013). This leads to an overall TOA positive radiative forcing for the absorbing aerosols (Myhre et al., 1998; Penner et al., 1998; Bond et al., 2013) and influences cloud evolution and properties through atmospheric heating and surface cooling. This semi-direct effect may reduce low cloud cover through atmospheric heating and a reduction in the relative humidity (Hansen et al., 1997). These adjustments to the ARI are thought to be small and mainly offset by the direct effect (Bellouin et al., 2020). The cooling from the direct effect is less when rapid adjustments are made, with the effective radiative forcing (i.e the radiative forcing taking into account the adjustments) ERF_{ari} given between -0.71 and +0.14 Wm^{-2} (Bellouin et al., 2020).

1.3 Aerosol cloud interactions

In addition to their direct radiative forcing, aerosols also affect cloud radiative forcing through the indirect effect, whereby aerosols increase the albedo of a cloud, causing it to reflect more incoming SW radiation. Aerosols also alter cloud microphysical and thus radiative properties; these are known as adjustments.

Twomey effect

The fundamental mechanisms by which aerosols alter cloud properties is through their behaviour as cloud condensation nuclei (CCN) and ice nucleating particles (INP). Cloud droplets form on aerosols, such as dust or anthropogenic aerosols (Aitken, 1882). Acting as CCN, aerosols cause a higher number of smaller cloud droplets to form (Twomey, 1974). By increasing the cloud droplet number concentration (N_d), Twomey (1977) showed that for a fixed LWP (liquid water path), the relationship between N_d and cloud optical depth, τ is:

$$\tau \propto {N_d}^{\frac{1}{3}} \tag{1.1}$$

By increasing the cloud's optical depth (and thus its albedo), aerosols increase the amount of SW radiation it reflects, thereby having a cooling effect and negative radiative forcing.

Adjustments to aerosol-cloud interactions

Aerosols also cause adjustments to cloud lifetimes and precipitation efficiencies. Albrecht (1989) showed that the precipitation efficiency decreased for clouds with smaller cloud droplets formed in the presence of aerosols, causing the clouds to have larger LWP and longer lifetimes. This precipitation suppression has been observed in satellite studies (Fan et al., 2020), however aerosol driven changes to the LWP present large uncertainties in climate forcing calculations (Ackerman et al., 2004; Toll et al., 2019). Precipitation suppression also reduces the amount of wet scavenging (aerosol depletion through precipitation) that occurs, causing aerosol residence times to increase (Jing and Suzuki, 2018).

The adjustments to cloud lifetime and LWP contributes a small warming effect to the

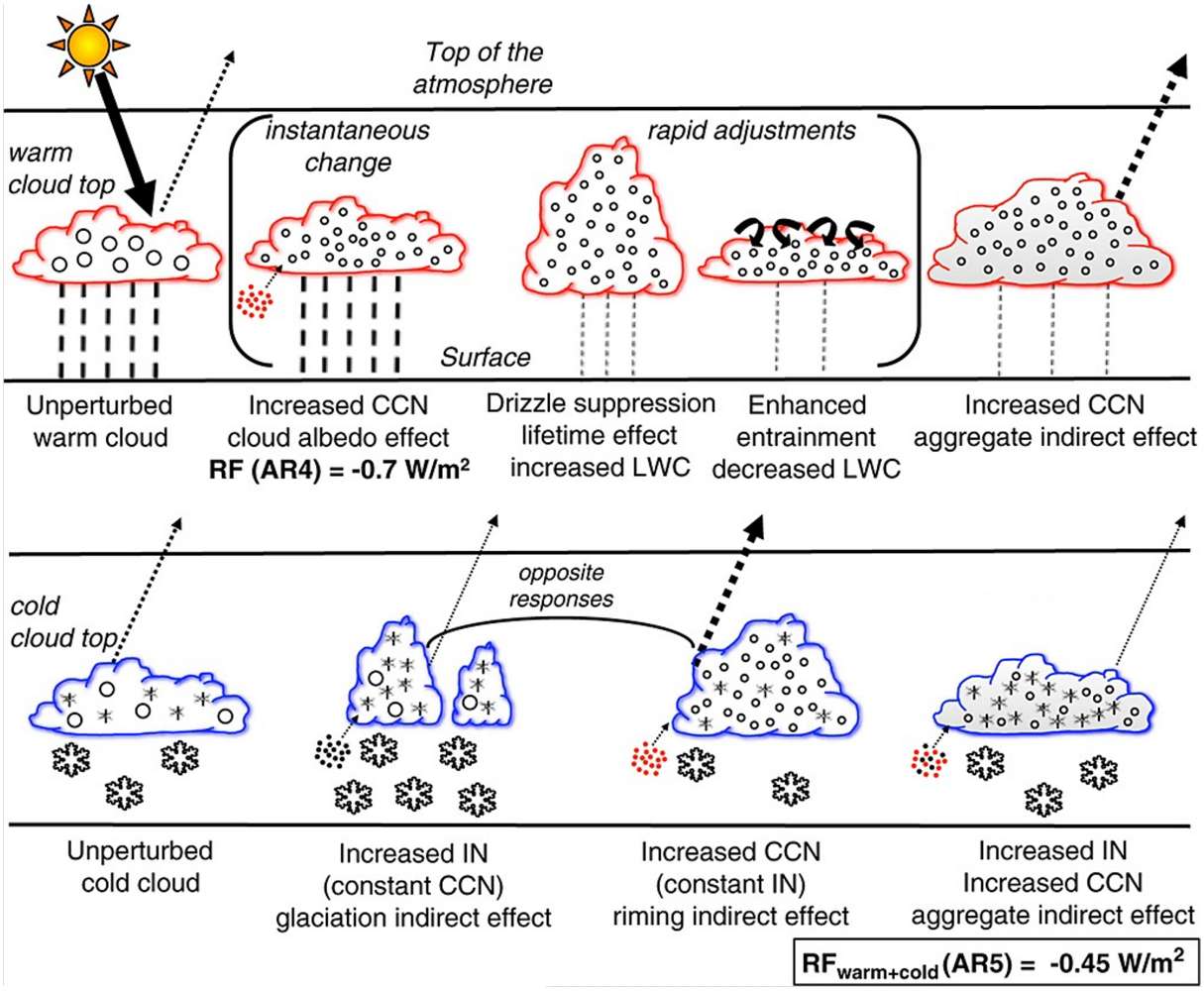


Figure 1.3: Schematic showing aerosol cloud effects and adjustments for liquid clouds and ice clouds, taken from Christensen et al. (2014).

overall effective radiative forcing (Bellouin et al., 2020). An increase in N_c via aerosol loading can also deplete LWP. Smaller droplets are more likely to evaporate quickly, which entrains dry air into the cloud and reducing the LWP of the cloud (Ackerman et al., 2004; Xue and Feingold, 2006). This may in turn reduced the cloud albedo (Stevens and Feingold, 2009). This negative LWP response has been observed at high aerosol loading (Gryspeerdt et al., 2022).

As well as longer lifetimes, Pincus and Baker (1994) predicted that aerosol loading, through precipitation suppression, caused higher cloud tops in stratocumulus clouds. As mentioned, precipitation suppression also reduced wet scavenging. Combining

these two adjustments means that increased aerosol concentrations are hypothesised to sometimes cause clouds to live longer and reflect more SW solar radiation through an increased albedo, emphasising the indirect effect and contributing further to a cooling CRE. Figure 3.2 shows a schematic of adjustments and cloud aerosol interactions for liquid and mixed-phase clouds from Christensen et al. (2014).

1.4 Total radiative forcing

Estimates of the total radiative forcing from the direct (RFari), indirect (RFaci), adjustments to the ACI (RAaci from the CF and LWP) and ARI (RAari), and the total effective radiative forcing (ERF, bottom-up estimate) from Bellouin et al. (2020) are given in Figure 1.4.

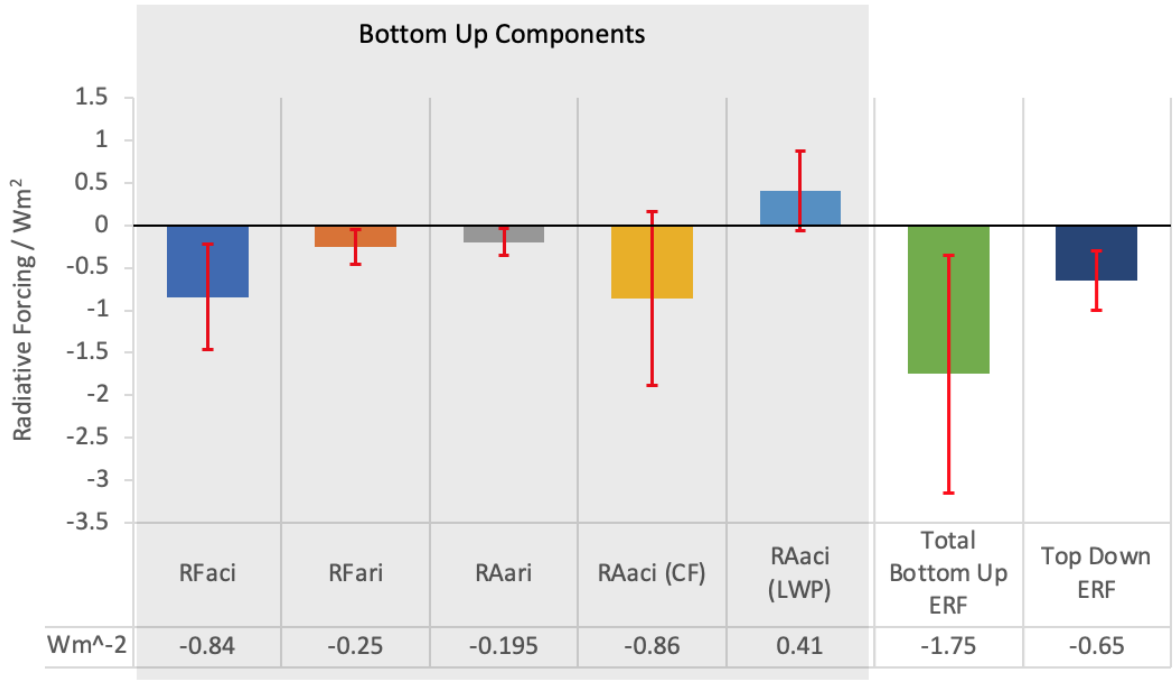


Figure 1.4: Radiative forcing of individual bottom-up components from Bellouin et al. (2020), compared to the top-down estimates from Stevens (2015).

A comparison to the top-down estimate from Stevens (2015) is also shown. Top down estimates are also given by Murphy et al. (2009) who, using TOA radiation budget measurements from satellites calculate an ERF of -0.6Wm^{-2} to -1.5Wm^{-2}. Cherian et al. (2014) uses observations of aerosol trends of Europe to constrain the ERF in global circulation models to obtain a value for the global ERF of between -0.9 Wm^{-2} to -1.5 Wm^{-2}. There is a large overall negative forcing given by Bellouin et al. (2020), with a lower and upper bound of -3.15Wm^{-2} and -0.35Wm^{-2} respectively, with negative contributions coming from the direct and indirect effect and their associated adjustments. The only positive warming contribution from Bellouin et al. (2020) is the adjustments to the aerosol-cloud interaction associated with a change in the LWP.

Bellouin et al. (2020) notes that their own estimates of the radiative forcing do not take into account the effects of aerosols on mixed-phase clouds, which include deep convective regimes, as models do not simulate them and there are no observational constraints. Constraining the aerosol effects on mixed-phase clouds is vital to better understand the present-day aerosol forcing and reduce the gap between the bottom-up and top-down estimates of radiative forcing. Reconciling these two estimates of radiative forcing requires either some 'missing warming' that is not currently accounted for in the bottom up ERF, or the cooling effect in current bottom up estimates being smaller than originally thought. One component of this challenge, and something that could be responsible for some of the missing warming, is constraining the aerosol effects on deep convective regimes, from the deep convective cores to the anvil cirrus that flow from them.

1.5 Deep convection

1.5.1 Tropical deep convection

Deep convective clouds (DCC) occur mostly in tropical and subtropical regions. They are characterized by one or more convective cores (cumulus towers), with strong updrafts that merge the cores at higher altitudes, and large anvils flowing out from the region of convective activity (Fan et al., 2013). Deep convection plays a vital role in the Earth's energy budget, as the latent heating from convection drives the large-scale circulation of the Hadley and Walker cells, transporting heat and water from the tropics to the mid to high latitudes (Heintzenberg and Charlson, 2009).

The TOA radiative forcing from deep convective clouds in the tropics can vary greatly depending on the optical depth of the cloud. Hartmann et al. (2001b) found that the TOA radiative forcing of DCC ranged between +20 to -119 Wm^2, with the optical depth of tropical DCC ranging from 1 to 60 in the upper troposphere. Characterised by high, optically thick cloud tops, they reflect incoming shortwave solar radiation. However, they also have a significant warming effect due to their high cloud tops. These two balancing factors, and the fact that DCC tends to be accompanied by more optically thin high clouds, mean the overall net radiative forcing from regions of tropical convection tends to be small. Because of this balance, understanding the controls on deep convection and the outflow of anvil cirrus is important in our estimates of future climate change. A small percentage change in the large forcing from the cirrus clouds could significantly impact this balance.

1.5.2 Convective invigoration

The schematic of Twomey indirect effect and adjustments shown in Figure 3.2, whilst useful, is a simplification of the processes that occur in response to a perturbation in the concentration of CCN, particularly in mixed-phase clouds such as DCC (Lebo and
195 Seinfeld, 2011). The complexity of the dynamics (vertical updraft, wind shear) and ice processes in mixed-phase clouds also means that isolating the effects of aerosols from the meteorological conditions that also influence convective clouds is difficult.

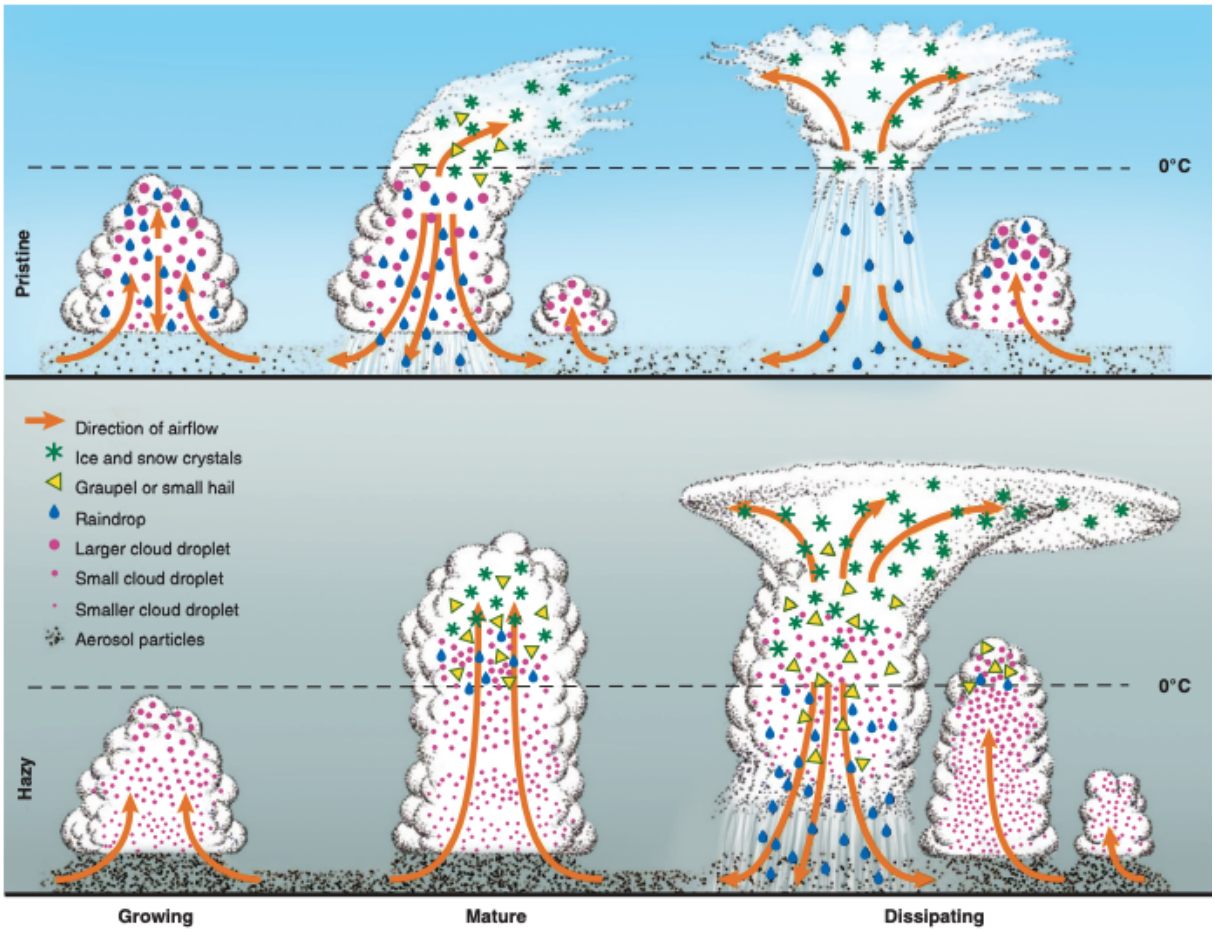


Figure 1.5: Convective cloud growth and decay in both pristine (top) and polluted (bottom) environments, showing the effect of aerosol CCN invigoration (Rosenfeld et al., 2008). Reprinted with permission from AAAS.

Studies have hypothesised that aerosol loading increases convective strength, with the-

oretical works from Williams et al. (2002), Rosenfeld et al. (2008), and Stevens and Feingold (2009) and observational works from Koren et al. (2005), Koren et al. (2010b), and Koren et al. (2010a) supporting this hypothesis.

Rosenfeld et al. (2008) made the case that aerosols can both increase and decrease precipitation in convective clouds. Decreased precipitation can occur when aerosols scatter and absorb solar radiation, reducing the amount of surface heating and, thus, the amount of evaporated water available for convective cloud production. On the other hand, Rosenfeld et al. (2008) also hypothesised the idea of 'cold phase' invigoration, which can delay precipitation and increase its intensity. As with the Twomey effect, aerosols acting as CCN cause smaller cloud droplets to form. This suppresses precipitation in convective clouds through delayed coalescence of rain droplets. This allows the smaller cloud droplets to travel higher into the convective core. These smaller droplets freeze at a higher altitude, releasing energy in the form of latent heat, which drives further convection and the transportation of moisture higher into the troposphere. Figure 1.5 shows a schematic of aerosol invigoration leading to delayed but larger precipitation. Critical examinations of this particular theory have suggested that it is not a large contributing factor to aerosol invigoration (Igel and van den Heever, 2021). Simplified parcel simulations have shown that updrafts could actually weaken with precipitation suppression (Peters et al., 2023), through increased entrainment. Nevertheless, an observational study of increased lightning along shipping lanes from Thornton et al. (2017) provides evidence of some relationship between AOD and increased intensity of tropical convection.

Many have also hypothesised a 'warm-phase' invigoration that is distinct from the 'cold-phase' invigoration described above (Fan et al., 2018; Koren et al., 2014; Cotton and Walko, 2021). The 'warm-phase' invigoration hypothesises that, in the presence of ultrafine aerosols (UAP<50nm in diameter), more cloud droplets condense above

the cloud base; this lowers the supersaturation and increases the amount of latent heat released in the cloud to drive convection. The larger amount of condensate also contributes to an increase in the warm rain rate and supercooled water, which freezes and adds more latent heat to drive convection and storm electrification. Warm phase invigoration is thought to be a more likely mechanism for invigoration than cold phase (Varble et al., 2023). However studies have also shown that aerosol loading decreases shallow cumulus lifetime due to entrainment effects (Jiang et al., 2006). It is not clear whether these processes counter invigoration in deep convection.

In contrast to the above mechanisms, simulations from Abbott and Cronin (2021) hypothesised that convective invigoration was driven not through the cold or warm phased mechanisms but, in fact, was due to an increase in environmental humidity that is caused by aerosols mixing more condensed water in with the surrounding air. There are no observational studies supporting this work, but unlike the cold and warm phase mechanisms, it takes into account the environmental factors as well as the cloud microphysics and doesn't depend on ice phase processes. However, work from Dagan et al. (2022) suggests that these mechanisms might be an artefact of the boundary conditions of the simulation.

Although there is much uncertainty around mechanisms that drive invigoration in deep convection, some attempts have been made to quantify the radiative forcing due to invigoration. Andreae et al. (2004) showed the potential for warming from invigoration in field campaigns looking at wildfires over the Amazon. Fan et al. (2012) suggested, using high resolution model simulations, that there could be large positive warming of +5.6Wm^{-2}. Blossey et al. (2018) found an insignificant change in the net CRE in simulations of a modelled shipping lane. Koren et al. (2010b) and Rosenfeld et al. (2014) both suggest, but do not show, that changes in the wind profile could impact cirrus clouds, by reducing their optical depth and increasing their detrainment

height, to induce a strong warming. These conflicting theoretical and observational results highlight the uncertainty in the response of high clouds to aerosol. More work needs to be done to quantify the radiative impacts that anvil cirrus clouds may have due to changes in properties of deep convection and to explain the mechanisms responsible for results from, e.g. Thornton et al. (2017).

Observing aerosol invigoration is not straightforward due to the difficulties in retrieving the aerosol AOD and N_c in the same pixel (Bellouin et al., 2020; Gryspeerdt et al., 2015a), separating meteorological effects from aerosol effects, and choosing suitable proxies for determining 'convective strength'. Williams et al. (2002) first observed potential invigoration by analysing lightning rates, convective available potential energy (CAPE), and aerosol in the Amazon. CAPE is defined as the integrated amount of work that an upward buoyancy force would perform on an air parcel if it rose vertically in the atmosphere. A nonzero CAPE indicates atmospheric instability, with a positive CAPE indicating an air parcel would rise and a negative CAPE indicating a fall. Studies often used proxies rather than CAPE itself for measuring convective invigoration. Jensen et al. (2018) showed that an increasing CAPE correlated with higher cloud fraction and higher cloud top height. Rosenfeld et al. (2008) explored the non-linear relationship between the CCN concentration and the CAPE. By considering a theoretical parcel model, they showed that the atmospheric heating from the direct aerosol effect competes against the aerosol invigoration to reduce the CAPE. They showed in their illustration a maximum CAPE occurring at $CCN_{0.04}$ of 1200cm^{-2} or an AOD of 0.25. This matches well with observations from Koren et al. (2008), who saw a peak in the cloud fraction (which correlates with higher cloud tops) at around 0.25 AOD using MODIS data in the Amazon dry season. Koren et al. (2005) suggested clear observation evidence of cold phase invigoration, however methodological flaws were subsequently found in this research (Varble et al., 2023).

As mentioned above, observing aerosol invigoration is difficult due to collocating CCN measurements, or N_c, at cloud base and updraft velocity in the same region or over a large enough range of conditions. In these instances proxies are used for CCN, such as surface based measurements of CCN, or for larger regional studies AOD. AOD is an imperfect proxy as it doesn't correlate well with low level CCN (Stier, 2016; Veals et al., 2022). AOD also increases with relative humidity (RH) (Quaas et al., 2010), which is naturally higher nearer to clouds. Wet scavenging of aerosols (Gryspeerdt et al., 2015b) also occurs in regions of convective activity, thus altering the retrieved AOD value around the location of deep convection, highlighting the importance of obtaining AOD in the right locations relative to the convection. Vertical wind retrievals inside deep convective cores are also very rare, with most coming from in situ measurements that are difficult to put into a wider context outside of the specific experiment, meaning it is hard to scale up to a global estimate of the impact. It is also difficult to control for meteorological variability in observational invigoration studies and for factors that may impact invigoration proxies such as cloud top height. For a full critical evaluation of aerosol invigoration, see Varble et al. (2023). There is clear observational evidence that aerosols impact convective clouds (Thornton et al., 2017); however, there is also clearly much difficulty in isolating the aerosol response (Varble et al., 2023). Christensen et al. (2014) attempted to bound a global estimate for the indirect cloud aerosol effect for convective clouds, giving a value of 0.15 ± 0.23 Wm^{-2}, however this estimate didn't take into account the non-local radiative effect of anvil cirrus that spread out far from the initial convection.

1.5.3 Anvil cirrus

As well as measuring convective invigoration through the quantification of convective strength, the properties of the anvil cirrus clouds that flow out of the convective cores

are of significant importance due to their much larger size and longer lifetimes than the convective cores. Of particular interest is how the strength of convection affects the properties of the anvil cirrus throughout its evolution. By looking at MODIS retrieved cloud properties over the Atlantic during June-August 2002, Koren et al. (2005) showed a strong positive correlation between AOD in clean (AOD < 0.2) and hazy (AOD > 0.2) conditions and the cloud fraction, cloud optical depth, and cloud top pressure of the anvil cirrus (Koren et al., 2005). Koren et al. (2010b) also showed a positive correlation between the anvil cirrus cloud fraction and the AOD in the Atlantic and Pacific regions.

This increase in anvil cirrus area correlates with a decrease in the ice optical depth in the anvil due to spreading the anvil over a larger area. The following proposed mechanism causes these larger anvils: increased aerosol loading leads to more convective invigoration. This causes deeper convective cores that reach higher into the atmosphere due to the small cloud droplets (Lin et al., 2006; Li et al., 2011). The anvil cirrus formation then occurs at higher altitudes with greater wind shear, and thus a larger spreading of the anvil and lower optical depth (Lindsey and Fromm, 2008; Koren et al., 2010b).

The radiative effects of the out-flowing cirrus from deep convection are particularly important in this work since, due to their spatial extent, they exert a large radiative effect, much larger than the convective cores themselves. The sign of the radiative forcing from cirrus in the tropics is highly dependent on the optical depth of the cloud, with Choi and Ho (2006) finding that thin cirrus with an optical depth $\tau < 10$ have a warming effect, whilst cirrus with $\tau > 10$ have a cooling effect. Since more than 60% of tropical ice clouds are thin cirrus, the cloud radiative forcing from these clouds significantly affects the energy budget of the tropics. Koren et al. (2010b) showed that the cloud top height also plays a vital role in the sign of the forcing from cirrus by visualising the net top of atmosphere (TOA) cloud radiative effect in cloud top height

and cloud optical depth (CTH-COD) space, as shown in Figure 1.6.

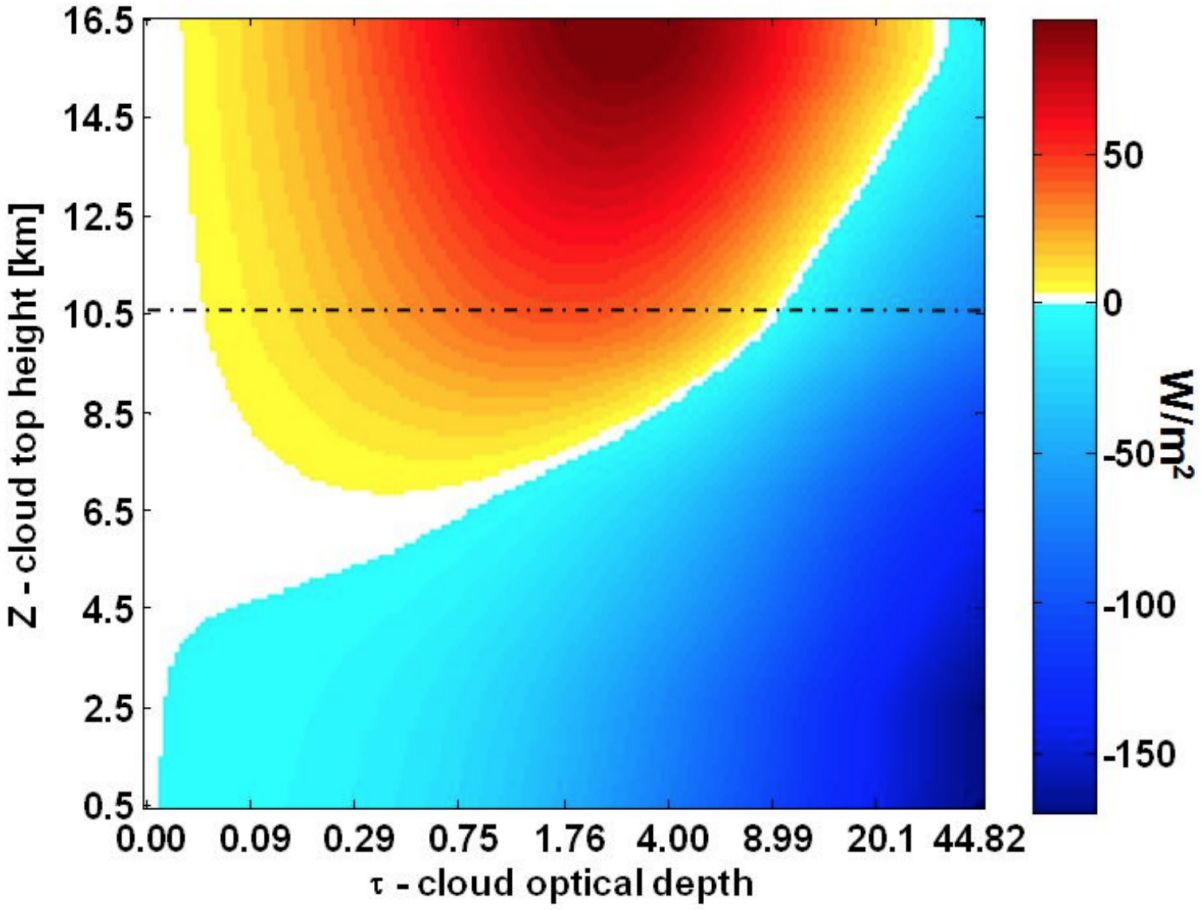


Figure 1.6: TOA cloud radiative forcing in the CTH-COD space (Koren et al., 2010b)

This shows that if the cirrus cloud top height is increased and optical depth is de-
330 creased due to aerosol invigoration, there is potential for much greater warming. This agrees with the observations from Choi and Ho (2006), who found that for cirrus clouds that exist at a height between 10-12km, the optical depth at which the boundary between cooling and warming exists is around $\tau = 10$.

1.5.4 Temporal evolution of deep convection and anvil cirrus

As previously mentioned, Christensen et al. (2014) estimated the indirect effect of convective cloud-aerosol interactions. This estimate, however, only considered the impact that aerosols had on the convection itself. As highlighted by Rosenfeld et al. (2014), in order to assess the full impact that aerosols have on deep convection, it is also important to include the full evolution of the anvil cirrus. The evolution of anvil cirrus across their entire lifetime has been studied in previous work by using Lagrangian frameworks to track deep convection and the subsequent anvil cirrus.

Gehlot and Quaas (2012) applied a Lagrangian framework to ISCCP data in order to evaluate the performance of the ECHAM5 general circulation model. They followed a similar approach to that of Luo and Rossow (2004), where upper tropospheric air masses were traced using reanalysis wind data in order to follow the evolution of cirrus developing from deep convection. Luo and Rossow (2004) looked at the evolution of cirrus and cirrostratus up to 5 days from a convective event. They found a rapid decay (6-12hrs) of deep convection from the peak and an associated growth of cirrus. After one day they found a decay of the cirrostratus, likely associated with a loss of cloud water due to larger particles with a large sedimentation mass flux. The cirrus decay was much slower, occurring over 5 days, from a maximum cirrus cloud fraction of 0.4 to 0.15 after 5 days.

Two distinct cirrus types will be referenced throughout this thesis. The first type, known as in-situ cirrus clouds, form directly from the gas phase at temperatures below approximately 235K (Krämer et al., 2016). On the other hand, liquid-origin cirrus clouds form through heterogeneous nucleation in strong-updrafts, where water droplets freeze on ice nucleating particles.

Luo and Rossow (2004) also distinguished between cirrus that are entirely formed in-situ (hereafter, "in-situ cirrus") and those detrained out from convective cores (containing both liquid-origin and in-situ-formed ice crystals). They found that the detrained cirrus had, on average, longer lifetimes than the in-situ cirrus, at around 30 hours compared to 19 hours for in-situ. This suggests some mechanism for sustaining water vapour at the detrained cirrus height, allowing for longer lifetimes. Salathé and Hartmann (1997) investigated the Lagrangian evolution of the upper tropospheric humidity (UTH) in the tropics from deep convective events. They showed the UTH is sustained for up to 5 days from convection, consistent with the cirrus decay found by Luo and Rossow (2004). Garrett et al. (2005) looked at the detailed evolution of a single thunderstorm anvil cirrus cloud in Florida. They found that the advected outflow was separated into two cloud layers: a cirrus anvil at -45°C laying below a thin tropopause cirrus (TTC) at -70°C. The TTC cirrus lifetime was sustained longer than that of the anvil cirrus, potentially due to the anvil cirrus shielding the TTC cirrus from terrestrial radiation, as proposed by Hartmann et al. (2001a).

The lifetime CRE of deep convection and detrained anvil cirrus is particularly sensitive to the time at which the initial convection occurs. Jones et al. (2024) showed using SEVIRI data over continental Africa that the lifetime anvil CRE from nighttime convection had a warming effect, whereas those originating from daytime convection had a cooling effect. Gasparini et al. (2022) showed in high-resolution models that the sign of the lifetime integrated CRE of anvil clouds is also highly dependent on the time the simulation began.

The timing of convection varies significantly between land and ocean (Yang and Slingo, 2001). Therefore, the CRE of land-origin versus ocean-origin anvil cirrus may be expected to vary based on the timing of the initial convection. Any change to the distribution of land or ocean-origin convection in a future climate, or a change in the diurnal

cycle of convection, could therefore induce a large change in the average lifetime CRE of detrained cirrus.

The lifetime of detrained cirrus clouds also depends on the timing of the convection. The rate at which anvil cloud thinning occurs from convective detrainment depends on the local time at which the convective core first develops. Sokol and Hartmann (2020) found that anvil thinning occurs faster at night from convection that occurs in the afternoon. They also found that anvils thin to a 'modal' anvil optical depth between 1-2 and then do not thin as rapidly after this. This would mean that after an initial decay in optical depth, anvil cirrus exist in the COT-CTP space associated with a positive radiative forcing. A temporal investigation into the evolution of the cirrus clouds is important to understand the complete picture of deep convective events, rather than instantaneous snapshots of deep convecton or anvil cirrus.

A Lagrangian approach to tracking atmospheric phenomena, from mesoscale convective systems (Feng et al., 2012; Gehlot and Quaas, 2012; Luo and Rossow, 2004; Pincus et al., 1997) to pollutants and aerosols (Redington and Derwent, 2002), is not new. However research so far has been limited to local, mesoscale systems. A Lagrangian framework for looking at the global evolution of deep convective cloud, the subsequent outflows, microphysical and radiative properties, and the effects of aerosols on all of the above has not yet been achieved. However, the properties that the mesoscale studies have investigated and the results they found provide a solid bedrock for this research to build off and a chance to validate methods against their results.

1.6 Summary

The overarching goal of this thesis is to better understand the evolution of deep convection, from the optically thick cores and anvils to the thin detrained cirrus that flow from them, and how aerosol invigoration may impact this evolution. Deep convective clouds play a vital role in modulating the energy budget and circulation of the atmosphere; they are also responsible for extreme weather events such as lightning storms, hail and flooding. The entire deep convective system has a large SW and LW CRE, however these cancel out over its lifetime to exert a near neutral net CRE. Therefore, any changes to the properties of deep convection and the cirrus outflows, or feedbacks associated with these changes, could have profound impacts on the atmosphere and society as a whole. Furthermore, global circulation models struggle to model deep convection, with poor representation of the diurnal cycle of the deep convection. Improving our understanding of the distribution and timing of deep convection can help improve model representation and also highlight the impact that any changes in these initial conditions have on the subsequent evolution of the detrained cirrus. This thesis aims to improve our understanding of the radiative evolution of deep convection, to better understand the controls on this radiative evolution, and the impact that aerosols may have on the evolution. The aims of this thesis can be split up into three chapters.

The first aim is to broadly improve understanding of the lifecycle of deep convection and detrained cirrus over the entire tropics, in particular the radiative evolution of clouds that flow from them. Previous studies have performed Lagrangian analysis on specific deep convective systems, however many of these studies focused regionally, for short study periods, for a finite number of steps along the trajectories from deep convection, and relied on polar orbiting satellites that only provided coarse snapshots of the radiative evolution of the cirrus. A large scale composite approach to looking at the evolution of deep convection is vital if we are to capture the entire lifecycle of all

tropical deep convection, all the way to the thinnest cirrus.

The second aim of this thesis is to understand the impact that the lifetime of the detrained cirrus has on the overall CRE of high clouds in the tropics. It is suggested that some changes in the lifetime of detrained cirrus may occur due to mechanisms such as aerosol invigoration, as mentioned above. Understanding the sensitivity of the tropical CRE to changes in the lifetime of detrained cirrus is vital to assess what impact the proposed mechanisms could have.

The final aim of this thesis is to improve our understanding of how the initial strength of convection impacts the detrained cirrus CRE. There is a large amount of literature regarding mechanisms that control aerosol invigoration, however little work has been done to understand the radiative impact that such invigoration has on the lifecycle of deep convection and the non-local impacts on detrained cirrus. This work will help to bound an estimate of the impact of any potential aerosol invigoration on the tropical CRE, without evaluating the mechanisms through which invigoration may occur.

1.7 Thesis Structure

Chapter 2 gives an overview of the different types of data used throughout the thesis.

Chapter 3 describes the method used to create and verify the Time Since Convection dataset, and presents an initial investigation into the evolution of cloud properties, vertical structure and radiative evolution of deep convection and associated cirrus as a function of Time Since Convection.

Chapter 4 investigates how the lifetime of the detrained cirrus clouds impacts the over-

all high cloud radiative effect in the tropics. This analysis is also separated into land-origin versus ocean-origin convection and highlights the impact that the initial conditions and timing of the convection have on the cloud radiative effect in the tropics.

Chapter 5 uses a convective strength flag to split up the cloud radiative effect of detrained cirrus depending on the strength of the deep convection they originated from. This sensitivity is then linked to the sensitivity of cloud top pressure to AOD in an attempt to quantify the sensitivity of detrained cirrus on the AOD at the locations of the initial deep convection.

Chapter 6 presents the conclusions of this thesis, summing up its main achievements, and highlights some avenues for future research that build off this work.

Chapter 2

Data

There are a number of key satellite measurement products that are used throughout this thesis. This chapter will provide a brief overview of each of the main ones used, ISCCP-H, DARDAR, CERES, and MODIS.

2.1 ISCCP-H

The International Satellite and Cloud Climatology Project (ISCCP) was established in 1982. Its goal was to provide a continuous, reduced-resolution, global dataset to give information on surface and atmospheric properties from satellite measurements that can be used to derive cloud properties (Schiffer and Rossow, 1983). Today, it provides 34 years of continuous satellite measurements of atmospheric, cloud, and surface properties obtained by stitching together measurements from a range of geostationary weather and polar orbiting satellites. The most recent version of this product is the ISCCP-H dataset (Rossow et al., 2017), which has been updated and verified against

newer cloud datasets that have improved cloud detection capabilities due to active sensors, but shorter records (e.g. CALIPSO and CloudSat).

The primary instruments used to provide data for ISCCP are imaging radiometers on meteorological geostationary satellites. These are inputted into ISCCP in seven separate geographical streams that cover the globe (Rossow et al., 2017). Where no geostationary data are available, then polar orbiting satellites are used to fill in the gaps. If more than one geostationary satellite provides data for a gridbox, then the satellite with the largest cosine of the satellite zenith angle is used, to ensure that the satellite most directly overhead the gridbox of any particular location is used. To ensure consistency between the geostationary satellites used, the data are normalised to low-earth-orbit Advanced Very High Resolution Radiometer family (AVHRR) radiances, which are retrieved from the afternoon polar orbiting satellites. The geostationary satellites provide 3-hourly, 10km resolution to ISCCP, although in the ISCCP-HGG product used in this thesis, this resolution is scaled to 1x1 degree.

There have been considerable changes to the suite of satellites used over the long period that ISCCP-H data is available for. This changing constellation creates challenges for ensuring consistency over the study period. Figure 2.1 shows the quilt of satellites used to generate the ISCCP data from 1983 to 2011, taken from Knapp et al. (2011). From 1983-2000, there was considerable variability in the constellation of geostationary satellites used to create the ISCCP data product, most notably the lack of satellite retrievals around 60E, over the Indian Ocean. There is also significant variability in the average satellite solar zenith angle at this time. After 1998 and the launch of METEOSAT-7 and repositioning of METEOSAT-5, there was full geostationary coverage of the globe in the ISCCP dataset for the first time. After this point, the average solar satellite zenith angle becomes more constant with time. Previous studies have shown difficulties using the older ISCCP-D dataset to infer trends (Evan et al., 2007)

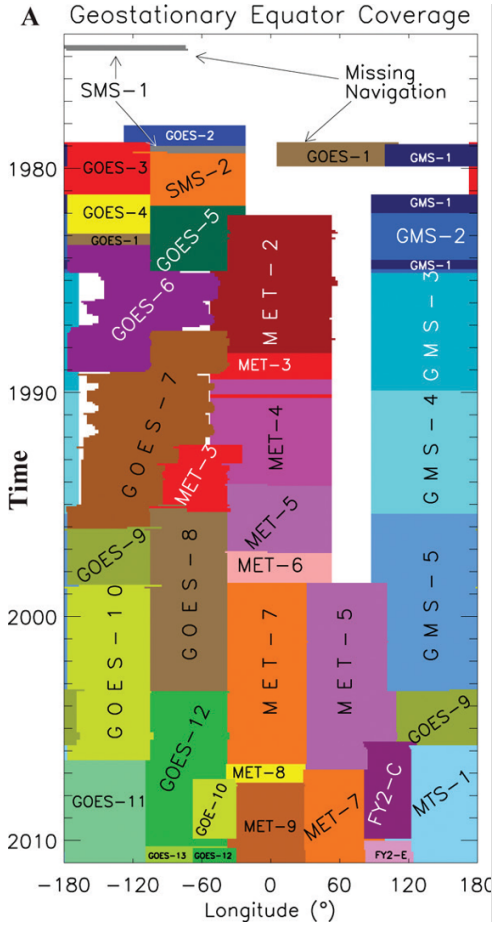


Figure 2.1: The constellation of geostationary satellites used at the equator for ISCCP B1, from Knapp et al. (2011). © American Meteorological Society. Used with permission.

because of the artefacts introduced in regions with little satellite coverage or at high satellite zenith angles. These artefacts remain in the more recent ISCCP-H dataset (Knapp et al., 2021). Most of these artefacts disappear from the data when looking only at years after 1998. Norris and Evan (2015) showed that it is possible to remove these artifacts, if there is a desire to infer longer term trends from the ISCCP dataset. In this thesis, any trend analysis is limited to years after 2000, this is also due to the limited study period of other satellite data used in the analysis.

In this thesis, cloud fraction, cloud optical thickness, cloud top pressure, and the cloud optical thickness-cloud top pressure histograms are the only products used from the ISCCP dataset. The cloud fraction, called cloud amount in the ISCCP dataset, is defined

as the percentage of pixels in a 1x1 degree gridbox that are flagged as cloudy. A pixel is considered cloudy when the radiance deviates from the clear sky radiance by a certain threshold, dependent on the surface type, in both the visible and infrared channels (Rossow and Garder, 1993). The cloud top pressure is calculated, assuming that a pixel is cloudy, from a cloud top temperature. The cloud top temperature is calculated from the deviation of the IR radiance to the radiance predicted by a radiative transfer model (Rossow and Schiffer, 1999). The cloud optical thickness is calculated from the visible radiance in the day and interpolated for the night based on adjacent daytime values. In all cases, the ISCCP data is adjusted for the diurnal cycle, taking into account cases where clouds are more detectable in the day than they are at night. The ISCCP cloud top pressure-optical depth (pc-tau) histograms are binned as shown in the introduction in Figure 1.1. As seen, there are limitations to ISCCP when trying to infer long term trends. However, the length and scale of the dataset mean that it is a very valuable tool for investigating tropical deep convection.

2.2 CERES

The Clouds and the Earth's Radiant Energy System (CERES) project has provided earth radiation budget data for the past 24 years. The CERES instruments fly on a variety of geostationary and polar orbiting satellites. In this thesis, the CERES SYN-1deg-1Hour_Terra-Aqua-MODIS-Edition4A product is used to retrieve the TOA all-sky and clear sky LW, SW fluxes as well as the albedo (NASA/LARC/SD/ASDC, 2017). This product incorporates geostationary fluxes as well as the CERES retrievals from Terra and Aqua.

The TOA fluxes are calculated using the observed radiances combined with an angular distribution model (Loeb et al., 2005). This model converts observed radiances

into fluxes by taking into account angular dependence of the radiance field, itself a function of the properties of the scene it is viewing, for example: surface type, cloud fraction, and aerosol optical depth. The instantaneous retrieved fluxes are then spatially averaged to a uniform 1x1 degree grid, and temporally averaged to 1 hourly retrievals. Since the CERES instrument does not measure directly the LW radiance, it is calculated from the total minus the SW radiance. In order to calculate the clear sky fluxes, the gridbox averaged all-sky is used, ignoring any CERES footprint that contain more than 1% cloud, as identified by the CERES-MODIS clear sky mask for MODIS pixels contained within the CERES footprint. There are regions in the tropics where no clear sky footprint is obtained, and where therefore no clear sky fluxes can be given (NASA/LARC/SD/ASDC, 2017). The TOA incoming solar radiation is calculated from data from the SORCE TIM instrument, which measures the absolute intensity of solar radiation. The CERES albedo is derived from the ratio of upward and downward shortwave flux.

2.3 DARDAR

The liDAR-raDAR, DARDAR-Nice (ice crystal number concentration, N_i) product offers vertical retrievals of N_i profiles obtained from combined lidar and radar measurements. The product is provided at 60m vertical resolution, 1.7km horizontal resolution with equatorial overpasses occurring at around 01:30am and 13:30pm local solar time. The methodology is based on the VarCloud algorithm from Delanoë and Hogan (2008) which combines CloudSat, CALIPSO and MODIS retrievals of properties of ice clouds. In the operational DARDAR product the CloudSat and CALIPSO measurements are regridded to collocate with each other, resulting in lidar, radar, and MODIS data all interpolated to the same grid. The cloud mask values in the DARDAR product are retrieved directly from the VarCloud algorithm. Both CALIPSO and CloudSat provide

mask-like products to aid in the creation of the cloud-mask. A radar cloud mask from 2B-GEOPROF (Mace, 2004) contains a value between 0-40 indicating the location of hydrometeors. A lidar mask from CALIPSO indicates five categories (clear sky, cloud, aerosol, surface and no signal) (Vaughan et al., 2023). A mask value greater than 30 from the radar mask, or the lidar cloud flag, indicates a cloud in the DARDAR dataset.

The N_i is derived in Sourdeval et al. (2018) and expands on the Delanoë and Hogan (2008) data product outlined above. The N_i is calculated as the integral of a given parameterised ice particle size distribution, PSD, using DARDAR retrievals of ice water content (IWC) and N_0^* (a scaling parameter, see Sourdeval et al. (2018) for more details). In situ measurements of the PSD are used to evaluate the parametrised PSD used to calculate the N_i. The calculated N_i show good agreement with in situ measurements, with vertical distribution of concentrations of ice crystals larger than 5μm and 100μm (N_i^5 and N_i^{100}, respectively) showing physical consistency with a case study of a frontal system.

In this thesis, the vertical cloud fraction from the operational DARDAR product (Delanoë and Hogan, 2008), and the N_i^5 and N_i^{100} values from the DARDAR-Nice (Sourdeval et al., 2018) product are used in a qualitative manner in Chapter 3.

2.4 MODIS

The Moderate Resolution Imaging Spectroradiometer (MODIS) (Salomonson et al., 1989) is a sensor onboard NASA's polar-orbiting Terra and Aqua satellites. They have provided atmospheric and cloud properties continuously since 2000. The Terra and Aqua satellites have an equatorial overpass at approximately 10:30 and 13:30 local solar time (LST) during the day, and 22:30 and 01:30 LST during the night, respectively.

Both satellites view the entirety of the Earth's surface every 1-2 days.

In this thesis, 17 years (2000-2016) of MODIS Terra aerosol (Remer et al., 2005) daily level 3 data are used at 1x1°between 30S-30N to retrieve aerosol optical depth (AOD). The standard dark-target MODIS AOD retrieval 'Optical Depth Land and Ocean Mean' is used. The 'dark-target' algorithm is based on the idea that over dark surfaces, aerosols in the atmosphere can brighten the scene. This perturbation then allows the AOD to be calculated.

Chapter 3

Time Since Convection

Chapter Summary

- Time Since Convection (TSC) is introduced and used to investigate cloud properties, including vertical cloud evolution.
- TSC is shown to be independent of latitude for a given TSC bin, highlighting that proposed cloud evolution is due to changes along trajectories not just a shift away from the tropics to higher latitudes.
- The radiative evolution of high clouds is shown as a function of TSC, with a distinctive cooling to warming pattern, characteristic of detrained anvil cirrus.

The text and figures in this chapter are adapted from Horner & Gryspeerdt (2023). (Horner, G. and Gryspeerdt, E.: The evolution of deep convective systems and their associated cirrus outflows, Atmos. Chem. Phys., 23, 14239–14253, https://doi.org/10.5194/acp-23-14239-2023, 2023) The analysis and manuscript are my own work with comments and suggestions from Edward Gryspeerdt.

3.1 Introduction

The overall cloud radiative effect (CRE) in the tropics is small (Wielicki et al., 1996). However, this small net CRE is the combination of a large longwave (LW) warming that occurs due to ubiquitous thin cirrus clouds, and the large shortwave (SW) cooling that occurs due to optically thick convective regions. This leads to the CRE in cloudy regions being very similar to the CRE in nearby non-convective regions (Ramanathan et al., 1989; Harrison et al., 1990; Hartmann and Berry, 2017).

This cancellation, if a coincidence, could change in a warming world or under different aerosol concentrations with changes in deep convective regimes. Any small change in the LW warming from the thin cirrus, or the SW cooling caused by the deep convection itself, could potentially have a very large impact on the overall high cloud CRE in the tropics. Understanding the lifecycle and radiative evolution of deep convection is thus important to understand the sensitivity of these regimes.

The lifecycle of deep convective cores (DCCs) and their associated anvil and thin cirrus outflows has been investigated in numerous prior works, in both observations and models. Using observational data, Luo and Rossow (2004) found that 50% of tropical cirrus clouds originated from convection. Mace et al. (2006) found that 47% of cirrus observed over Manus Island in the western Pacific originated from deep convection occurring within the past 12 hours. Many other modelling and observational studies also showed that at least 50% of tropical cirrus originate from convection (Massie et al., 2002; Gehlot and Quaas, 2012; Riihimaki et al., 2012).

Studies investigating the model evolution of cirrus found broadly similar results to those found in observations. Gehlot and Quaas (2012) saw a rapid decay (6–12 hours) of deep convection from the peak and an associated growth of cirrus in the ECHAM5

model. After one day they found a decay of the cirrostratus, likely associated with a loss of cloud water due to larger particles that have a large sedimentation mass flux. Jensen et al. (2018) investigated the detrainment of ice crystals from the tops of deep convection in a cloud-resolving model (CRM). They found that most large ice crystals (¿200 μm in diameter) fall out of the anvils within two hours of formation. The cirrus decay was much slower, occurring over 120 hours, from a maximum cirrus cloud fraction of 0.4 to 0.15 after 120 hours. They also looked at changes under increased sea surface temperatures (SSTs), finding anvil cirrus clouds to have increased cloud fractions and higher cloud tops, leading to a positive cloud feedback.

When considering the CRE of the evolution of the convective system, it is the balance between the LW and SW over the entire lifetime of the cirrus in the tropics that, if perturbed, could lead to large changes in the overall net CRE. Most tropical radiative studies are confined to models. Looking at the CRE along Lagrangian trajectories in simulation, Gasparini et al. (2021) found that large SW and large LW values dominate close to convection, as expected. The net CRE oscillates close to zero and is a function of the solar insolation. In their simulations most convection occurs in the early morning, and there is a peak in net negative CRE at peak solar insolation when SW cooling dominates. There is a slight warming at 15 hours when the anvil has thinned sufficiently and the solar insolation decreased enough for the LW CRE to dominate.

The factors that control the radiative evolution of the decaying cirrus have also been investigated in model studies. Gasparini et al. (2019) found that at high (¿100 gm^{-2}) IWP (ice water path) values, or above the 80th percentile, the net CRE is negative. Beyond this, at low IWP and correspondingly low cloud fractions above 12 km, the net CRE switches signs to a small positive value. This switch occurs when the cloud optical depth is around 4, roughly where precipitation stops occurring. This is a lower value for cloud optical depth than found in observations by Choi and Ho (2006). As the CF

and IWP decrease, the CRE tends to zero. The switch from warming to cooling happens at around 6 hours from convection in Gasparini et al. (2019). They generally found that small-scale microphysical and dynamical processes are responsible for determining the lifecycle of the detrained anvil cloud. Current global circulation models (GCMs) have horizontal and vertical resolutions that are too coarse to accurately reflect the dynamical processes controlling anvil–cirrus evolution (Wall and Hartmann, 2018).

Most previous work focused on individual mesoscale studies and capped the analysis at shorter timescales in the region of 120 hours. In contrast, this thesis presents a method to run a Lagrangian trajectory analysis across the entirety of the tropics at unbounded trajectory lengths at a low computational cost, leading to changes being found in the cloud properties at timescales far beyond 120 hours after the initial detrained cirrus from convection has dissipated and in situ cirrus has formed. Used in conjunction with lidar and radar data, the vertical evolution of the cloud properties is characterised as a function of time since convection (TSC). The approach in this chapter builds a composite picture of the lifecycle from tropical convective into thin cirrus. This chapter also investigates how TSC is a function of latitude and shows that the changes in the cloud properties along trajectories are a strong function of TSC and are not simply reflective of latitudinal changes as air moves from the tropics to the extratropics. Finally, this chapter also considers the radiative evolution for just the high clouds along the trajectories.

3.2 Method

3.2.1 Data

Observational data from the 3-hourly International Satellite Cloud Climatology Project (ISCCP) H dataset at 1x1° is used to define locations of deep convection (Rossow et al., 2017). ECMWF ERA5 reanalysis wind fields are used in the trajectory analysis (Hersbach et al., 2018) and to characterise cloud properties. To examine the evolution of the radiative properties, the CERES SYN1deg L3 LW and SW TOA fluxes are used (NASA/LARC/SD/ASDC, 2017). The CERES SYN1deg product combines MODIS and geostationary satellite data to provide global coverage at a 1x1° resolution and 1 hourly temporal resolution.

To illustrate the vertical cloud evolution and microphysical properties the DARDAR dataset is used. N_i is highlighted from the DARDAR data due to the complimentary information it provides about cloud history compared to the large scale properties from ISCCP (Krämer et al., 2016). The period of study in this chapter is 2008-2010 inclusive. For a full description of these datasets, see the Chapter 2.

3.2.2 Deep convective core identification

In order to track the time since a parcel of air last experienced convection, convective cores were defined and identified in the satellite data. This chapter uses the global weather states in Tselioudis et al. (2021), which uses the ISCCP-H 1x1° daytime and nighttime 3 hourly dataset (Rossow et al., 2017). The ISCCP-H dataset is separated into seven distinct cloud regimes by calculating the nearest neighbours of each gridbox and

Regime	CTP / hPa	τ_c	CF / %
Deep convective cores	**242.6**	**10.5**	**99.5**
Mid latitude storm	433.6	10.4	99.2
Thin high cirrus	316.3	1.2	79.9
Polar	395.6	2.2	84.5
Middle top clouds	606.9	9.5	97.2
Fair weather	645.1	3.2	40.0
Shallow cumulus	840.1	4.0	79.6
Stratocumulus	725.5	6.3	90.7

Table 3.1: ISCCP-H cloud regime centroid values for the CTP, τ_c, and CF from Tselioudis et al. (2021). The deep convective cloud regime, DCC, is highlighted in bold.

clustering them into the separate regimes depending on their cloud fraction, albedo, and cloud top pressure. These cloud regimes, and their associated centroid values, are shown in Table 1. The albedo is calculated from the optical thickness using Equation 3.1.

$$\alpha = \frac{\tau_c^{0.895}}{\tau_c^{0.895} + 6.82} \tag{3.1}$$

as defined in the ISCCP simulator (Klein and Jakob, 1999). For a full description of the ISCCP-H weather states, see Tselioudis et al. (2021).

This study is focused on the tropical region of 30S-30N and only considers the deep convection defined within the tropics, whereas the weather states in Table 1 are defined globally. Note that the value of 10.5 for the optical depth centroid for the deep convection is typically lower than the optical depth of deep convective cores in high resolution satellite data. The ISCCP data used here is at 1x1°, and therefore the bins will have a lower average optical depth across the whole gridbox.

Additional conditions are applied to isolate the convective cores, requiring a $\tau_c > 8.5$ (albedo > 0.5) and a cloud top temperature (CTT) < 220K. Only the very brightest, thickest cores of the convective clouds are categorised as DCC. If these conditions aren't imposed then thick anvil cirrus are included as part of the convective cores, and the ability to investigate their temporal development is reduced.

The mean relative frequency of occurrence (RFO) for the convective cores for the years 2007-10 is shown in Figure 3.1. Most of the convection occurs in the Maritime Continent, over Central Africa, South America, and along the ITCZ. This thesis is only concerned with tropical convection, defined in the region between the red boundaries (30S-30N).

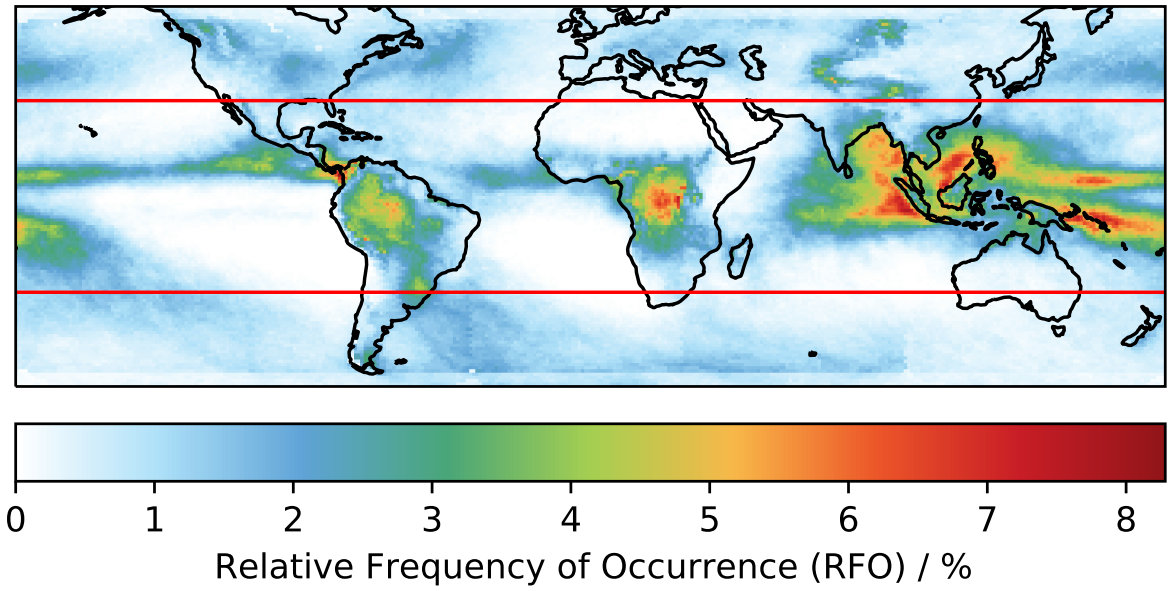


Figure 3.1: Relative frequency of occurrence (RFO) of the convective core regime from between 2007-2010. Red bands show the boundaries of the tropics (30S-30N).

3.2.3 Time Since Convection

The ECMWF ERA5 reanalysis wind speeds at 0.25° are used in this study (Hersbach et al., 2018). A pressure averaged wind field between 200hPa and 300hPa is used to advect the convective cores forward, in order to best reflect the range of heights that the convective cores and subsequent detrained and in situ cirrus exist. This is the same logic as applied in Luo and Rossow (2004), where vertical movement of air is not considered, however they use a pressure averaged wind field between 200hPa and 500hPa. The decision to use a higher altitude average wind field is addressed in section 3.2.5.

The advection process is as follows. All the pixels in the tropics are advected forward one hour in time according to the wind field. The TSC now has values of T+1 hours since convection. In locations where DCC are present, the TSC is reset to zero. This advection process repeats, each time resetting locations of DCC to zero TSC. Figure 3.2 show a schematic diagram of the process in one dimension.

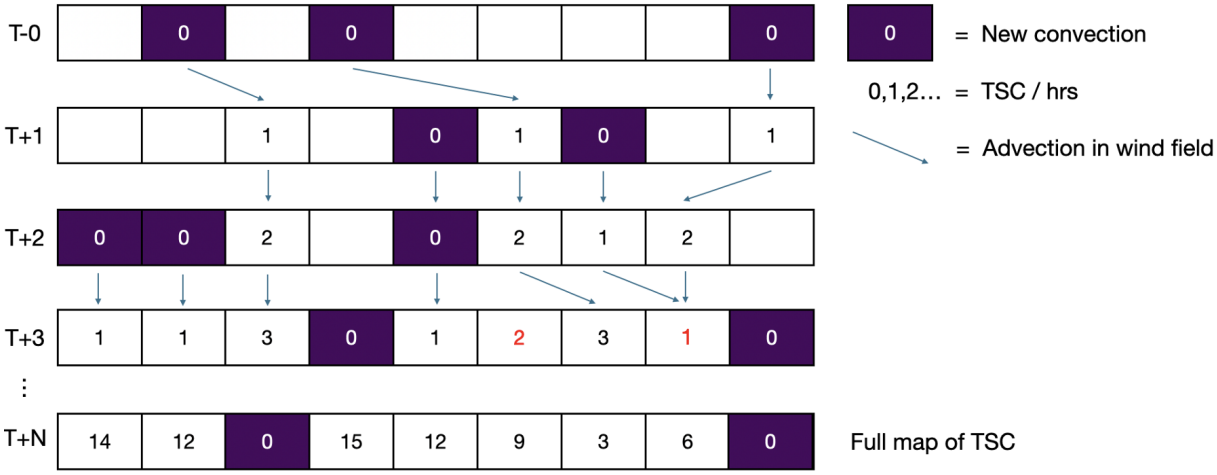


Figure 3.2: Schematic diagram of the advection process in one dimension, assuming all locations start with no TSC value. Red values indicate where either a divergence or convergence of pixels occurs. The purple boxes show new convection occuring, and the arrows highlight the advection of convective air into new gridboxes between timesteps. The values of the TSC are shown in each box.

The TSC algorithm runs at 0.1x0.1° resolution. Running the TSC code at 0.1x0.1° is necessary to ensure that between one hour timesteps there is a high enough resolution so that parcels are advected out of the pixels they currently occupy. If the algorithm was run at 1x1°, large discretisation errors would be introduced, as air would very rarely travel out of the pixel that it occupies within a single hour-long timestep. For this reason, the resolution of the DCC dataset is increased to 0.1x0.1° using a nearest-neighbour interpolation to be compatible with the TSC algorithm. The resolution of the outputted TSC files is averaged to 1x1° to be compatible with the MODIS and CERES gridded products.

The TSC array is interpolated into missing regions after each advection timestep (Fig-

ure 3.2). When each 0.1x0.1° pixel in the TSC array is advected forward, some of the trajectories converge to occupy the same pixel, necessarily leaving some pixels without a TSC value. When this occurs, the missing values are interpolated as an average of TSC values around this empty pixel. Between each timestep, divergence leaves approximately 5% of the pixels empty. When two trajectories enter the same pixel, they will proceed to follow the same trajectory ad infinitum due to the deterministic nature of the trajectories. Therefore the trajectory with the smaller TSC value is the one that determines the TSC value at that pixel from that point on. This increases confidence that any high TSC value really represents air at such long timescales since convection.

The TSC map is defined between 32S-32N to ensure that air is allowed to briefly leave the region of analysis and reenter. If the wind field brings air from outside 32S-32N into this region, this new air will not be assigned a TSC value until it meets new convection or advection introduces a TSC value. This increases confidence in the high TSC regions. If TSC is defined well beyond the tropics, the extratropics act like a reservoir of very high TSC values that are occasionally advected back into the tropics. This inflates the TSC values, because no convection is defined outside of 30S-30N.

As TSC is initially undefined, there is an associated spin up time until every point is a true reflection of the hours since the air at that location last experienced convection. This spin up time is shown in Figure 3.3 and is approximately 20 days. Therefore in all further analysis, the first month of data are excluded.

3.2.4 Detrained v in situ cirrus

Not all of the cirrus along the advected air parcels will have detrained directly from the convective cores. Therefore it is useful to to have an indicator for what percentage

of the cirrus are detrained for a given TSC. To do this a 'cirrus type' value is assigned to each gridbox where detrained cirrus is present. Initially, all cirrus are considered to be detrained. Once the ISCCP cloud fraction drops below 10% along a given trajectory, any cirrus that forms subsequently is considered to be in situ in origin. This cirrus type value doesn't necessitate that a cirrus cloud be present in the gridbox, just that the cloud fraction of the detrained cirrus has dropped below 10% at some point, meaning that any subsequent cirrus that forms is in situ. This is a similar method used in Luo and Rossow (2004), who use a threshold of 20% of the maximum cirrus cloud fraction along a trajectory to identify the 'zero detrained cirrus' case, rather than a 10% cloud fraction threshold as used in this thesis.

3.2.5 Evaluation of TSC

After the spin up, there is minimal variability in the TSC across two years of data, with the mean TSC oscillating around 180 hours (Figure 3.3). The 10th percentile is very consistent, due to the regularity of new convection occurring in the dataset. The 90th percentile is more erratic, oscillating between 350 hours and occasionally over 500 hours, due to the sporadic nature of the occurrence of very high TSC regions and the long tail on the distribution of TSC.

It is interesting to note that the 90th percentile TSC values are considerably higher than the temporal length of the trajectories in prior works (Gehlot and Quaas, 2012; Luo and Rossow, 2004). Both of these studies limited their analysis to 120 hours (5 days), which included only 30% of tropical locations (Figure 3.3b). This is a benefit of the TSC approach, which allows the trajectories to be computationally efficiently advected without an upper bound to their length, so does not bias the results towards shorter trajectories and allows for the investigation of clouds that form along the air

parcels from convection after the detrained cirrus have dissipated.

Figure 3.3b shows that there is a sharp decrease in the number of gridboxes containing detrained cirrus clouds, after an initial peak around 12 hours from convection. This is in agreement previous studies that investigated detrained cirrus lifetimes (Luo and Rossow, 2004). Although there are still some detrained cirrus at very long TSC values (more than 100 hours), most of the cirrus forming at this point are not directly detrained from convection.

3.2.6 Comparison with HYSPLIT trajectories

A comparison can be made to individual trajectories initiated from locations of convection. The HYSPLIT Lagrangian forward trajectory model is used in this chapter (Rolph et al., 2017). The HYSPLIT model uses reanalysis data from NCEP/NCAR to advect individual air parcels in a 3D wind field, which includes vertical transport of the air parcel. In this chapter, HYSPLIT trajectories are initiated from the centre of each 1x1° box that contains a TSC-0 value, at an altitude of 10km. These trajectories are followed for 315 hours, with the TSC time at the location of each trajectory compared the time since the HYSPLIT trajectories were initiated. This is done for three complete days across 2008 (Jan 1st, Jun 1st, and Sept 1st). Figure 3.4 shows the median value of the TSC for the gridbox occupied by the trajectories. The dotted red line indicates all the trajectories initiated from the convective cores (1033 in total), ignoring any new convection along that trajectory. The solid blue line only includes trajectories up to the point at which they next experience convection, which better represents the TSC methodology.

The TSC value and HYSPLIT trajectory time broadly match for lower TSC values (Fig-

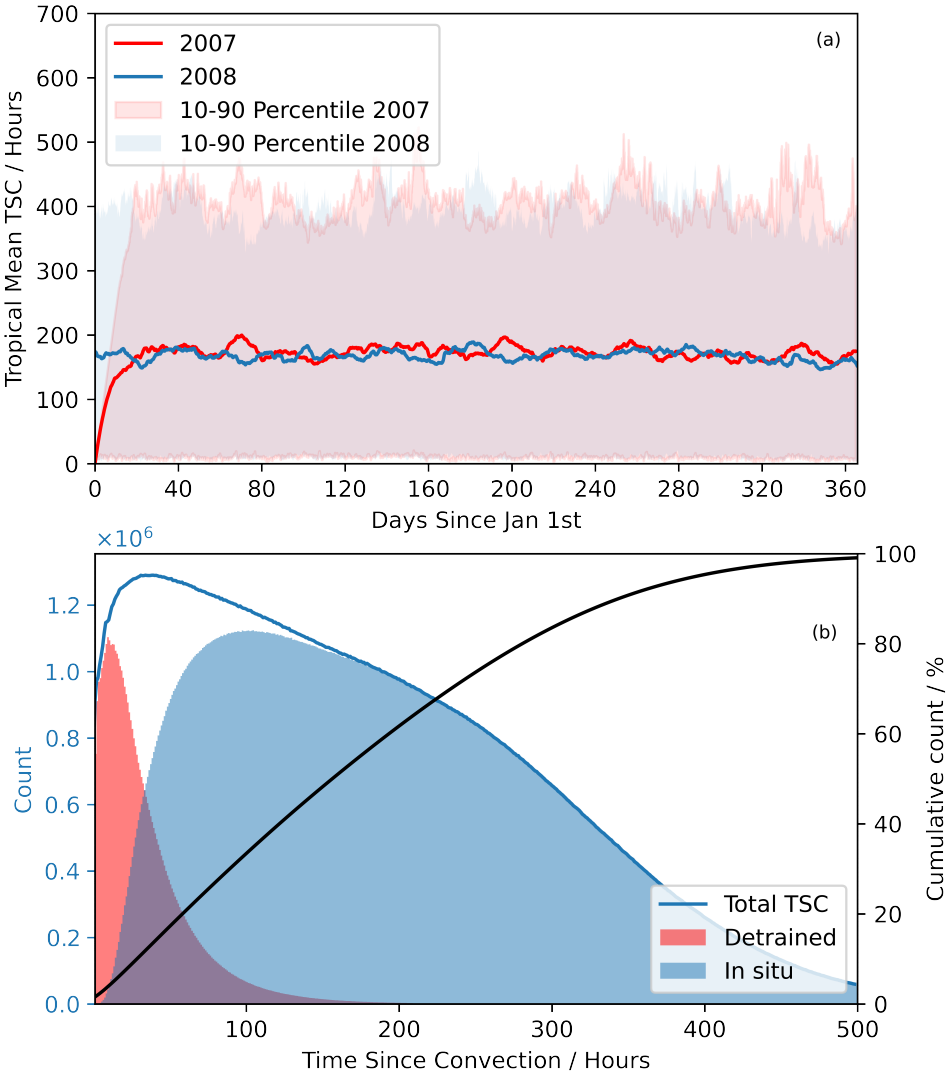


Figure 3.3: a) Tropical mean Time Since Convection (TSC) for 2007 and 2008, with 10th-90th percentiles highlighted. The top right histogram shows the normalised distribution of TSC values over the 2 year period, excluding the spin up time. There is little variation in the mean TSC between the years after the initial spin up period in 2007. b) Histogram of TSC values between 2007-2010 between 0 and 500 hours. Red indicates the fraction of gridboxes that contain detrained cirrus, blue are candidates for in situ cirrus formation. Right axis shows the cumulative distribution in percentage of all TSC values. >99% of TSC values are less than 500 hours.

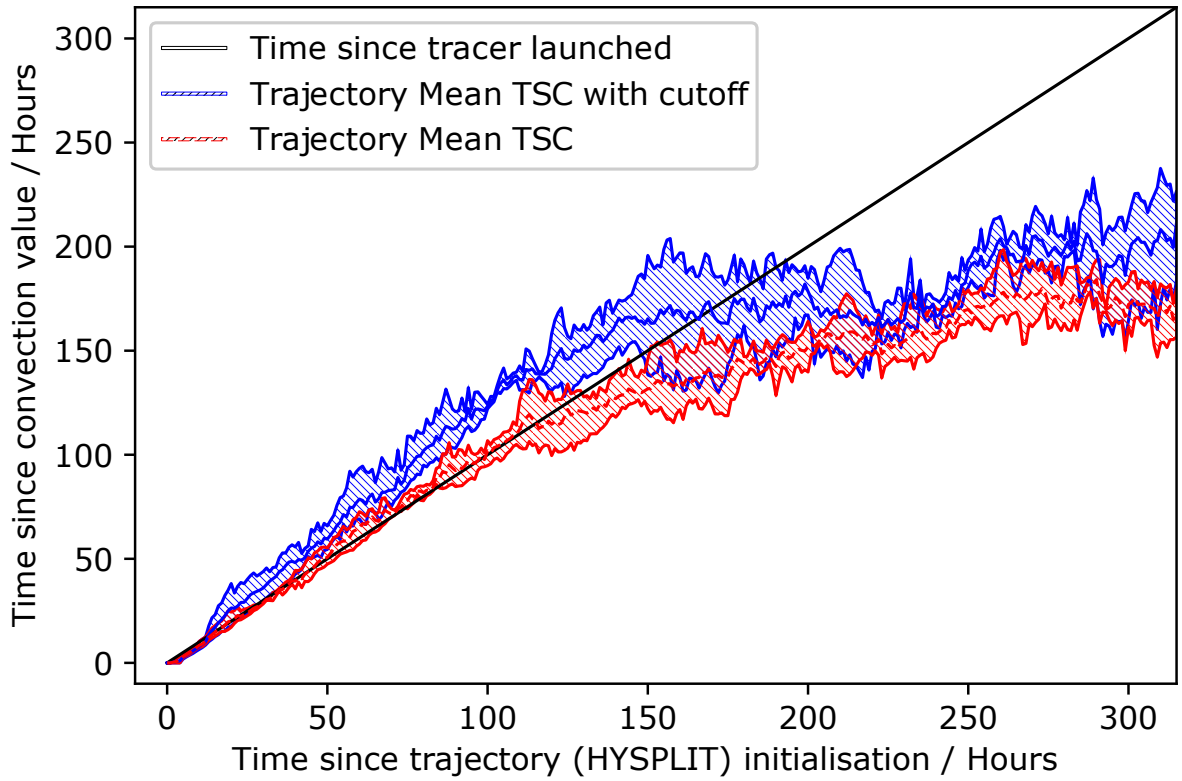


Figure 3.4: Median TSC values (y-axis) along HYSPLIT trajectories (x-axis), for all trajectories and for trajectories that are stopped once they reach new convection. Error range between maximum to minimum trajectory values. Straight line indicates an exact relationship between trajectory age and TSC value.

ure 3.4). However, particularly for the trajectories that stop when they experience new convection, the TSC values are higher than the time since the trajectories are initiated. The main reason for this difference is there is no vertical transport in the TSC advection algorithm. Rather, the average wind speeds between 200hPa-300hPa are used to advect the air parcels. The trajectories in the NCEP/NCAR HYSPLIT model are initiated at an average pressure of 200hPa. This height is an approximation of the DCC detrainment altitude, which leads to some uncertainty in the relevant wind level for advection. During the early stages of the HYSPLIT trajectory, the HYSPLIT wind speed will be greater than that used for the TSC trajectory. This is because the HYSPLIT trajectory is at 200hPa and the TSC trajectory wind speed is averaged between the 200hPa and 300hPa wind speeds.

This explains why the TSC is greater than the age of the trajectories, as the faster HYSPLIT winds will move further from convection than modelled by the TSC dataset. As the trajectories subside (it is worth noting that there is uncertainty in the appropriate subsidence rate), the horizontal wind speeds decrease, and start to become closer to the wind speeds in the TSC dataset, therefore the difference between the age of the trajectories and the TSC becomes constant. As the trajectories begin to subside even more, the TSC values become closer to the age of the trajectories, until at around 150 hours where the TSC value becomes lower than the age of the trajectories. This close comparison between the TSC and HYSPLIT trajectory times justifies the use of the 200-300hPa pressure levels, rather than the broader range of pressure levels used by Luo and Rossow (2004).

3.2.7 Cloud Properties

The ISCCP-H dataset is used to investigate how the CTP and τ_c change as a function of TSC, making use of the joint histograms of CTP-$\tau_c$in the ISCCP product. These show cloud fraction for a range of CTP and τ_c bins, produced at the pixel-level and limited to show the evolution of the tropical gridbox mean values for the region between 30S-30N. The joint histograms are used to isolate the highest clouds, retaining only the top 3 CTP bins of the histogram (¿375hPa). This is done by multiplying the centroid value of the top 3 CTP bins by the cloud fraction of each bin from the joint histograms. This allows for a comparison for the evolution of the τ_c and CTP for all clouds, and just the highest clouds in the tropics.

Failed retrievals in the ISCCP-H dataset, are assigned to the lowest τ_c and CTP bin in the joint histogram. The bin containing these missing values significantly affect the high cloud τ_c and CTP, so is removed when generating the τ_c and CTP histograms in

Figure 3.7.

The vertical profile of the cirrus is investigated using the DARDAR dataset, a combination of the CloudSat radar and CALIPSO lidar (Delanoë and Hogan, 2008). The overpass locations of DARDAR are matched within the hour to the TSC at that location, at 1x1° resolution. A 1x1° can contain many DARDAR retrievals, each of these DARDAR retrievals is assigned the same TSC value - that of the 1x1° gridbox. These DARDAR retrievals then all contribute equally to the analysis in the relevant TSC bin. The DARDAR cloud mask is used to filter out aerosol, ground, and unknown retrievals. The DARDAR-Nice product (Sourdeval et al., 2018) is used to provide the vertical profile of ice crystal number concentration (N_i) for crystals larger than 5um (N_i^5) and larger than 100um (N_i^{100}).

The radiative evolution of convection, from thick convective core to thin anvil cirrus, is investigated by analysing the CERES SYN1deg L3 LW and SW TOA fluxes (NASA/LARC/SD/ASDC, 2017). The CRE is calculated as the all sky minus clear sky radiative fluxes from the CERES data. In order to only look at the radiative evolution of the highest clouds, regions where the cloud fraction of the low clouds (as defined by the ISCCP joint histograms) is less than 1% are classified as 'high cloud only' gridboxes. For the cloudiest regions in the tropics (which are also the regions of the lowest TSC), there is often no hourly outgoing clear sky LW data. For these gridboxes, the 3 monthly seasonal average outgoing clear sky LW for these gridboxes is used, in order to calculate a value for the CRE.

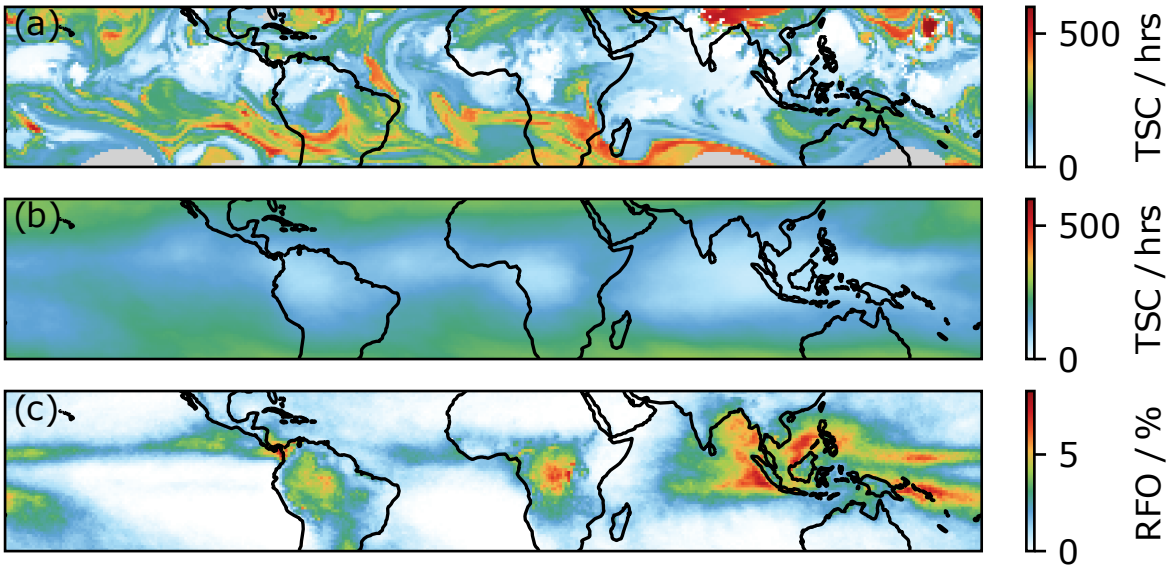


Figure 3.5: a) Snapshot of the TSC 30S-30N at 00:30UTC 26th July 2008. b) Mean TSC for between 2008-2010. c) RFO of deep convection between 2008-2010.

3.3 Results

3.3.1 Regional distribution of Time Since Convection.

Figure 3.5 shows the map of time since convection for the tropical region 30S-30N at 00:30 UTC on Jan 1st 2008. As might be expected, the TSC map broadly follows the geographical distribution of the deep convective cores shown in Figure 3.1. The areas of low TSC, such as the Maritime Continent, South America and Central Africa align with the regions of high DCC occurrence. However the low TSC regions are more spread out around the regions of DCC occurrence, as they are advected via the wind field away from the initial DCC. Regions of particularly high TSC are the extra tropical regions around 30S and 30N latitudes, far from convection.

3.3.2 Evolution of ISCCP cloud properties

As the optically thick deep convective cores dissipate, a reduction in the cloud optical thickness (τ_c) is expected following previous studies (Luo and Rossow, 2004), as the anvil cirrus decays into thin cirrus and eventually disappears completely. Changes in the cloud top pressure (CTP) are also expected, moving from low pressure (high altitude) close to the convective core, to higher pressures (lower altitude) as the anvil cirrus extends and sinks (Luo and Rossow, 2004).

Figure 3.6 shows the ISCCP-H joint histograms in the first 5 days since convection, with each 24 hour period showing the joint histogram of CTP and τ_c. At day 0 (0<TSC<24) the histogram is dominated by optically thick, high altitude clouds, with high cloud fractions. There is very little low cloud, which may be due to the thick high cloud obscuring the clouds below them. However, low clouds become visible in the first 24 hours since convection. There is a shift to optically thin clouds as TSC increases. This implies that the thick anvil cirrus clouds do not persist longer than 24 hours post convection, consistent with previous studies by Luo and Rossow (2004). This is supported by Figure 3.6, showing the difference is largest between day 0 and day 1 than any subsequent day. High clouds with an optical thickness in the middle two bins (between 2.3 and 14.5) representing the thicker cirrus outflow are still noticeably persist up to day 5, with the most significant decrease in their cloud fraction happening 3 days after convection. They remain with low cloud fractions up to day 25.

From day 4 onwards, low clouds begin to dominate in the joint histogram, however there is still a presence of thin cirrus. Interestingly, small changes in the cloud fractions are still seen between day 10 and day 15, particularly an increase in low cloud and decrease in high cloud. This implies that the TSC is still influential at up to 360 hours from convection. Note that the top left bin (high, optically thin cloud) remains

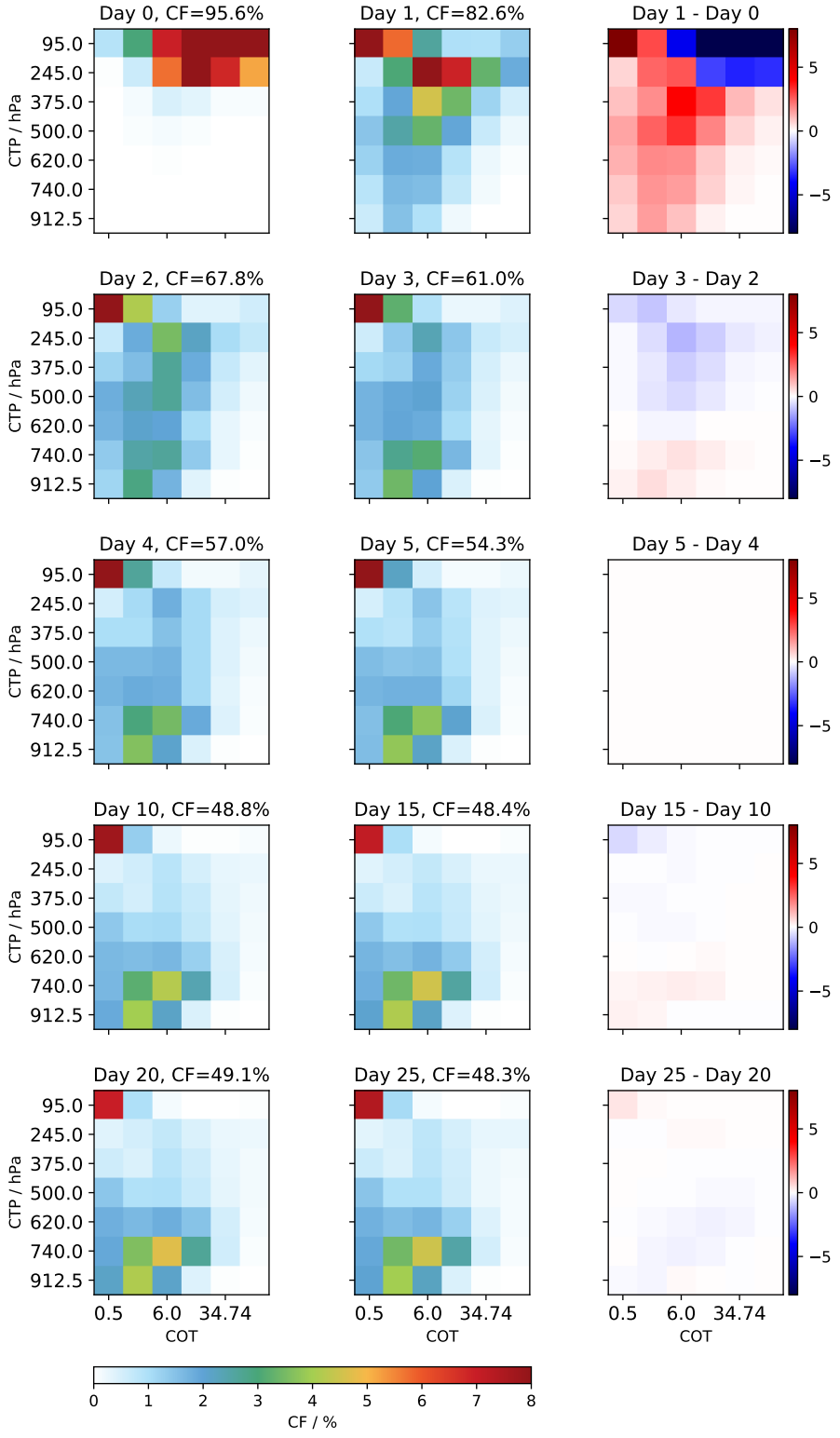


Figure 3.6: ISCCP-H joint histograms showing the distribution of the CTP, and τ_c and cloud fraction as a function of days since convection. The rightmost column shows the absolute percentage change between days. Day 0 is the first 0-24 hours since convection, day 1 is 24-48 hours since convection, and so on. High CF values for upper right gridboxes would indicate a distribution skewed towards optically thick, high altitude clouds, and the opposite (optically thin, low altitude), for bottom left. Note that the top left bin also contains unreliable data, so gives an unrealistically large cloud fraction.

particularly frequent across all histograms. This is due to the failed retrievals. These can't be assigned into a particular τ_c/CTP bin and so are assigned into top left bin in the ISCCP-H dataset by default (Pincus et al., 2012).

These results are generally consistent with previous work (Gehlot and Quaas, 2012; Luo and Rossow, 2004), however this chapter sees a slightly quicker decay of the anvil cirrus than in Luo and Rossow (2004), and continued changes in cloud fraction beyond 5 days from convection. Luo and Rossow (2004) use a column averaged wind field between 200hPa-500hPa, whereas this chapter uses 200hPa-300hPa to better reflect the range of heights at which the detrained thin cirrus and in situ cirrus occur at. The wind field in this chapter will be on average faster than Luo and Rossow (2004), and therefore the air will travel further in the same period of time. As such a TSC value of 10 hours will be geographically further along the trajectory than in Luo and Rossow (2004). This will cause the lifetime of the convective outflow clouds to appear shorter in this chapter and may explain these differences.

Seeing changes in the cloud fraction at such long TSC values is a consequence of the approach of this thesis. Unlike previous studies, where the trajectories were stopped at predetermined times, this thesis tracks air from convection for an unbounded amount of time. Therefore changes in cloud properties can be tracked at much longer times since convection than previous work, without having to pick out specific convective events that are known to reach a certain age. The TSC methodology also explicitly deals with scenarios in which a trajectory is overlapped by new convection.

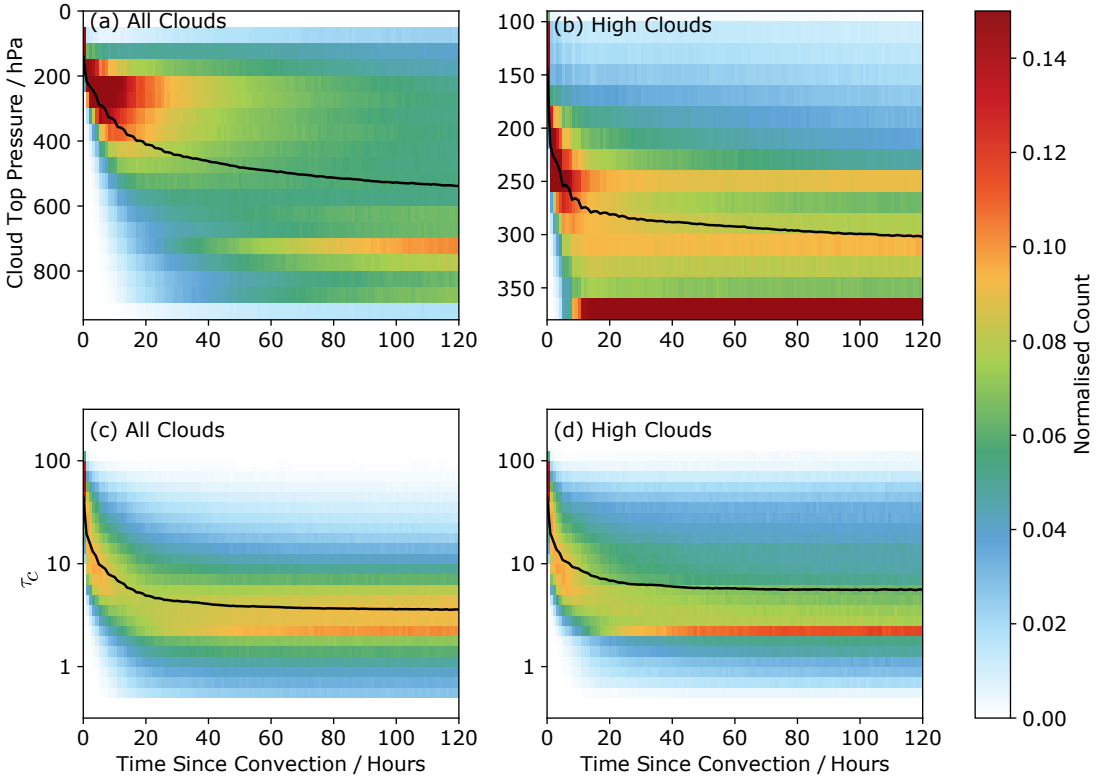


Figure 3.7: ISCCP cloud properties as a function of TSC. The normalised distribution represents the probability of finding clouds with a particular CTP or τ_c for a given TSC value. The black line indicates the mean value. Left-hand column shows the CTP and τ_c for all clouds, and right-hand column for high clouds only.

3.3.3 Evolution of cloud properties

Figure 3.7 shows the evolution of the CTP and τ_c respectively as a function of the TSC for both all cloud gridboxes (Figure 3.7a,b) and the high cloud only gridboxes (Figure 3.7c,d). The joint histograms are normalised so that the number of y-axis bins add up to unity, to account for the fact that there are more retrievals for smaller TSC values. This provides a higher temporal resolution than the histograms in Figure 3.6.

Figure 3.7a shows that the CTP initially sits at very high altitudes for the convective cores, around 200hPa, coincident with the upper level wind field used. There is an large increase in the mean CTP in the first day since convection, as the convective

core thins, and the mean CTP is skewed by the optically thicker lower altitude clouds (shown in Figure 3.6). The histogram still shows a presence of higher altitude clouds, with an increasing proportion of low altitude clouds further from TSC-0 (the convection itself). There is still a decreasing CTP at 5 days from convection.

Isolating just the high clouds using the ISCCP histograms, Figure 3.7b shows a similar decline in the mean CTP, albeit at lower pressures. The τ_c also sits at 200hPa initially, decaying to 250hPa in the first 6-12 hours as the convective core dissipates. The decay then slows, reaching 300hPa at 120 hours from convection. There is a significant cloud layer at 370hPa that becomes visible as the high cloud dissipates. These are likely clouds not directly detrained from convection that become visible as the cloud fraction of the anvil cloud above decreases, and any changes in the properties of these clouds, particularly at large TSC values, are not suggested to be directly related to the initial convection.

Figure 3.7c shows the evolution of the cloud optical thickness for all clouds. The all cloud τ_c drops significantly in the first 24 hours from convection, indicating the dissipation of the very thickest high clouds associated with the convective cores. This is to be expected as the regime shifts from thicker cirrus associated with convection, to thin cirrus that persists either after a convective event, or is formed in situ and unrelated to convection.

When just looking at high clouds in Figure 3.7d, the mean values of the histogram are relatively unchanged. However there is larger spread in the cloud optical thicknesses, including a relative increase in the optically thinnest of the clouds in the lowest bin.

3.3.4 Vertical profile evolution

The vertical distribution of cloud and N_i vary strongly as a function of TSC. Figure 3.8a shows the cloud amount and thus the general anvil shape of convective cores and their associated cirrus outflow up to 120 hours from convection. Figure 3.8b shows the same up to 500 hours from convection. At very low TSC (TSC<2hr), there is a substantial amount of cloud at all altitudes up to approximately 16km associated with the very tops of the convective towers. It should be noted that this cloud amount is not comparable to the ISCCP cloud fraction used to identify the deep convection. The low to mid altitude cloud, likely the convective cores, quickly dissipates as the TSC increases. High clouds are maintained for much longer, with changes in the high cloud fraction continuing beyond 120 hours from convection. There is a moderate amount of low clouds, almost independent of TSC. There is also a sustained amount of mid level clouds between 4 and 8km for the first 60 hours. These mid level clouds are thought to form when latent heat associated with convective freezing creates a shallow temperature inversion which slows vertical motion in subsequent convective cycles and detrains moisture near the freezing level (Bourgeois et al., 2016). Figure 3.8b shows that even at very long TSC values, beyond 120 hours up to 500 hours, there is still a significant change in cloud amount as a function of TSC.

Figure 3.8c shows the ice crystal number concentration for particles greater than 5μm in diameter, (N_i^5), as a function of the time since convection. Figure 3.8e shows the same as Figure 3.8c but for those greater than 100μm, (N_i^{100}). Given that the N_i is a very strong function of temperature (and therefore altitude), it is useful to consider the relative changes in the N_i as a function of TSC. Figure 3.8d and 3.8e show the deviation of the N_i from the tropical mean N_i for a given altitude. Red indicates where the N_i at a given TSC is greater than the tropical mean, and blue those regions where it is less than the tropical mean.

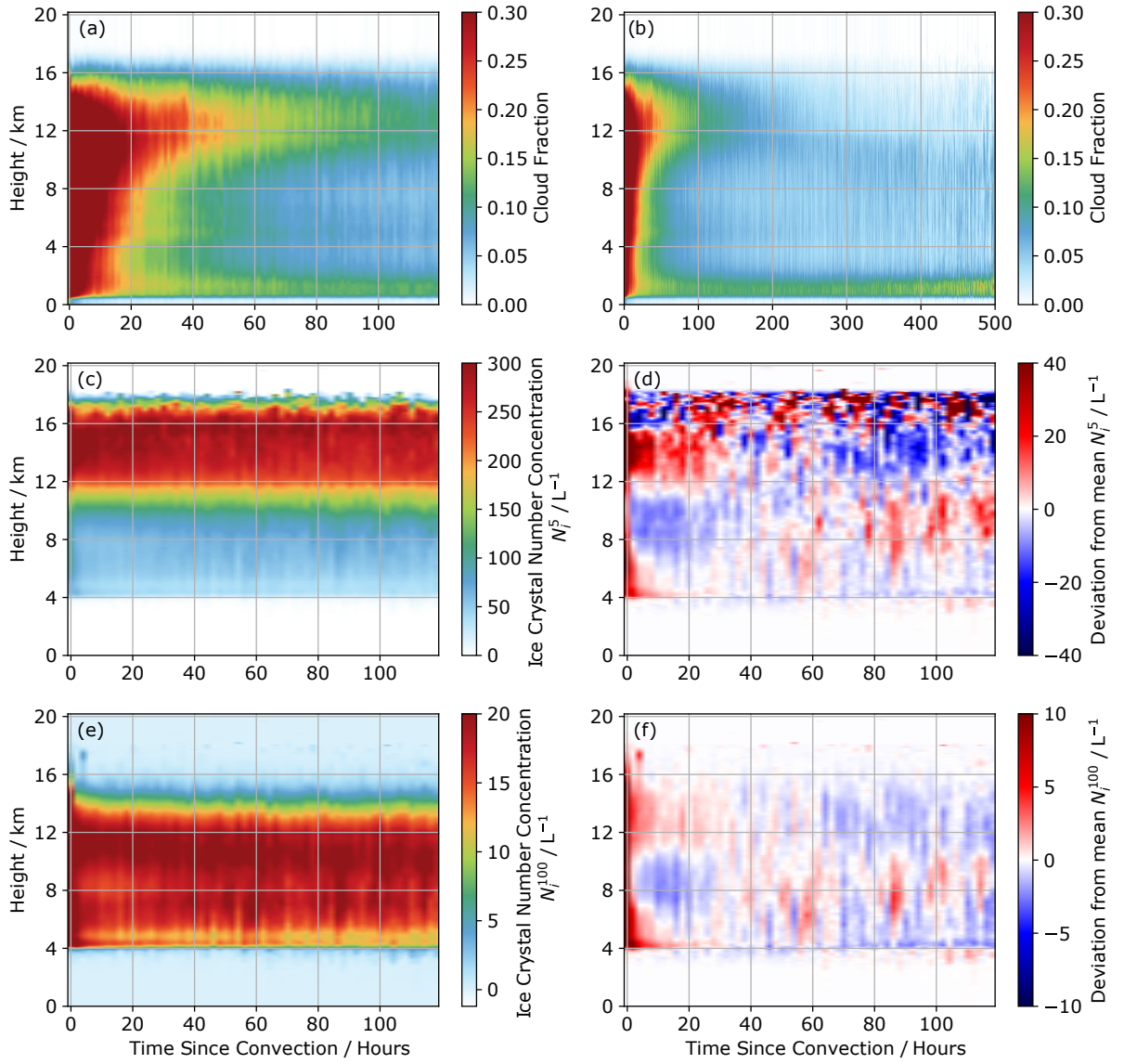


Figure 3.8: Vertical evolution of DARDAR cloud properties as a function of TSC. a) Cloud fraction up to 120 hours from convection. b) Cloud fraction up to 500 hours from convection. c) N_i for particles larger than 5μm. d) N_i^5 anomaly for 120 hours from convection. e) N_i for particles larger than 100μm. f) N_i^{100} anomaly from mean value for 120 hours from convection. Anomaly here refers to the difference in the N_i at a given TSC to the mean N_i at that altitude for the tropics.

Considering Figure 3.8d first, there is an greater than average N_i^5 at all altitudes close to convection. This is most notable between 12km and 16km, where the N_i^5 peaks. This is to be expected given the presence of a deep convective core. At short times after TSC-0, there remains an above average N_i^5 between 12km and 16km. This is indicative

of the convective outflow that remains after the convective core has dissipated. This outflow decays within 36-42 hours, when the deviation to the mean N_i^5 becomes negative. There is also an increase in N_i^5 at similar times at lower altitudes (between 4km and 8km) that decays within around 20 hours. This is likely due to the active shallow convection that occurs close to the region of deep convection, and thin mid level clouds discussed in Bourgeois et al. (2016). Considering Figure 3.8f, there is a clear increase in the N_i^{100} close to convection, particularly at lower altitudes between 4km and 8km. Although the DARDAR retrieval is less reliable in convective cores (Delanoë and Hogan, 2008), larger ice crystals are expected in the convective core at lower altitudes as they are less likely to be lifted higher into the cloud column than smaller ice crystals, and also subside quicker (Jensen et al., 2018). The lower altitude N_i^{100} drops off rapidly as the convective core dissipates. As in the case of the N_i^5, there is an increase in the N_i^{100} between 12km and 16km which is sustained for the first 24 hours from convection and linked to updrafts of large ice crystals from deep convective cores. In both of these figures there appears to be anomalies after 36-42 hours from clouds not directly detrained from convection. This is expected, as not all high clouds are detrained from convection or change as a function of TSC, as shown in Figure 3b many of the cirrus clouds that form along the trajectories form in situ after the detrained cirrus have dissipated.

It is worth noting that N_i depends on many drivers that may not be related to TSC. These drivers may be supersaturation, cloud updrafts, ice nucleating particle (INP) concentration, and whether the origin of the ice crystal is liquid or in situ in origin. Naturally, this makes the relationship between N_i more challenging to show compared with INP, as many more of these drivers need to be disentangled. This partially explains the noisy results in Figure 3.8d and 3.8f.

3.3.5 TSC as a function of latitude

It is clear from Figure 3.5b that on average TSC increases with latitude, expected from the large-scale behaviour of the Hadley circulation. However, while latitude can explain the broad features of the high cloud field, TSC offers valuable additional insight into the development of high clouds, more closely constraining their properties and development.

Figure 3.9a shows the zonally averaged DARDAR cloud fraction in the tropics for all gridboxes with a TSC value between 0 and 6 hours. Close to convection, it is clear there is very little latitudinal dependence in the cloud profile when when controlling for TSC. As TSC increases during the first 24 hours from convection (Figures 3.9b,c), latitude starts to become relevant for determining the cloud profile, although the impact is still small. At three days from convection (Figure 3.9d), the zonal cloud fraction begins to resemble the average tropical climatology. Despite this, there are still clear changes in cloud fraction as a function of TSC at a given latitude, even several days after convection (Figures 3.9e, f).

This demonstrates that the results shown in Figure 3.8 are not purely due to the correlation between TSC and latitude. In contrast, TSC provides significant additional information about the state of the cloud field. In all regions of the tropics, the temporal evolution of clouds following convection is critical to understand high cloud properties.

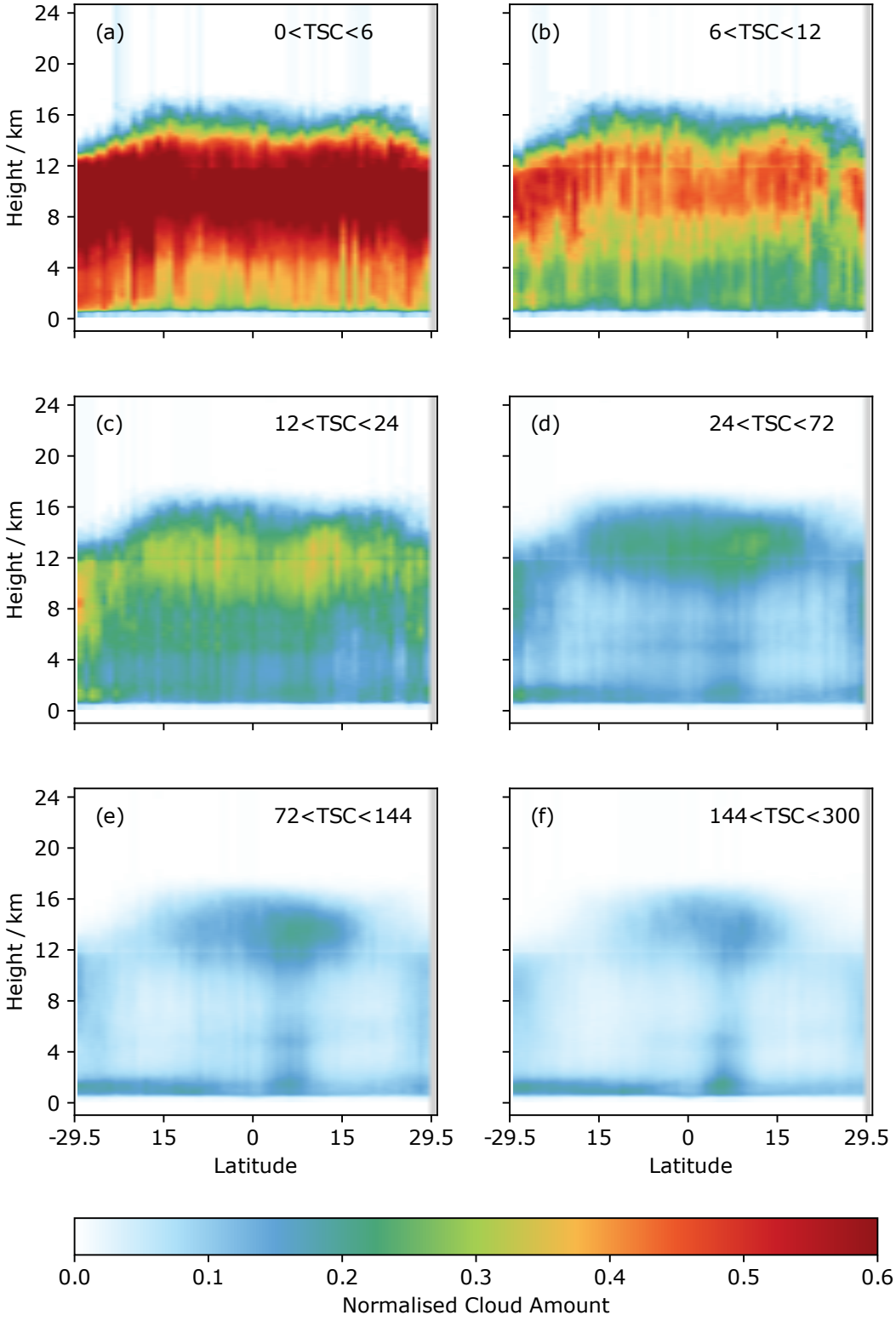


Figure 3.9: Zonally averaged DARDAR vertical cloud amount for a given TSC bin. TSC bins are given in the top right corner.

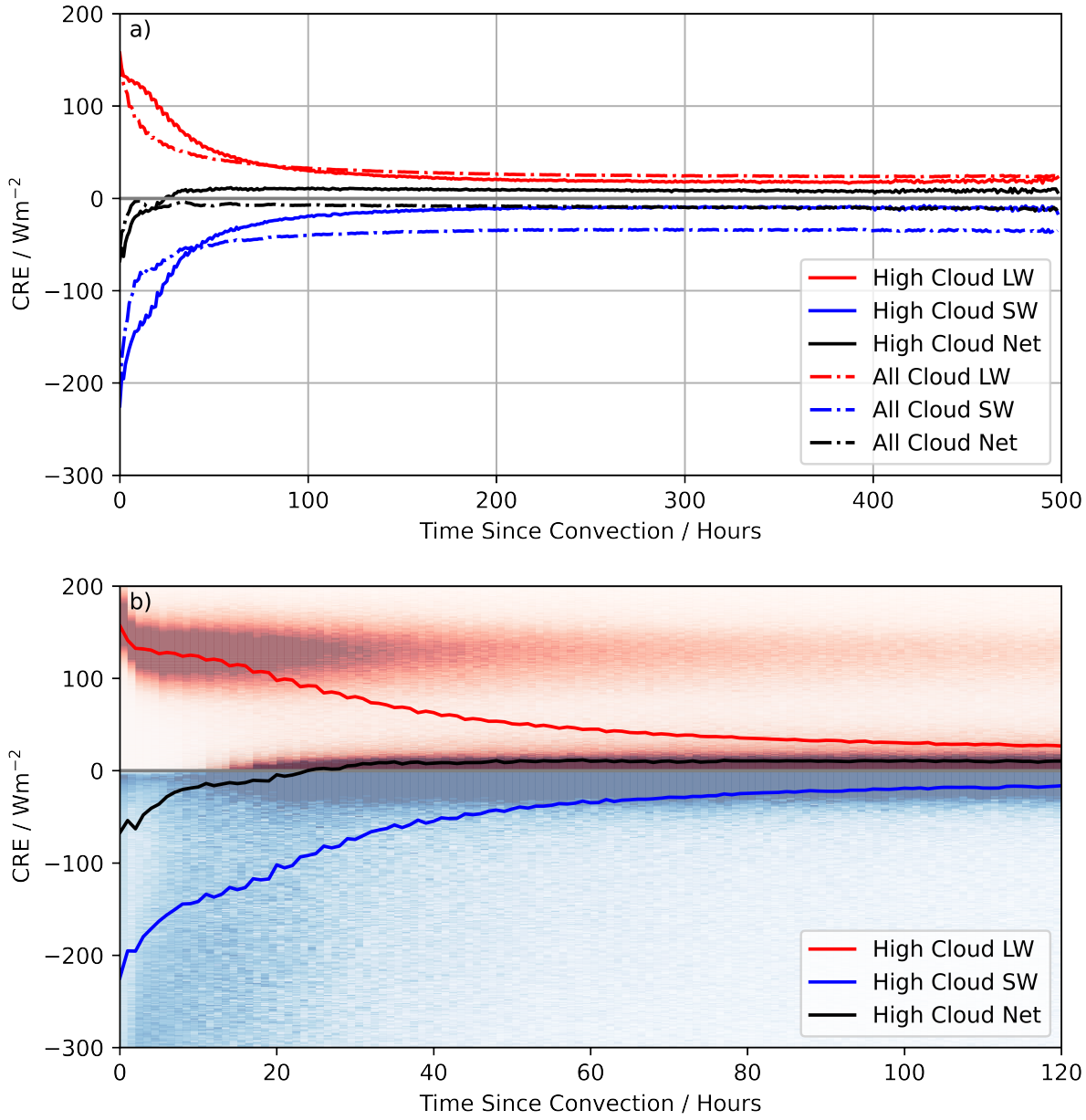


Figure 3.10: Cloud Radiative Effect (CRE) as a function of TSC. a) All cloud and high cloud LW, SW and Net CRE up to 500 hours from convection. b) High cloud LW, SW and Net CRE up to 120 hours from convection with normalised joint histogram showing the probability of finding a particular CRE value (LW in red, SW in blue) for a given TSC value.

3.3.6 Cloud radiative effects

The radiative evolution of convection, from thick convective core to thin anvil cirrus, is characterised by analysing the CERES SYN1deg L3 LW and SW TOA fluxes (NASA/LARC/SD/ASDC, 2017). Figure 3.10 shows the SW, LW and net cloud radiative effect (CRE) as a function of the time since convection. Figure 3.10a shows the evolution of the LW and SW and NET CRE for both the all cloud gridboxes, and gridboxes containing only high cloud, up to 500 hours from convection.

Figure 3.10a shows that when considering the all cloud CRE, the net CRE is always slightly cooling, with an oscillation in the first 48 hours due to the diurnal cycle in the CRE. This net CRE of close to zero in the tropics is well studied (Ramanathan et al., 1989; Hartmann and Berry, 2017; Wielicki et al., 1996). In the all cloud case, there is initially a very large significant warming and cooling that cancel each other out. The LW and SW CRE decreases significantly in the first 24-48 hours as the cloud fraction of these clouds drop (Figure 3.8a). By 100 hours from convection there is very little change in the all cloud and high cloud CRE. To understand how the radiative forcing of the clouds that evolve from convection change, it is vital to consider only the gridboxes containing high clouds.

The high cloud CRE is a strong function of TSC at very low values of TSC (Figure 3.10b). Initially, there is a large SW and LW component to the CRE, with -210Wm^{-2} SW cooling and 150Wm^{-2} LW warming at TSC-0, leading to a net CRE of -70Wm^{-2} cooling. This is due to the very optically thick convective core that reflects a significant portion of the incoming solar radiation (Figure 3.7d), whilst also having a very large LW warming due to its high cloud tops (Figure 3.7b).

As the convective core dissipates and the cloud optical thickness decreases, the SW

CRE drops significantly, to 100Wm^{-2} at 20 hours from convection, whereas the LW warming remains around 90Wm^{-2}. At 24 hours from convection, the net CRE shifts from a cooling regime to a warming regime, dominated by the LW warming of the thinner detrained cirrus in the initial stages of TSC, and then sustained by in situ cirrus formed along the trajectories. After the initial dissipation of the core, the net warming is sustained. After 24 hours since convection, the net CRE remains at 10Wm^{-2}. The histogram in Figure 3.10b shows the LW warming splitting into two layers, with the weighted mean value falling in between. The top layer, which sits at around 100Wm^{-1} is the high cirrus with a high cloud fraction that has the largest warming potential. The layer that emerges close to 0Wm^{-2} is due to the lower cloud fraction high clouds that emerge further from convection. These clouds may not be directly detrained from convection themselves, but still evolve as a function of TSC. With their low cloud fraction, their CRE is small, close to 0Wm^{-2} in both the LW and SW.

This sustained warming as a function of TSC is not seen in previous studies. Gehlot and Quaas (2012) found the net CRE in the ECHAM5 model to be negative up to five days (120 hours) from convection. However they did not isolate the high clouds, meaning that cooling from lower altitude thick clouds contributed to their CRE. Without removing low clouds from the analysis, the work in this chapter finds a similar sustained, albeit small, cooling for the all cloud CRE (Figure 3.10).

Our results differ from previous model studies. Gasparini et al. (2021) looked at the CRE evolution in E3SM, a high resolution cloud resolving model (CRM). These results found that, after an initial positive CRE due to small insolation values where convection occurred early before sunrise, the SW and LW CRE quickly decayed, and the net CRE became negative after 2 hours, oscillating to a small warming again at 15 hours as the solar insolation decreased. These simulations did not represent the thinnest cirrus particularly well, so may underestimate some of the LW warming seen in this chapter.

3.4 Discussion

There are multiple benefits to the TSC approach described in this chapter. It is computationally efficient when compared to tracking every single location of deep convection in the tropics. Instead of keeping and updating an array of locations for each new convective event, which grows with each timestep, this work has just one TSC array for the entire tropics, which is updated at each timestep. It also removes any bias in selecting specific initial convection, since all convection from the shortest lived to the longest lived contribute to the mean TSC. The unbounded nature of the tracking means that the full life cycle of all trajectories from convection are considered until they are superseded by new convection. Finally, detrained cirrus can be differentiated from in situ cirrus. The majority of the detrained cirrus dissipate after around 12-24 hours from convection, however some last as long as 100 hours from convection. The in situ cirrus that form along trajectories still change as a function of TSC, and the formation mechanisms responsible for the development of in situ cirrus may be affected by the deep convection that has lifted air and moisture up to the tropopause, even after the detrained cirrus has dissipated.

However, there are some uncertainties introduced in the TSC algorithm. Firstly, it only considers horizontal wind fields, averaged between 200-300hPa, and there is no vertical advection of the TSC. This is a similar assumption as made by Luo and Rossow (2004), except that they considered a larger pressure averaged wind field between 200-500hPa. The choice of the 200-300hPa average wind field is supported by the evolution of the ISCCP CTP (Figure 3.7), and the evolution of the HYSPLIT trajectory pressures. There is some vertical subsidence during the evolution of the cirrus, therefore using the 200-300hPa wind field means there is some uncertainty in the advection of the air from deep convection. Adding a vertical evolution component would be an option for future enhancement to the TSC algorithm. It would add considerable computa-

tional complexity, but would improve the calculations of TSC and reduce uncertainty introduced by using a pressure averaged wind field.

Secondly, there is a necessary interpolation that occurs when the wind field diverges. If a grid box becomes empty between timesteps, then the value for the TSC in that grid box is calculated as the mean value of the surrounding grid boxes. This increases the uncertainty in longer TSC values.

While there are significant changes in DARDAR ice properties as a function of TSC (Figure 3.8), there are still considerable uncertainties surrounding the retrieval, particularly at warmer temperatures. The DARDAR-Nice N_i retrieval compares favourably to in-situ measurements at the cirrus temperatures that are the focus of this chapter (Sourdeval et al., 2018). However, the potential temporal variation of factors such as particle shape might introduce TSC-dependent biases in the N_i retrieval, producing an apparent change in Ni.

Two key factors may introduce temporal biases in the CRE presented in Figure 3.10. First, to ensure CRE values existed for all clouds, missing LW clear sky values in the instantaneous data were filled with the 3 month/seasonal mean. This introduces some uncertainty into the results, but using annual averages makes little difference to the results. Using too short an averaging period results in large amounts of missing data near convection.

Furthermore, it is important to note that the ISCCP dataset does not necessarily provide a true representation of cloud top pressure or cloud optical depth. As stated in Chen and Del Genio (2009), the ISCCP CTP-TAU histograms are not an actual vertical distribution of clouds. This means that when considering Figure 3.6, the apparent cloud layer that appears at 370 hPa should not be taken to be a true appearance of the clouds at this height. More likely, it is the existence of thin high clouds sitting over low-

cloud that causes ISCCP to incorrectly diagnose them as lower level clouds (Mace and Wrenn, 2013). This occurs when the optically thick deep convection dissipates, and the thin cirrus moves over a region of continuous low cloud in the trade cumulus regions. The DARDAR dataset and Figure 3.8 is particularly useful here as it can provide us with a more reliable vertical distribution of the cloud amount. The issue with the ISCCP mid level clouds is not concerning, and should not impact our subsequent results, in particular the CRE calculations in Figure 3.10. To isolate our high cloud regions for the CRE calculations we select bins with very little low clouds, making it unlikely that this mid-level cloud effect drives the results in Figure 3.10.

3.5 Conclusion

The lifecycle of convective cores and their associated cirrus outflows, including their vertical evolution, have been characterised in this chapter through the creation of a 'Time Since Convection' (TSC) dataset. Convection is identified in satellite data (Figure 3.1), and then advected as a tracer in a reanalysis wind field, resulting in every point in the tropics being assigned a TSC value, indicating the last time that air parcel experienced convection (Figure 3.4). Building on previous studies that were forced to set an artifical limit to the time they tracked a parcel of air from convection (Luo and Rossow, 2004; Gehlot and Quaas, 2012), the methodology presented here allows an effectively unbounded upper limit for the time since convection. Changes in high clouds as a function of TSC continue to be observed several days after the convective event (Figure 3.9).

Cloud properties are strong functions of TSC, particularly those for high clouds. There is a general trend for high altitude, optically thinner clouds to appear over time, as expected in the evolution of deep convection to anvil to thin cirrus (Figure 3.7). Following

a sharp initial decay in both the CTP and COT in the first 12 hours from convection, a slower decrease is observed in ISCCP data over the next 120 hours. This gradual thinning of the anvil is also seen in vertical profiles of cloudiness, with the clearest changes observed in the first 120 hours (Figure 3.8a), although changes in cloud fraction as a function of TSC continue to be observed for several hundred hours after the convective event (Figure 3.8b) in both detrained and in situ cirrus.

Cloud properties and TSC are both strong functions of latitude in the tropics (Figure 3.4). However, changes in the cloud properties along TSC trajectories are not solely due to latitudinal changes along these trajectories. Controlling for latitude by looking at the zonally averaged cloud amount at a given TSC, it is clear that cloud properties are similar for a given TSC at all latitudes. This shows that looking at evolution along trajectories is not merely characterising the changing climatology as trajectories move from tropics to extra tropics, but it provides significant extra information on cloud evolution, making it a powerful tool for studying the development of clouds.

The changes in cloud properties explain the observed evolution of the CRE as a function of TSC (Figure 3.10). Considering the CRE for all clouds, the net CRE is very close to zero at all values of TSC. This apparent balance in the tropical CRE is well documented (Wielicki et al., 1996; Ramanathan et al., 1989; Hartmann and Berry, 2017), occurring both close to convection when the the LW and SW values are very high and at very large TSC. However, when the high cloud only regions are isolated, there is a sustained warming beyond 120 hours from convection after a brief initial cooling. The warming effect of high clouds is only unmasked when removing the optically thick, low clouds from the analysis, which generate a significant SW cooling at large TSC (Figure 3.7). The LW warming from these high, optically thin clouds is sustained well beyond 24 hours from convection, by which point the SW cooling from the convective core has largely dissipated. With this close CRE balance at a range of TSC values, un-

derstanding the controls on high cloud evolution as a function of TSC is essential to constrain the processes governing tropical radiation balance.

This chapter has introduced a novel method for investigating the evolution of clouds following convection, through anvil cirrus to thin cirrus. Combining satellite and reanalysis data to calculate the 'Time Since Convection' for each point in the tropics, this provides a new window into high cloud development in the tropics. The flexible nature of the TSC approach allows it to be easily applied to a wide range of cloud and atmospheric datasets, as will be shown in the next two chapters. Whilst there are significant changes in CRE with TSC observed close to convection, this chapter also demonstrates that changes in cloud properties with TSC can be observed at timescales up to 500 hours from convection, long after the original convective event has dissipated. With previous studies being limited to the youngest 30% of tropical locations (<120 hours), there is a clear need for future investigation of cirrus development at these longer timescales. The next chapter will further investigate the controls on the radiative evolution of detrained cirrus clouds, and consider the impact that the detrained cirrus lifetime has on the overall high cloud radiative effect in the tropics.

Chapter 4

Lifetime extension of detrained cirrus

Chapter Summary

- The Time Since Convection dataset is expanded to investigate how the initial location of the convection, namely if it occurred over ocean or land, impacts the subsequent radiative evolution of the high clouds.
- Land-origin trajectories are considerably warmer over the lifetime of the detrained cirrus than ocean-origin trajectories, due to the timing of the initial convection.
- Extending the lifetime of detrained cirrus is found to increase the overall high cloud radiative effect in the tropics.

The text and figures in this chapter are adapted from Horner & Gryspeerdt (2024, in review). (Horner, G. and Gryspeerdt, E.: How does the lifetime of detrained cirrus impact the high cloud radiative effect in the tropics?, https://doi.org/10.5194/egusphere-2024-1090, 2024.) The analysis and manuscript are my own work with comments and suggestions from Edward Gryspeerdt.

4.1 Introduction

The previous chapter introduced the TSC methodology and showed how cloud properties evolve as they travel away from deep convection. It also introduced the distinction between air parcels containing detrained cirrus, that is cirrus that evolve directly out of deep convection, and in situ cirrus, cirrus that form along trajectories from deep convection but do not evolve directly out of the deep convection. The amount of detrained cirrus was shown to sharply decrease at the expense of in situ cirrus air parcels as a function of TSC. This chapter will investigate the properties of the detrained and in situ cirrus air parcels in more detail, and in particular investigate how the radiative properties of these air parcels compare, and how an artificial extension to the lifetime of the detrained cirrus may impact the overall high cloud radiative effect in the tropics.

In situ cirrus, whilst not formed directly from convective cores, do not exist independently from their detrained counterparts. The lifetime and properties of detrained cirrus are affected by any factor that affects the distribution of deep convection (Gasparini et al., 2023). These large scale factors range from variable sea surface temperatures (SSTs) to the Madden-Julian Oscillation (MJO) and El-Niño Southern Oscillation (ENSO) (Riley et al., 2011). Not only will these factors affect the distribution and properties of the detrained cirrus, but the abundance of deep convection which lifts moisture into the free troposphere and generates detrained cirrus is likely to also affect the distribution of in situ cirrus (Massie et al., 2002). Conversely, the existence of in situ cirrus will also affect the impact that convective air and moisture has on the free troposphere and lower stratosphere, and therefore the development of detrained cirrus (Jensen et al., 2020). For these reasons, the total cirrus CRE in the tropics must be considered when investigating lifetime changes to detrained cirrus. Any change in the properties or amount of detrained cirrus will ultimately affect the average properties of all cirrus in the tropics.

Detrained cirrus and in situ cirrus have different radiative and microphysical properties. Of particular importance is the time dependence of the properties of detrained cirrus compared to in situ cirrus. The properties of detrained cirrus strongly depend on the time since the cirrus cloud formed out of deep convection, as shown in the previous chapter. Close to convection, the detrained anvil cirrus will be optically thick, with a SW cooling dominating the net CRE. As time since convection increases, the detrained cirrus have a tendency to thin and spread out, decreasing the SW cooling as the albedo decreases (Luo and Rossow, 2004; Hartmann et al., 2018; Gasparini et al., 2019, 2021). The albedo decreases faster than the LW emissivity, contributing to this switch from cooling to warming in the net CRE (Berry and Mace, 2014). The properties of in situ cirrus will vary, depending on the optical thickness and ice water path, as well as the altitude of the clouds (Hartmann and Berry, 2017). In contrast to in situ cirrus, where there is little time dependence on their radiative properties, the time dependence of detrained cirrus is an important factor in determining their CRE. Therefore when calculating the radiative balance in the tropics, any changes in the lifetime of detrained cirrus would have a significant impact on the delicate radiative balance in the tropics, given that their properties are such a strong function of time since convection.

In addition to the overall lifetime of the detrained cirrus, the timing of the initial convection plays an important role in determining the total cirrus cloud CRE over the detrained cirrus' lifetime. Jones et al. (2024) showed that the timing of the initial convection has a large effect on the total CRE across the detrained cirrus lifetime. This is due to the dependence of SW cooling on incoming solar radiation. If convection occurs later in the day when solar insolation is lower, the SW cooling of the younger, thicker anvil cirrus will be less than if the convection occurs in the morning or middle of the day.

The diurnal dependence on the total lifetime CRE of detrained cirrus means that the

location where the convection occurs has a large effect on the CRE across its lifetime. Many studies have investigated the diurnal cycle of regional convection (Chen and Houze Jr, 1997; Lopez-Bravo et al., 2023; Krishna et al., 2021). Fewer studies have investigated large-scale differences in the diurnal cycle of deep convection (Ruppert and Hohenegger, 2018). The difference in the diurnal cycle from terrestrial and oceanic convection, where the differences in the diurnal cycle of convection are significant, has been thoroughly studied (Albright et al., 1985; Dai et al., 1999; Dai, 2001; Zuidema, 2003). Of particular importance in this chapter is not the mechanisms that govern the behaviour of terrestrial and oceanic convection but the effect that the difference in timing of this convection has on the subsequent radiative properties of the detrained cirrus.

The temperature of anvil clouds will remain the same in a warming climate for a given increase in altitude under the fixed anvil temperature (FAT) hypothesis (Hartmann and Larson, 2002). However, many modelling studies have predicted changes in the cloud fraction of detrained anvil clouds in a warming climate (Bony et al., 2016; Cronin and Wing, 2017; Su et al., 2017). Changes in cloud area can be thought of as changes in the lifetime from a Lagrangian viewpoint assuming that the advection of the anvil cirrus remains the same, where 'time since convection' is a function of distance from a convective core (see Chapter 3).

Gasparini et al. (2021) used Lagrangian trajectories and model studies to investigate the lifetime of anvil cirrus in present and future climate. They found the lifetime of the anvil cloud to be 15 h, significantly shorter to that of Luo and Rossow (2004) who found anvil lifetimes of 30 h. These studies are sensitive to the choice of methods and thresholds for cirrus detection used. For example, Luo and Rossow (2004) determine cirrus lifetime as the point at which the cloud fraction along a trajectory first drops below 20% of the maximum cloud fraction along the trajectory (nominally 100%). There

is no robust definition of when detrained cirrus have dissipated, therefore there is some spread in the given lifetimes of detrained cirrus in the literature.

Crucially, Gasparini et al. (2021) found no difference in the lifetime of anvil cirrus in the present climate compared to a 4K warming scenario. Beydoun et al. (2021) also found a similar negligible change in anvil lifetime using RCEMIP-style models. It should be noted that neither of these studies represent all the processes that would impact cirrus lifetime, particularly the lack of diurnal cycle. More observational studies are needed to assess the impact that these particular processes may have on the lifetime of detrained cirrus clouds. Overall, there is much uncertainty in the response of high cloud area and lifetime to a warming climate.

There are many factors that impact the decay, and therefore lifetime, of detrained cirrus clouds. Gasparini et al. (2022) used idealised cloud resolving models to investigate the impact that the diurnal cycle has on the cirrus lifetime. They found that tropical anvil clouds forming in the day are more widespread and longer lasting than those formed out night, due to the shortwave radiative heating during the day which lofts and spreads the anvil clouds. During night there is an increase in ice nucleation, however this doesn't compensate for the entrainment of dry air that also acts to reduce anvil lifetime. Sokol and Hartmann (2020) also found that anvils thin more rapidly during the night due to the net radiative cooling eroding the cloud top. In both cases, it is found that the timing of convection is an important control on the lifetime of the detrained cirrus cloud.

This chapter seeks to understand the extent to which changing the lifetime of detrained cirrus impacts the overall tropical CRE. If the effect is small, then many of the drivers of anvil development mentioned above may not be important when considering changes in total cirrus CRE in a warming tropics. This question is answered by first characterising the overall high cloud CRE in the tropics as a combination of the CRE of the

detrained cirrus and in situ cirrus distributions. The distribution of detrained cirrus is then modified by artificially altering its lifetime, and the impact that this has on the overall CRE is investigated. How the CRE of detrained cirrus from land convection differs to oceanic convection is also investigated, and how their lifetime extensions change the overall tropical CRE. Answering these questions will allow us to investigate how sensitive the overall CRE in the tropics is to changes in the lifetime of the detrained cirrus clouds, enabling us to constrain future changes due to climate change or anthropogenic aerosol emissions.

4.2 Methods

4.2.1 Cirrus Type Flag: Land/Ocean origin

The TSC method developed in Chapter 3 is adapted to store properties associated with the initial convection. The convective origin flag marks each air parcel with either a land-origin or an ocean-origin flag. This flag remains on the air parcel until it is replaced by a flag from newer convection. It is important to note that this flag doesn't simply indicate whether a cirrus cloud is currently over land or ocean, but rather whether the convection it originated from occurred over land or ocean. For this reason, it is often the case that land-origin convection exists over the ocean and vice versa (Figure 4.1c). When two trajectories enter the same gridbox, the air that has more recently experienced convection (with a lower TSC) is deemed to be a more important indicator of cloud properties. As a result, the properties of the younger convection define that gridbox, whether that be the detrained or in situ flag, or the land ocean flag.

Figure 4.1 shows (a) a snapshot TSC map from 00:30UTC on the 9th April 2008, a

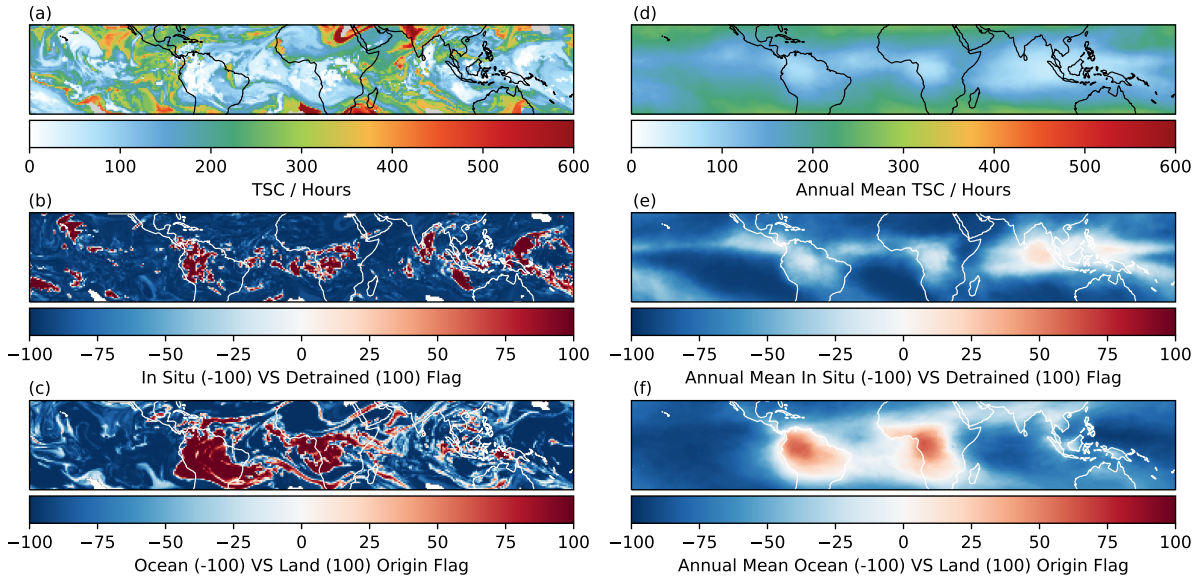


Figure 4.1: Sample TSC snapshot from April 9th 2008, 00:30UTC. (a) Time since convection (TSC) (b) In situ versus detrained cirrus flag values (c) land versus ocean convective origin flag. (d-f) 2008 annual mean for (a-c).

snapshot of the associated (b) cirrus type flag and (c) convective origin flag. As values are interpolated during the advection algorithm generating the TSC and associated flags, the flag values are not a binary classification. Instead, the positive or negative sign indicates the flag value (i.e., positive cirrus type flag indicates detrained, negative in situ), and the magnitude can be considered an indication of the confidence in that flag following the merging of trajectories over time.

4.2.2 High Cloud Radiative Effect

In this chapter, the high cloud CRE is calculated differently to Chapter 3. The reason for this is that in this chapter, the instantaneous CRE as a function of TSC is used to calculate a tropical estimate of the lifetime CRE. The method used in the previous chapter, i.e. determining the high cloud CRE in regions where the low cloud fraction was close to zero, was sufficient to show how the instantaneous CRE changed as a function of TSC. However, this approach would regionally bias the results to regions

of little low cloud if it were used to calculate a tropical lifetime CRE. This new method for calculating the high cloud CRE reduces the regional bias.

The high cloud CRE is again calculated using the CERES SYN1deg L3 1-hourly dataset (NASA/LARC/SD/ASDC, 2017). It is necessary to isolate the CRE of the cirrus clouds from the effects of low clouds in order to investigate how the radiative properties of the high clouds alone change with TSC. To isolate the radiative effect of the high clouds, the monthly mean combined low cloud and clear sky albedo (hereafter referred to as the 'background albedo') are subtracted from the instantaneous all sky albedo to give an estimated high cloud albedo. To identify the background albedo, the ISCCP histograms are used to isolate gridboxes where the high cloud fraction is less than <1%, thereby attributing the albedo to the low cloud and surface only. The monthly mean background is used in order to give sufficient coverage to co-locate regions of high cloud and background cloud. Equation 4.1 is used to isolate the albedo of the high clouds only:

$$\alpha_{high} = \alpha_{all\_sky} - \bar{\alpha}_{bkg} \tag{4.1}$$

where α_{high} is the high cloud albedo, α_{all_sky} is the all sky albedo and $\bar{\alpha}_{bkg}$ is the monthly mean background albedo. The background albedo is defined as the α_{all_sky} in regions with a <1% high cloud fraction. The SW high cloud CRE can then be calculated using:

$$SW\_CRE_{high} = F_{\downarrow} \times \alpha_{high} \tag{4.2}$$

where $F_{\downarrow}$ is the incoming solar radiation. One shortcoming in using the monthly mean background albedo, and subtracting this from the instantaneous all sky albedo, is that

this introduces regions where there is a negative albedo, and therefore an apparent positive instantaneous high cloud SW CRE. This occurs in regions where the all sky is less than the monthly mean background albedo. Figure 4.2 shows (a) an instantaneous all sky CRE, (b) the monthly mean background albedo (in this case the month of March), and (c) the instantaneous high cloud CRE calculated from these.

As seen in Figure 4.2c), in regions with little to no high cloud, the SW CRE can be positive, since the all sky instantaneous albedo is less than the annual mean background albedo. These un-physical regions disppear in the annual mean, but are required to avoid biasing the mean high cloud albedo. The LW CRE is calculated as the all-sky LW minus the clear-sky LW, due to the small LW CRE of low clouds.

4.3 Results

4.3.1 TSC distribution

Figure 4.1b shows the instantaneous detrained versus in situ flag map, and e) shows the yearly mean flag values. The detrained cirrus in red are centered around regions of active convection. These extend beyond the original convective cores, much like anvil cirrus would extend beyond the active convection, All other regions contain in situ air parcels, i.e. if cirrus were to occur in these regions they would be classed as in situ in origin.

Any region in Figure 4.1e) where the mean value is above zero are regions where detrained cirrus clouds are more often found. Compared to Figure 4.1d, these occur at low TSC values, close to convection. The likelihood of finding detrained cirrus air

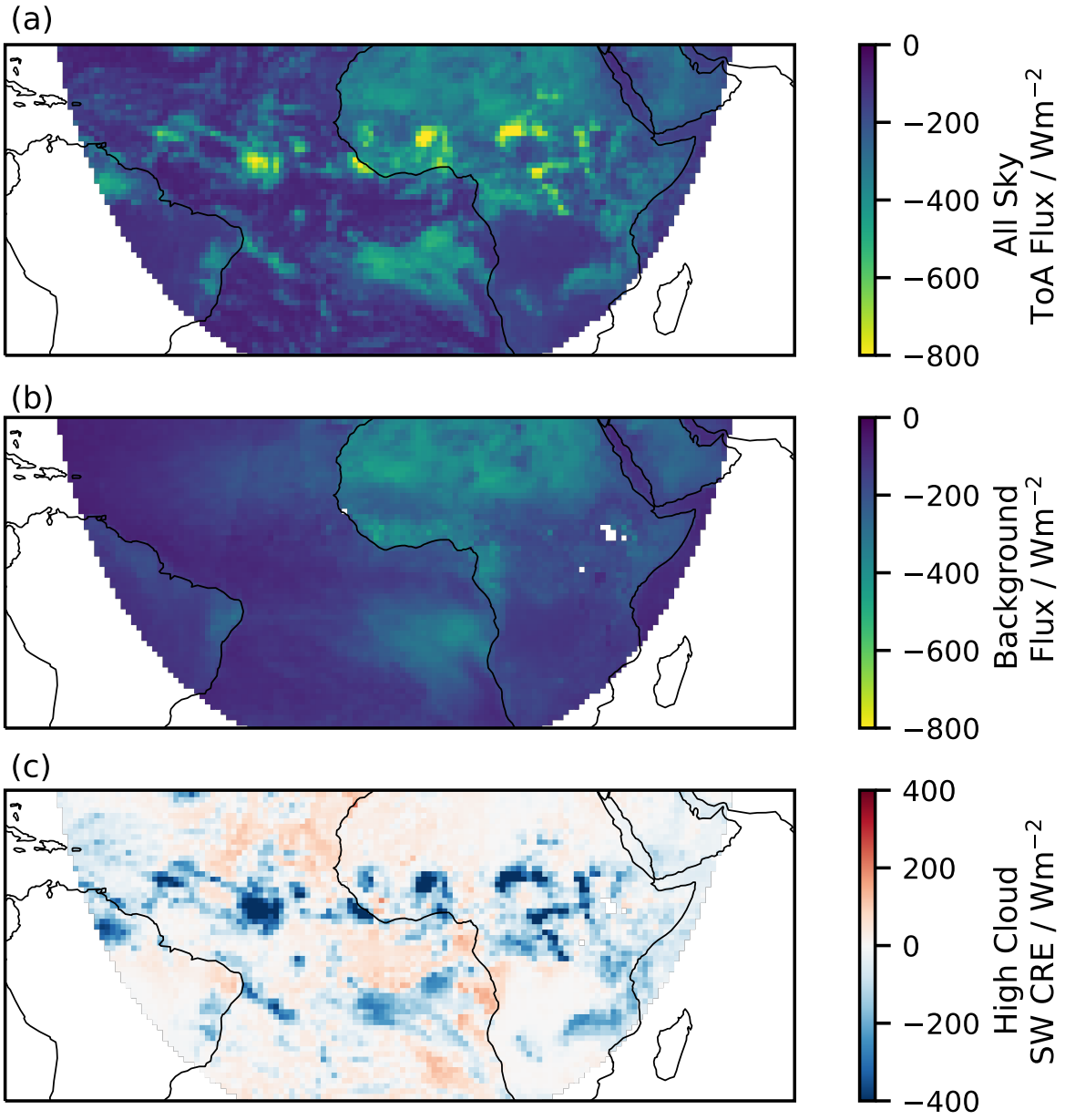


Figure 4.2: Snapshot of (a) All sky SW CRE for 12:00UTC 02/03/2008, (b) Monthly mean background SW CRE (March), (c) High cloud SW CRE for 12:00UTC 02/03/2008.

parcels is highest over the Maritime Continent. This is because there is much more sustained convection over the ocean, which means convection here has a smaller diurnal variation. This allows for a constant supply of detrained air from convection over the course of 24 hours. This compares to terrestrial regions over South America and central Africa where the convective cycle is more diurnal. This means there are large periods in the day where there is little convection, and the detrained origin air parcels are advected away and replaced by in situ air parcels from the ocean.

Figure 4.3a shows the fraction of grid boxes containing detrained or in situ air parcels, as a function of TSC. Figure 4.3b shows the total counts of both origin types. Note, the scallop-like pattern along the lines in Figure 4.3a is due to the temporal resolution of ISCCP data meaning that convection is only initiated every three hours. At low TSC values, most air parcels along trajectories contain detrained cirrus clouds. At $\approx$ 30 hours, the number of gridboxes containing detrained cirrus or in situ air parcels is approximately equal. For example, at 30 hours from convection, approximately 50% of the detrained cirrus have dissipated. At higher TSC values than this, new cirrus clouds that occurs along the trajectory are more likely to be in situ in origin.

The median lifetime, that is the TSC at the point a gridbox switches from containing a detrained cirrus air parcel to an in situ air parcel, of a detrained cirrus cloud is 36 hours. The modal lifetime is 25 hours. These values are in agreement with Luo and Rossow (2004) who found the average detrained cirrus lifetime to be 30 $\pm$ 16 hours. The standard deviation of the lifetime is found to be 30 hours. This is much larger than that found by Luo and Rossow (2004) since it doesn't track specific convective events but rather tracks all air from convection.

Figure 4.1d shows the instantaneous snapshot of the land and ocean origin air parcels. The majority of the tropics contain ocean origin air parcels (blue), as the majority of convection that occurs in the tropics occurs over the ocean. Therefore for a given de-

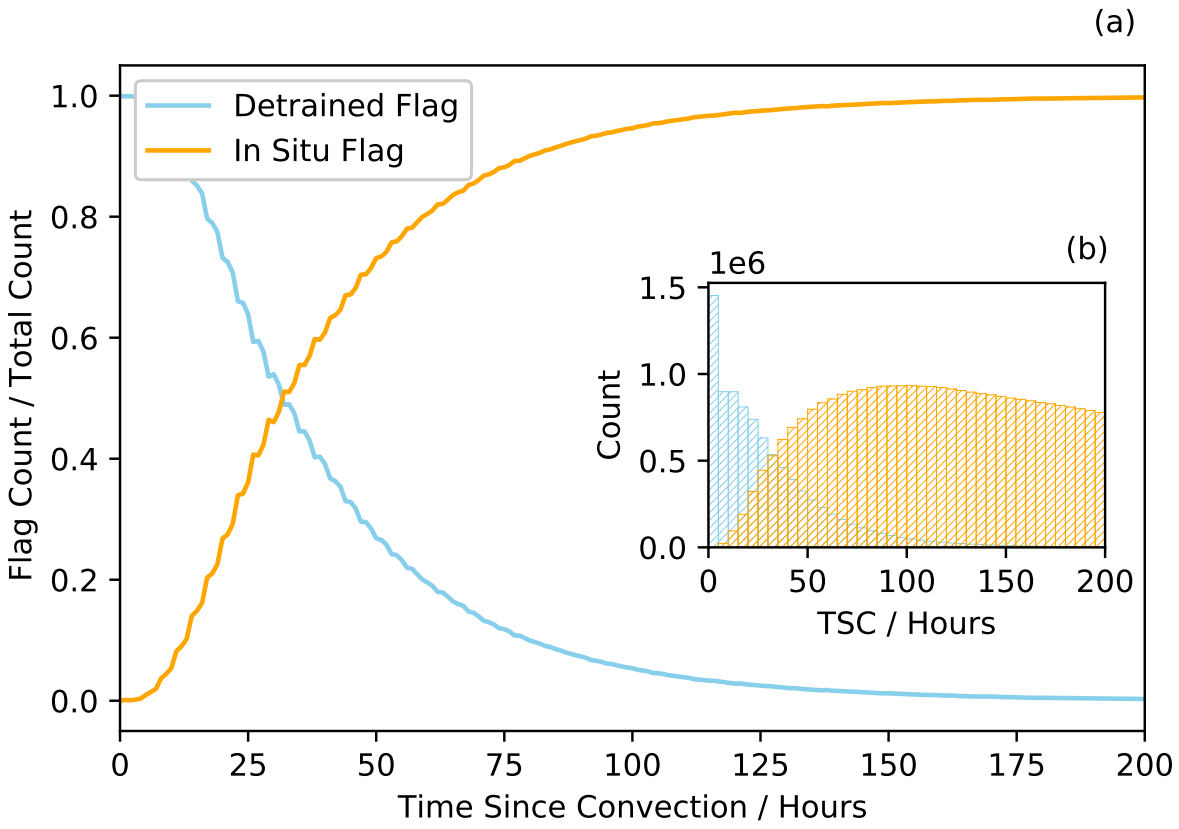


Figure 4.3: Distribution of detrained and in situ cirrus flags as a function of TSC. (a) The count of each flag as a fraction of the total TSC distribution. (b) The total distribution of each flag.

trained cirrus cloud, it is more likely to be oceanic than terrestrial in origin.

The land origin air parcels occur predominantly over land or near the coast. Figure 4.1f shows the mean land-ocean origin value. There are large regions over the southern Atlantic ocean that contain more frequent land origin air parcels than average. This is due to wind fields that carry air from land origin convection over the ocean, making it more likely to find land-origin detrained cirrus in this region compared to the rest of the global oceans.

The average air parcel origin map (Figure 4.1f) shows which type of air parcel is most common for a particular region. For example, land air parcels are most likely seen over oceans in the SE Atlantic off the coast of Africa. Figure 4.1c shows that these instances

of land origin air parcels can occur in many regions over ocean, and can travel long distances from any land source.

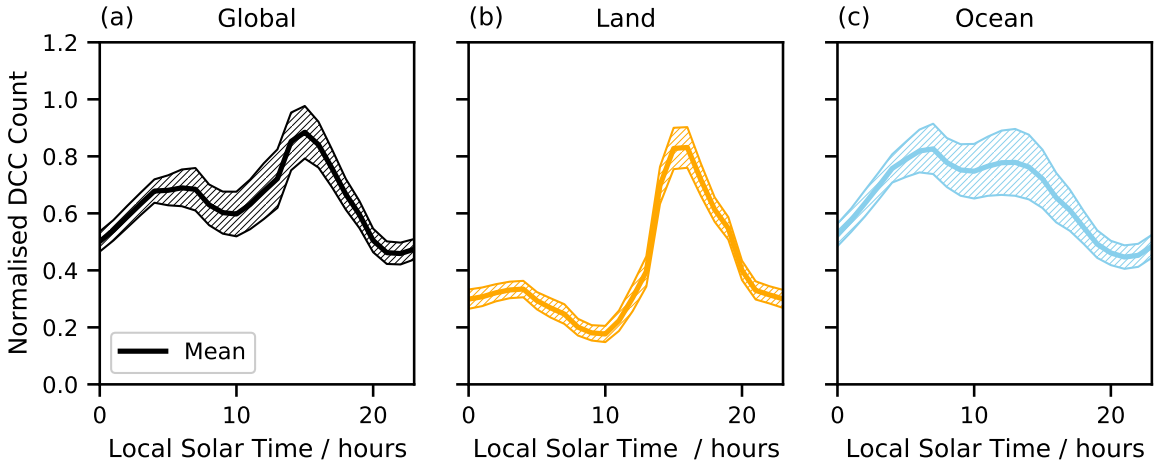


Figure 4.4: Diurnal cycle of tropical deep convection, normalised such that the maxima of each cycle is one, for (a) the entire globe, (b) land origin convection (c) ocean origin convection. The error bars correspond to the standard deviation of the interannual variability between 1984 and 2016.

Figure 4.4 shows the timing of convection from land-origin versus ocean-origin convection. There is a significant peak in convective activity over land in the late afternoon into the early evening. This is in contrast to oceanic convection which occurs comparatively uniformly throughout the day, with a smaller peak in the morning.

Figure 4.5 shows the distribution of the lifetime of the land and ocean-origin detrained cirrus. The modal lifetime for land-origin detrained cirrus is 15 hours, compared to 25 hours for ocean-origin detrained cirrus. It should be noted that many of the very low lifetimes occur when convection replaces itself between timesteps. However, these instances have a negligible impact on the median lifetime. Removing these very low lifetimes (lifetimes less than 5 hours), increases the median lifetime by less than 1 hour.

The difference in land and ocean origin detrained cirrus lifetime is significant. The land origin lifetimes are much shorter than the ocean origin lifetimes likely due to the timing of the initial convection. Given that most land convection occurs closer to the

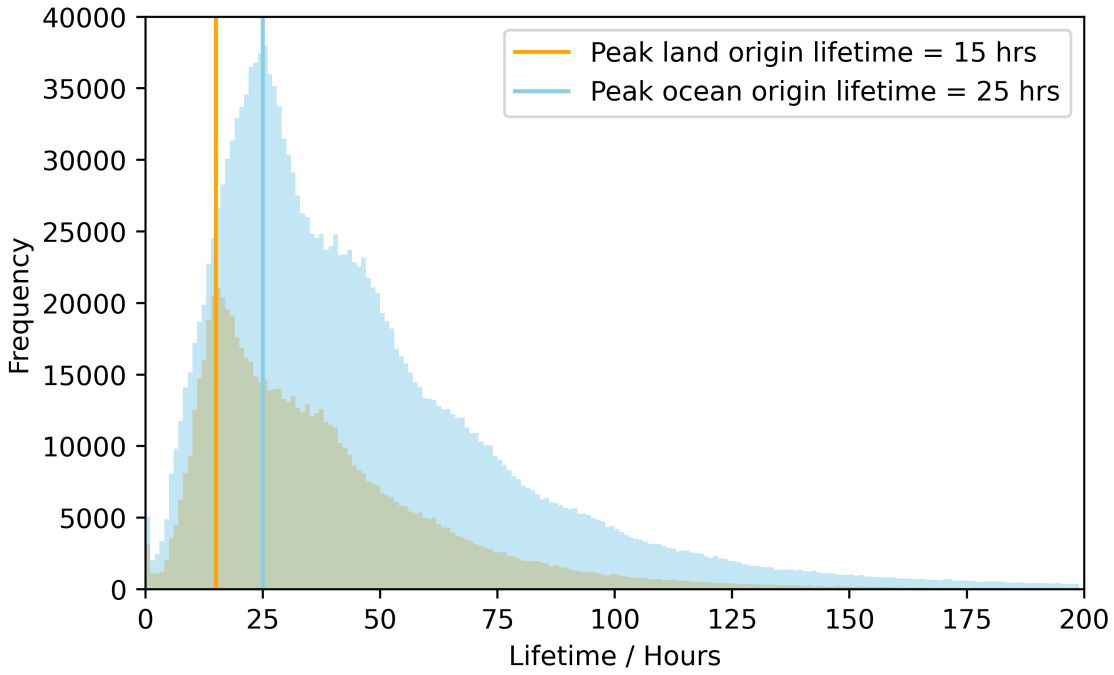


Figure 4.5: Total distribution of the lifetimes of ocean-origin and land-origin.

evening, this means that the thicker anvil exists for most of its life during solar night. This is compared to the oceanic convection that sees a small morning peak, followed by a much greater proportion occurring during the day than at night. This means that for ocean, most of the thick anvil will spend its evolution in the solar day. Detrained cirrus is likely to dissipate much faster during the night due to, among other factors, the entrainment of dry air acting to reduce anvil lifetime (Gasparini et al., 2022). These lifetime differences also support findings by Sokol and Hartmann (2020) who found that anvils thin more rapidly during the night due to the net radiative cooling which erodes the cloud top. As well as the lifetimes being different between land-origin and ocean-origin-detrained cirrus, the distribution shown in Figure 4.5 shows an oscillation in the rate of decay for both origin cirrus, which could be further evidence of a diurnal impact on the lifetime.

Figure 4.6 shows the median lifetime of detrained cirrus clouds as a function of the

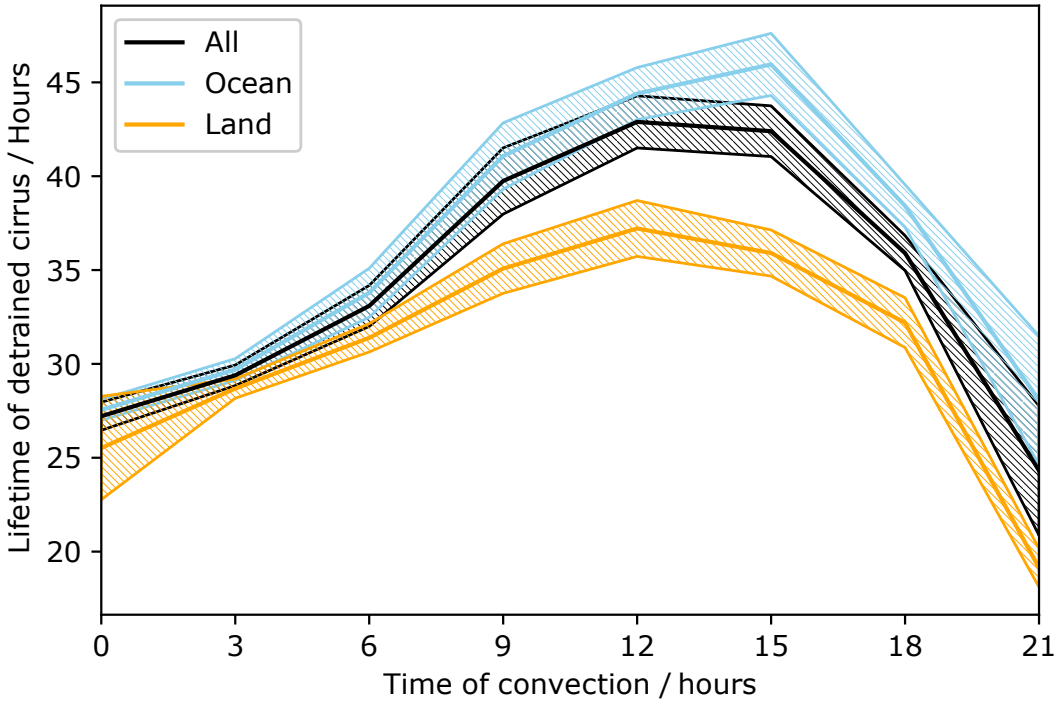


Figure 4.6: Lifetime of detrained cirrus as a function of the timing of the initial convection for all, land, and ocean origin cirrus. The error bars represent the interannual variability over the study period.

local solar time that the deep convection occurred at. This further shows a strong dependence on the lifetime of the detrained cirrus to the diurnal cycle of convection, with cirrus that originates from convection that occurs during the night having a shorter lifetime than cirrus that occurs from convection during the day. For the all origin case, cirrus that occur from convection occurring between 12pm-3pm has on average a lifetime of 45 hours. In contrast, cirrus that originate from convection occurring between 9pm and midnight have an average lifetime of around 24 hours, almost twice as short. This is the case for both land and ocean origin cirrus as well, with land origin cirrus on average having a shorter lifetime, particularly for the longest lived cirrus. This shows that the difference in the lifetimes as a function of time of initial convection isn't simply showing a shift in the distribution of convection from ocean to land throughout the day. Whilst this figure doesn't control for other factors, such as the changing strength

of convection throughout the day, it is further evidence for the hypothesis that cirrus decay quicker through the night than they do during the daytime.

4.3.2 Cloud radiative effect - detrained versus in situ

Figure 4.7 shows the LW, SW and net high cloud CRE for detrained, in situ and net of all air parcels as a function of TSC. They are weighted in each TSC bin by the relative occurence of each bin. The total net CRE is negative (a cooling) at low TSC values becoming warming after $\approx$ 6 hours, reflecting the shift from optically thick deep convective core and anvil cirrus to thinner cirrus. For the first 10 hours, the mean high CRE is the same as the detrained cirrus CRE, as almost all air parcels at this point are considered detrained (Figure 4.7).

The low occurrence of in situ air parcels at low TSC accounts for the erratic jumps in the weighted mean of the in situ CRE close to convection (Figure 4.7). As these in situ air parcels become more common, the mean high-cloud CRE approaches the in situ CRE, although some differences remain even at several days from convection. This shift in the high-cloud CRE is most evident when considering the LW and SW CRE separately. The detrained clouds have a larger SW cooling, LW warming, and stronger net positive CRE than the in situ air parcels. There is still a small trend in the CRE of the in situ air parcels even when their occurrence is low close to convection. This is likely due to shallower, mid-tropospheric convection that is not identified as deep convection, but still contributing to the CRE along trajectories.

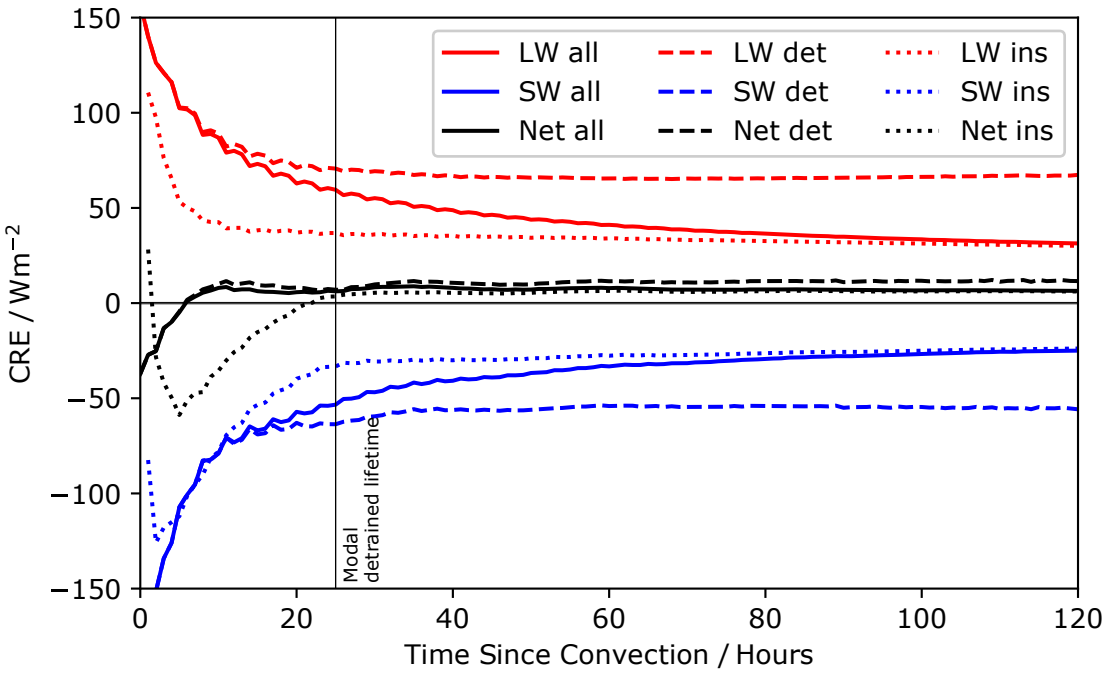


Figure 4.7: The cloud radiative effects (Net, LW, SW) as a function of the TSC for both detrained, in situ air parcels, and the weighted sum of both. The vertical line shows the modal lifetime of the detrained cirrus. Note that in situ values at TSC less than 6 hours are unreliable due to the small number of data points.

After the initial cooling, the net high cloud CRE peaks at $\approx 10\text{Wm}^{-2}$ at 10 hours since convection. There are some small oscillations in the CRE due to the diurnal cycle of convection formation (see Figure 4.4). As the proportion of in situ air parcels increases as a function of TSC, the mean net CRE decreases towards zero, as the in situ air parcels have a CRE closer to zero than the detrained cirrus clouds. At low TSC values, the change in high cloud CRE is dominated by the changing properties of the detrained cirrus clouds. As TSC increases, the change in total cirrus CRE reflects the change in distribution away from detrained cirrus clouds, towards in situ cirrus air parcels.

The total lifetime CRE of the high clouds for the entire tropics is calculated as the average CRE along trajectories, weighted according to the distribution of TSC values in the tropics and the latitude that the values occur at (see Figure 4.3b inset).

4.3.3 Cloud Radiative Effect - Land versus Ocean

There are significant differences in the CRE of air parcels that originate from convection over land, versus those that originate over the ocean. Figure 4.8 shows the LW, SW and net CRE for ocean-origin air parcels and land-origin air parcels. It is found that 20% of air parcels are land-origin, and 80% are ocean-origin. The ocean-origin evolution is very similar to the all-origin evolution since the majority of the air parcels from convection are oceanic in origin. The largest differences in the land versus ocean CRE occur at low TSC values, driven predominantly by differences in the SW cooling in the early stages of the evolution. These differences arise due to the differences in timings of convection and the strong diurnal cycle in convection over land shown earlier in the chapter. Some of the difference is also due to the contrast in surface albedo between

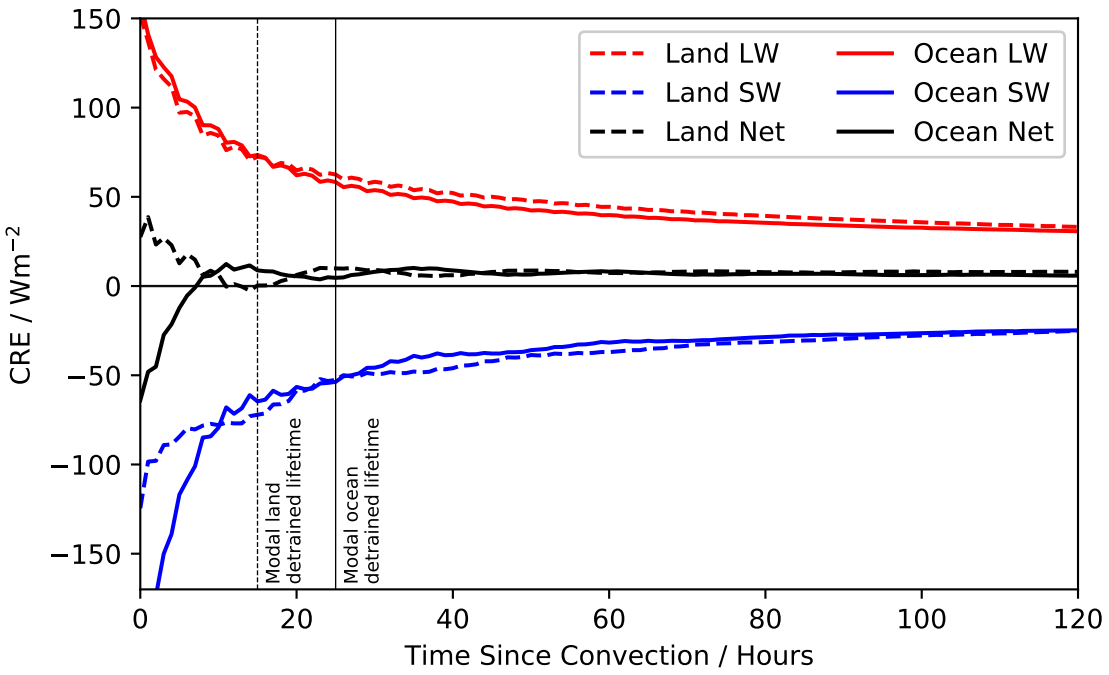


Figure 4.8: Total LW, SW and Net CRE as a function of TSC. Dotted lines show the land-origin CRE and solid lines show the ocean-origin CRE. The vertical lines show the modal lifetimes of the ocean and land detrained cirrus.

land and ocean. Further work is needed to quantify the contribution of both the albedo

contrast, and the diurnal cycle difference, by focusing on land origin convection that exists over land and over ocean.

The timing of this convection over land means that the SW cooling from the optically thick cirrus is minimised compared to oceanic convection. Therefore the total net CRE is positive in the first hours from convection. By the time the incoming solar radiation is maximised, the cirrus has already thinned sufficiently that the SW cooling is significantly smaller than the LW warming. As a result, the land-origin air parcels have a positive CRE throughout their entire lifecycle. The timing of terrestrial convection is shown to play a vital role in determining the total CRE of the detrained air parcels (Jones et al., 2024).

The differences in the LW warming between land and ocean-origin air parcels are less clear. In the early stages of the convection, they are similar. After 20 hours, the land-origin air parcels appears to have a slightly larger LW warming than the ocean-origin air parcels. This could be due to stronger convection occurring over land, leading to higher altitude cirrus producing a larger LW warming (Takahashi et al., 2017). The land-origin parcels also have a stronger SW cooling after the initial stage of convection, suggesting that the detrained cirrus from land-origin convection are optically thicker than their ocean-origin counterparts.

Over the entire range of lifetimes, the weighted average of the land-origin CRE is 7.7 $\pm$ 0.6 Wm^{-2}, the ocean-origin has a total CRE of 4.3 $\pm$ 0.4 Wm^{-2}. This difference in the lifetime CRE is almost entirely due to the differences in the timing of the initial convection, and as such the lack of SW cooling that occurs in land-origin cirrus compared to ocean-origin cirrus.

4.3.4 Lifetime adjustments

Given that the CRE of detrained cirrus clouds is very different to the CRE of in situ cirrus air parcels (Figure 4.7), the lifetime of the detrained cirrus clouds is very important when determining the total tropical CRE. As mentioned above, the median lifetime of the detrained cirrus is approximately 36 hours, with a modal lifetime of 25 hours. This is shown separately for land and ocean origin cirrus in Figure 4.5. This is defined as the mean TSC when the air parcel changes from detrained to in situ.

The impact of extensions to detrained cirrus lifetime on the tropical CRE can be estimated through an artificial modification of the detrained cirrus distribution. The lifetime of the detrained cirrus can be artificially extended by modifying the fractional distribution of the detrained cirrus in Figure 4.3, a novel method introduced in this thesis. In this chapter, a simple approach to extend the distribution of the detrained cirrus is used. The original distribution is stretched along the TSC-axis by a given percentage, and this new distribution can be thought to represent the distribution of detrained cirrus in this new extended lifetime regime. This is shown in Figure 4.9. By stretching the distribution along the x-axis by some factor the amount of detrained cirrus is artificially increased for a given TSC. It is important to note that the TSC distribution is not changed when the lifetime of detrained cirrus is extended, just the radiative properties of the cirrus as a function of TSC. This decouples the cloud evolution from the convective occurrence and large scale flow. This change, therefore, maintains the overall shape in the distribution of TSC whilst increasing the proportion of detrained cirrus air parcels for a given TSC. This increases the mean detrained cirrus lifetime by the prescribed factor.

Increasing the distribution is analogous to increasing the mean lifetime of each detrained cirrus by the same percentage. Figure 4.9 shows that for a 50% increase in

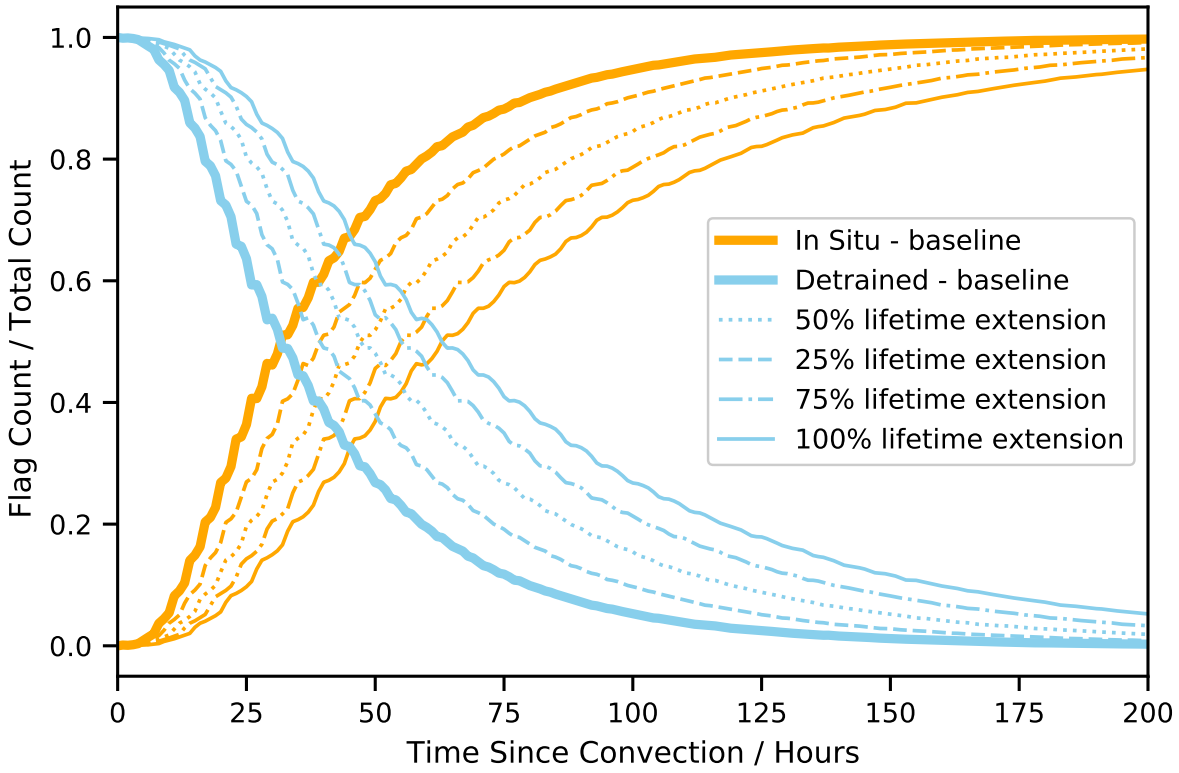


Figure 4.9: The fractional distribution of the detrained versus in situ air parcels. Dotted lines represent various distributions when the detrained cirrus are extended by a percentage.

the detrained cirrus lifetime, this shifts the point at which the number of in situ and detrained parcels are equal from around 30 hours to just under 50 hours.

As the all-cirrus LW, SW and net CRE along trajectories from convection are a weighted average of the CRE contributions of detrained cirrus and in situ air parcels, changing the lifetime of the detrained cirrus changes the weighting and thus total CRE along the trajectories. With detrained cirrus having a stronger warming effect, extending their lifetime increases the overall warming of tropical cirrus clouds.

Figure 4.10 shows how the total tropical CRE changes when the lifetime of the detrained cirrus is increased. In all cases, the tropical CRE increases almost linearly for a given increase in the lifetime of the detrained cirrus. For a doubling in the lifetime of all-origin detrained cirrus, the tropical CRE increases from a baseline of 5.0 $\pm$ 0.4

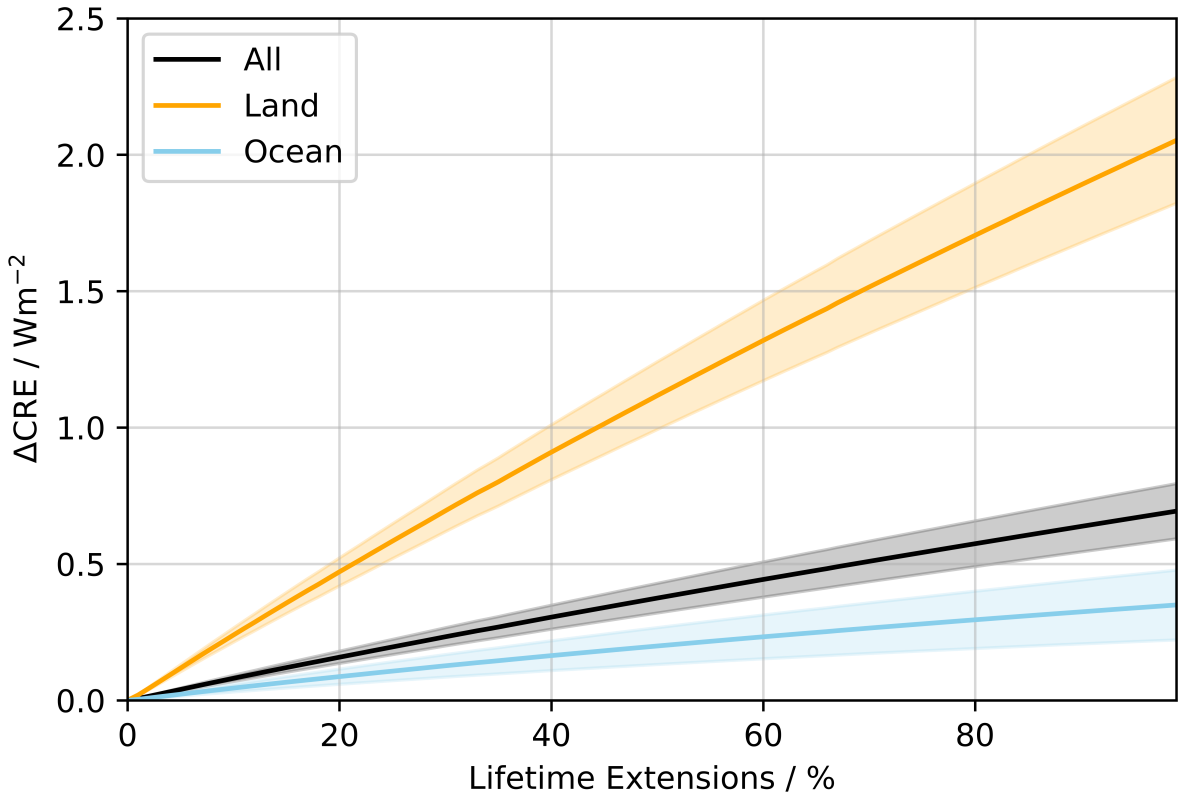


Figure 4.10: Change in CRE for all, land and ocean origin air parcels for a given percentage increase in the lifetime of the detrained cirrus clouds.

375 Wm^{-2} to $5.7 \pm 0.5\ \mathrm{Wm}^{-2}$. The uncertainties given represent the interannual variability in the increase in CRE for a given increase in detrained cirrus lifetime. In practice these uncertainties are likely larger due to the inherent uncertainties in the initial calculation of CRE, however these are normalised to a baseline, therefore there is no uncertainty in the lifetime extension when the lifetime extension is zero hours.

380 The increase in the high cloud CRE is similar for an increase in the lifetime of ocean-origin detrained cirrus. This is to be expected given the greater proportion of convection originating over ocean versus land. A doubling in the ocean-origin detrained lifetime leads to an increase in the tropical CRE of $0.3 \pm 0.1\mathrm{Wm}^{-2}$, from a baseline CRE of $4.4 \pm 0.4\ \mathrm{Wm}^{-2}$, to $4.7 \pm 0.4\ \mathrm{Wm}^{-2}$.

385 Interestingly the increase is not linear over time, with the first 50% lifetime extension

increasing the all-origin CRE by 0.06Wm^{-2} more than the final 50% increase. One reason for this is the decreasing difference between the in situ CRE and detrained CRE at longer TSC values. Therefore any adjustment to the relative distributions at longer TSC will have a slightly smaller impact than initial adjustments to the shorter lifetimes.

For land-origin cirrus the increase in tropical CRE is much greater for a given increase in the detrained cirrus lifetime. A doubling the land-origin detrained cirrus lifetime increases the tropical CRE from a baseline of 7.7 ± 0.6 Wm $^{-2}$ to 9.7 ± 0.5 Wm $^{-2}$. This is because land-origin detrained cirrus are much more warming than ocean-origin cirrus, particularly at low TSC values (Figure 4.8). This is due in part to a smaller SW cooling in land-origin detrained cirrus because of differences in the timing of convection. This means that increasing the proportion of detrained cirrus for a given TSC, increases the overall CRE by a larger amount than the same increase for ocean-origin detrained cirrus.

Figure 4.11 shows the LW, SW and net CRE as a function of TSC, for a baseline, as well as a 50% and a 100% increase in the lifetime of detrained cirrus. This shows an increase in the net CRE at all TSC values given an increase in the lifetime of detrained cirrus. At very low TSC values there is little change in the net CRE for an increase in lifetime. At these low TSC values, detrained air parcels account for almost all the air parcels. Therefore, there is no change in the relative distributions of detrained versus in situ air parcels (see Figure 4.3) and no change in the overall CRE at low TSC values.

4.4 Discussion

In this work, the overall high cloud CRE, including both detrained origin cirrus and in situ origin air parcels (which may contain in situ cirrus) was found to be 5.0 ± 0.4

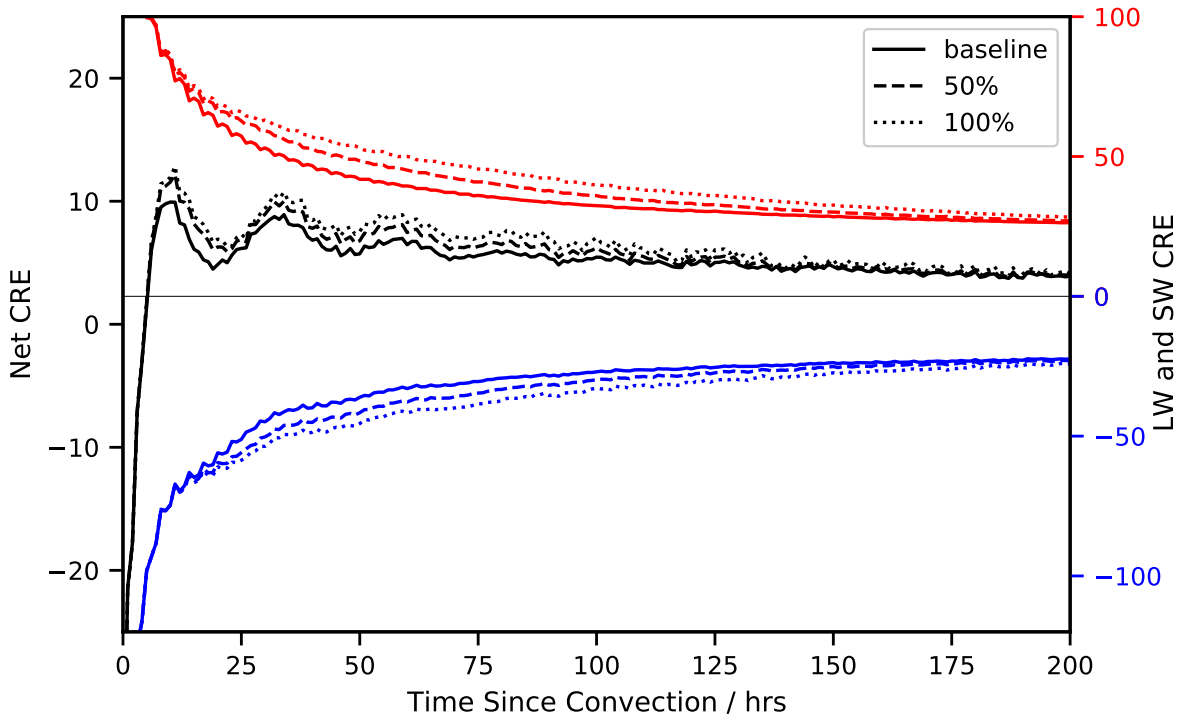


Figure 4.11: Total net (left axis) and LW and SW (right axis) CRE as a function of TSC.The dashed and dotted lines represent a 50% and 100% increase in the lifetime of detrained cirrus respectively. Note the separate axis for Net, LW and SW radiatve effects, introduced here to show the changes in CRE for each lifetime extension more clearly.

Wm^{-2}. However, there are still a number of uncertainties that need addressing. These uncertainties fall into three main categories: a) isolating the radiative effects from high clouds, b) the distinction between detrained and in situ air parcels, and c) the method for extending the lifetime.

In order to isolate the radiative effects of high and low clouds, this chapter attempts to consider the contributing radiative effect of the low clouds by calculating the monthly mean 'background albedo', which is then subtracted from the instantaneous all-sky albedo to give the 'high cloud' albedo. The background albedo is the all-sky albedo in regions with no high cloud. This method gives an approximate high cloud SW CRE. However, it relies on the assumption that the monthly mean background albedo is approximately representative of the instantaneous background albedo, if it were possible

to be calculated for everywhere in the tropics at each timestep.

As the annual mean background albedo is subtracted from the instantaneous all-sky, there are occasions where the annual background is greater than the all-sky (Figure 4.2). This produces a negative high cloud albedo and thus a positive SW cooling value. It can be assumed in these regions this occurs when the all-sky is close to the clear-sky albedo value, with total cloud fraction being lower than the average low cloud fraction. This assumes that there is little correlation between the low and high cloud fraction. For a further discussion of cloud overlap statistics, see Tompkins and Giuseppe (2015). The impact of these cases averages to zero when calculating the annual mean SW high cloud CRE, and is less important for this work's analysis as they occur at large TSC values in regions where there is little high cloud. This situation occurs in regions where the average low cloud cover is high, and therefore the average background albedo is high. Therefore, if a trajectory is observed at this location that contains an optically thin high cloud, and little to no low cloud, the observed albedo will be lower than the average albedo, thus resulting in a 'negative' high cloud SW CRE. It is also known that the ISCCP cloud type histograms may over attribute the TOA cooling to low clouds (Stephens et al., 2018). This may lead to a positive (warming) bias in the results in this work, therefore it should be understood that these results represent an upper bound. However this bias is likely small in comparison to other uncertainties mentioned above.

The second area of uncertainty in this work surrounds the definition of detrained cirrus. This work defines the end of a detrained cirrus lifetime, and the beginning of the in situ air parcels, as the point at which a cloud along a trajectory from deep convection moves below 10% cirrus cloud fraction for the first time. Any cirrus that then appears along a trajectory after this point is defined as in situ in origin. This is similar to Luo and Rossow (2004) who define the end of their cirrus lifetime as the point at which the

cirrus cloud reaches 1/5 of the maximum cloud fraction along the trajectory. Changing the definition of detrained cirrus would not change the overall high cloud CRE. However, it does change the calculated lifetime of detrained cirrus, which is shown in Figure A.1 in the appendix. There is no universal definition for 'detrained' or 'anvil' cirrus, and as such the lifetimes of these clouds vary depending on how they are defined. Nevertheless, the lifetimes in this work fall within the expected ranges given in the literature (Luo and Rossow, 2004) and as shown in Figure A.2, the final values for the change in CRE for a given lifetime extension are not particularly sensitive to the threshold used to define the convection.

The method used to extend the lifetime of the detrained cirrus is relatively idealised, insofar as it models a lifetime extension as a change in the distribution of detrained cirrus at the expense of in situ cirrus. Moreover, the extension in the distribution modifies the distribution mostly at the tail end of the detrained cirrus lifetimes, meaning that the oldest detrained cirrus are the ones that see the largest increase. The purpose of this work was not to assess the methods through which a lifetime extension would occur. Instead, the aim was to provide a bound on the impact that increasing the lifetime of the detrained cirrus would have on the tropical high cloud CRE. By modifying the distribution to represent an increase in lifetime, particularly in a way that may impact the longer lived detrained cirrus more than the short lived cirrus, we do provide such an upper bound, since any modification to the shorter lived cirrus would not increase the CRE by as much, as they are already more cooling. In reality, any physical routes through which a lifetime extension will likely increase the total CRE by less than the values we provide here. Further work is needed to assess the mechanisms through which lifetime extensions might occur, and what the range of impacts this may have on the CRE. For example, the lifetime could change due to a stronger clustering of convective cores (Jones et al., 2024) or increased updrafts via aerosol invigoration (Abbott and Cronin, 2021). Each of these mechanisms may impact the lifetime in a distinct way

from the idealised set up in this work. Investigating these mechanisms and the specific impacts they had on the lifetime would make for an interesting comparison study to the idealised extension proposed in this chapter, and would be a necessary addition to put these results into context, as well as developing a stronger constraint on the potential changes of the CRE.

As well as showing the difference in detrained cirrus CRE due to the origin of the convection, this work shows how extending the lifetime of the detrained cirrus changes the overall lifetime CRE. In this work, the lifetime is a simple distribution, and extending the lifetime is merely a case of extending the distribution at the expense of in situ air parcels. This assumes that every cirrus cloud in the tropics is either detrained or in situ and these are distinct from each other, i.e. an increase in detrained air parcel amount should correlate with a decrease in in situ air parcel amount. The purpose of extending the lifetime isn't to obtain a concrete value of the CRE for a given lifetime extension, but instead to indicate the trend in CRE for an increase in lifetime. This helps to bound estimates of how much the lifetime of a detrained cirrus would need to change to significantly affect the tropical high cloud CRE.

This work finds that increasing the lifetime of the detrained cirrus increases the overall high cloud CRE in the tropics, resulting in an overall warming. This is because on average the detrained cirrus have a larger net CRE than the in situ air parcels. For a 50% increase in the lifetime, the average CRE of tropical cirrus increases by $0.3 \pm 0.1 \mathrm{Wm}^{-2}$. Comparing this to aerosol invigoration studies which have shown lifetime extensions of detrained cirrus on the order of 30% (Zang et al., 2023), it may be the case that aerosol invigoration may not have a large impact on the total tropical CRE, however more work is needed to constrain the lifetime extension from aerosol invigoration, which is currently highly uncertain.

The average lifetime of detrained cirrus clouds is found to be approximately 36 hours,

similar to that found by Luo and Rossow (2004). This implies that increasing the average lifetime of detrained cirrus clouds by 15 hours would increase the overall high cloud CRE by 0.4 ± 0.1 Wm^{-2}. This increase is larger for land-origin convection, which increases by 1.1 ± 0.1 Wm^{-2} for a 15 hour increase in lifetime, and smaller for ocean-origin convection which increases by 0.2 ± 0.1 Wm^{-2}.

4.5 Conclusion

The lifetime of detrained cirrus clouds from convection plays an important role in determining the overall detrained CRE in the tropics, and this may impact the total high cloud CRE in the tropics. Small changes in the evolution of these clouds, either driven by their initial conditions or meteorological environment, have been hypothesised to produce large responses in the high cloud CRE, making understanding this evolution essential to constrain both climate forcings and feedbacks. Tracking the evolution of cirrus clouds throughout the tropics as they move away from convective events and isolating the high cloud CRE from the background albedo variation caused by low clouds, this work characterises the lifecycle of the cirrus CRE using satellite observations. Defining the lifetime of detrained cirrus based on the point along a trajectory following convection where the high cloud fraction drops below 10% (representing the time when the detrained cirrus has dissipated), the impact of cirrus formation mechanisms on CRE is isolated. By tracking the properties of the initial convection, this method also allows the impact of the initial convection on the CRE to be investigated. The tracking approach used in this work differs from previous studies, such as Jones et al. (2024), by using ISCCP data with a much longer time record, as well as covering the entirety of the tropics, without explicitly tracking individual clouds at all. This allows for regional variations such as the land ocean contrast to be thoroughly investigated.

Most detrained air parcels remain in the central tropical belt, close to active convection, while in situ air parcels exist throughout the tropics (Figures 4.1b,e). The high cloud CRE of the detrained cirrus air parcels is found to be considerably more warming than the CRE of in situ air parcels (Figure 4.7). The high cloud radiative effect is calculated by subtracting the variability in the background albedo due to changes in low clouds from the overall CRE (Figure 4.2). Calculating the total high cloud CRE as the weighted mean CRE along trajectories from deep convection gives a total high cloud topical CRE as 5.0 ± 0.4 Wm^{-2}.

Air parcels along trajectories from oceanic convection are compared to those from detrained convection (Figures 4.1c,f). Air from land convection exists over large regions of the oceans, and air from oceanic convection often exists over land. The high cloud CRE along trajectories from land-origin convection is 7.7 ± 0.6 Wm^{-2}, compared to 4.4 ± 0.4 Wm^{-2} for cirrus along trajectories from ocean-origin convection. Strong differences in the timing of the initial convection over land and ocean (Figure 4.4) lead to these differences in the net CRE of detrained cirrus clouds as a function of TSC. Detrained cirrus clouds from land are found to have a net warming across their entire lifetime, as land convection occurs much later in the day than oceanic convection (Figure 4.4). This reduces the SW cooling from the thick anvils at low TSC values compared to oceanic convection, which detrained from convection much earlier in the day when the SW cooling is still significant. This is similar to the results of Jones et al. (2024), who showed the importance of the diurnal cycle in determining the lifetime CRE of detrained cirrus clouds.

The lifetime of detrained cirrus is also shown to be a strong function of the timing and location of the initial convection. Figure 4.5 shows the distribution of the lifetimes for ocean-origin and land-origin detrained cirrus, showing that on average, ocean origin detrained cirrus persist for longer than their land-origin counterparts. It is hypothe-

sised that much of this is due to the difference in the diurnal cycle of land and ocean convection, with land-origin cirrus occurring later in the night, leading to faster decaying cirrus (Gasparini et al., 2022; Sokol and Hartmann, 2020). Figure 4.6 supports this theory, showing that detrained cirrus originating from convection occurring later in the day have, on average, shorter lifetimes than convection that occurs earlier in the day. More work needs to be done to investigate this further, and control for other confounding factors that may impact detrained lifetime such as the initial strength of the convection.

The lifetime of detrained cirrus clouds is artificially increased by stretching the distribution of the detrained cirrus air parcels at the expense of the in situ air parcels (Figure 4.9). These extended distributions are then used as the weights when calculating the total cirrus CRE in the tropics. It is found that increasing the lifetime of the detrained cirrus clouds increases the total CRE in the tropics almost linearly. For example, a 50% increase in the detrained cirrus lifetime, from an average of 36 hours to 54 hours, increases the total tropical CRE from 4.4 ± 0.4 Wm^{-2} to 4.8 ± 0.4 Wm^{-2} (Figure 4.10).

The impacts of lifetime extension of detrained cirrus air parcels is calculated for both land-origin and ocean-origin cirrus. Increasing the land-origin detrained cirrus lifetime by 50% increases the total land-origin CRE in the tropics by 1.1 ± 0.1 Wm^{-2}. On the other hand, increasing the ocean-origin detrained cirrus lifetime by 50% increases the total ocean-origin CRE in the tropics by only 0.2 ± 0.1 Wm^{-2}. These contrasts arise because of the differences in the CRE of land-origin and ocean-origin detrained cirrus in the early stages of their development. Ocean-origin detrained cirrus have a negative (cooling) CRE at low TSC, therefore any increase in the lifetime of the detrained cirrus also increases the time spent cooling, thus dampening the warming impact they may also have at longer TSC. Land-origin detrained cirrus are warming at all stages of their development, therefore any increase in their lifetime will amplify their warming

impact (see Figure 4.8).

While this chapter shows the potential for cirrus lifetime changes to modify high cloud CRE in the tropics, further work is required to constrain these changes in detrained cirrus lifetime. Building on this estimate of how the radiative effect of these clouds responds to lifetime extensions, the impact of meteorological or anthropogenic drivers (such as aerosol invigoration) on the lifetime of anvil cirrus, and therefore the overall tropical cirrus CRE must be bounded to fully constrain the magnitude of this effect. In the final chapter, the impact that the initial strength of convection has on the radiative properties of the detrained cirrus is investigated.

Chapter 5

Sensitivity of the detrained cirrus CRE to AOD at convection

Chapter Summary

- It is found that stronger convection leads to warmer detrained cirrus. This is true for both land and ocean, however the relationship is much stronger over land.
- This relationship is due, once again, to the timing of convection playing an important role in determining the lifetime CRE. Stronger convection occurs at times, more often during the night, more conducive to warming over the entire detrained cirrus lifetime.
- Finally, the sensitivity of the cloud radiative effect (CRE) to cloud top pressure (CTP) is linked to the AOD-CTP relationship to bound an estimate for the impact of AOD on the detrained cirrus CRE, using a novel non-local approach.

The figures and text in this chapter are my own work with comments and suggestions from Edward Gryspeerdt.

5.1 Introduction

The impact of aerosols on convective strength has been investigated in various observational studies, often through attempts to observe aerosol invigoration (Andreae et al., 2004; Koren et al., 2005; Storer et al., 2014). Many studies have found observational evidence of a relationship between cloud top pressure (CTP) (a suitable and commonly used proxy for convective strength (Adler and Negri, 1988)), and AOD (Storer et al., 2014; Zhang et al., 2022). However, as highlighted by Varble et al. (2023) there is often great uncertainty in attributing changes in the cloud properties to the aerosols themselves. This is mostly due to difficulties in observing both AOD and proxies for convective strength in the same gridbox or at the same time (Stier, 2016). There are also difficulties in controlling for meteorological factors that may influence any observed AOD-CTP relationship.

Most recently, Herbert and Stier (2023) investigated the impact that smoke from Amazonian wildfires had on cloud properties and the instantaneous radiative impact on the top of atmosphere radiative cooling. They found a decrease of up to -50Wm^{-2} for an AOD perturbation of +1 and also found that aerosol changed the onset time of deep convection, by depressing afternoon convection. In a recent modelling study, Herbert et al. (2021) observed considerable diurnal variability in the cloud response. They also reported an increase in the IWP across the study domain that generated a positive radiative forcing due to the aerosol. Yu et al. (2007) examined cloud-smoke relationships in the Amazon using MODIS retrievals over the 2002 and 2003 dry seasons and found considerable interannual variability in the cloud response. These works highlight the importance of having longer-term studies to dampen the impact that any single year has on the findings, and accounting for the diurnal cycle of convection in investigating AOD-CTP sensitivity.

Although many studies have attempted to quantify the relationship between AOD-CTP, few studies have investigated how the convective strength (CTP) impacts the evolution of the detrained cirrus that flow out of the deep convection (Koren et al., 2010b). Answering this question would help constrain any impact that aerosol invigoration could have on the overall tropical CRE, and assess the importance that any potential invigoration would have on the overall radiative forcing of deep convection and anvil cirrus.

It is hypothesised that stronger convection leads to cirrus outflowing at higher altitudes, exposed to greater wind shear, which ultimately leads to outflowing cirrus that have a large warming than in the non-invigorated cloud (Lindsey and Fromm, 2008; Koren et al., 2010b). These works indicate that there may be a warming that occurs due to stronger convection. However, more work needs to be done to investigate how the evolution of the detrained cirrus is impacted by the initial convective strength and how this is related to the diurnal cycle of tropical convection. For this, large scale temporal studies are required.

It is known that convection of differing strengths exhibit very different diurnal cycles (Chen and Houze Jr, 1997). What is less clear is how this change in strength impacts the CRE of the detrained cirrus. Gasparini et al. (2022) showed in an idealised simulation that the diurnal cycle of oceanic convection has a significant impact on the lifetime CRE, with convection that occurs during the night being more warming over the simulation period than daytime convection. Jones et al. (2024) also showed in a regional study over Africa that the timing of convection has a large impact on the overall anvil CRE. However neither of these studies linked the impact of the convective strength, via the diurnal cycle, to the lifetime CRE of the detrained cirrus.

There are clear unanswered questions regarding how a) aerosols impact the strength and timing of the convection, and b) how sensitive the lifetime CRE of detrained cirrus

are to changes in the timing and strength of the initial convection. By calculating both a sensitivity of CRE to high cloud CTP, and also calculating as sensitivity of high cloud CTP to AOD, an estimate of the impact that AOD has on the detrained cirrus CRE can be calculated. This chapter introduces a novel way to attribute local changes in the high cloud CTP to non-local changes to the detrained cirrus CRE, thereby linking both sensitivities. This chapter aims to introduce a bound for the change in the detrained cirrus CRE based on a change in the AOD from pre-industrial to present day, taken from Bellouin et al. (2020).

5.2 Methods

The sensitivity of the detrained cirrus CRE to the initial CTP ($\frac{dCRE}{dCTP}$) of the deep convection can be linked to the sensitivity of high cloud CTP to the AOD ($\frac{dlnCTP}{dlnAOD}$), in a similar way to Christensen et al. (2016). This can be used to estimate the change in the detrained cirrus CRE for a given change in AOD from pre-industrial to present day, by using the following equation:

$$\Delta CRE = \left(\frac{dCRE}{dCTP} \times CTP \frac{dlnCTP}{dlnAOD} \right) \times \Delta lnAOD \tag{5.1}$$

However, this equation assumes that the change in the CRE of the detrained cirrus occurs at the same location as the change in the aerosols. Instead, the change in the CRE of the detrained cirrus occurs at some non-local distance away from the convection, in 'detrained' space, and needs to be linked to a local change in the AOD in 'convective' space, which occurs at the location of convection. Therefore, there is a need to introduce a mapping factor (f_{det}) that enables the non-local sensitivity of the detrained

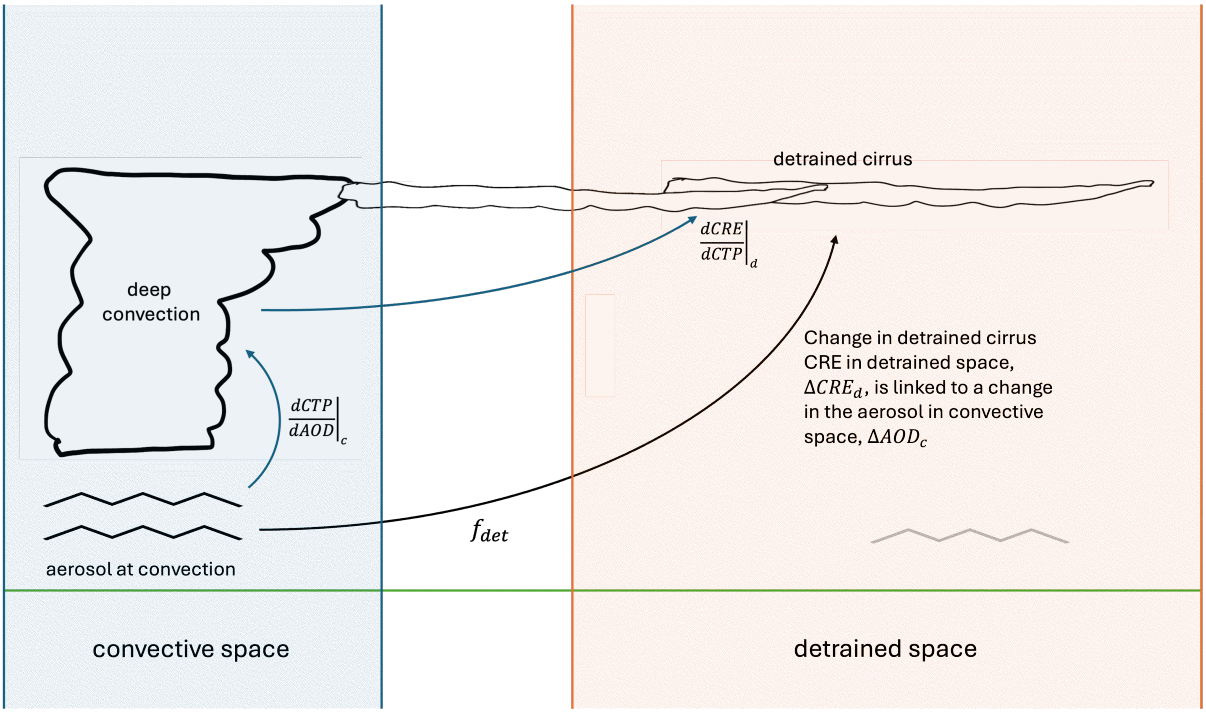


Figure 5.1: Schematic showing how the AOD-CTP sensitivity, which exists in convective space c, can be linked to the CRE-CTP in detrained space d.

cirrus to the deep convection to be combined with a local sensitivity of the deep convection to the AOD. Figure 5.1 shows a schematic of the two sensitivities occurring at separate locations, linked via the f_{det} term. Note how the change in aerosol occurs at the location of convection in convective space (denoted with a subscript c), which in turn generates the sensitivity AOD-CTP in convective space. By contrast, the sensitivity of CRE-CTP occurs in the detrained space, denoted by subscript d. It is clear from this diagram that the AOD at the location of the detrained cirrus is not suitable for use in the CRE-AOD sensitivity calculation, as it will have no impact on the deep convection itself.

Figure 5.2 shows how the f_{det} term is calculated. For convection occurring at some given location in the tropics, the probability map of detrained cirrus occurring from this convection is given. This f_{det} term is therefore defined as the probability of finding detrained cirrus at some location in detrained space d, given convection occurring at location c in convective space ($P(det|conv)_{cd}$). This, in turn, is calculated as the number

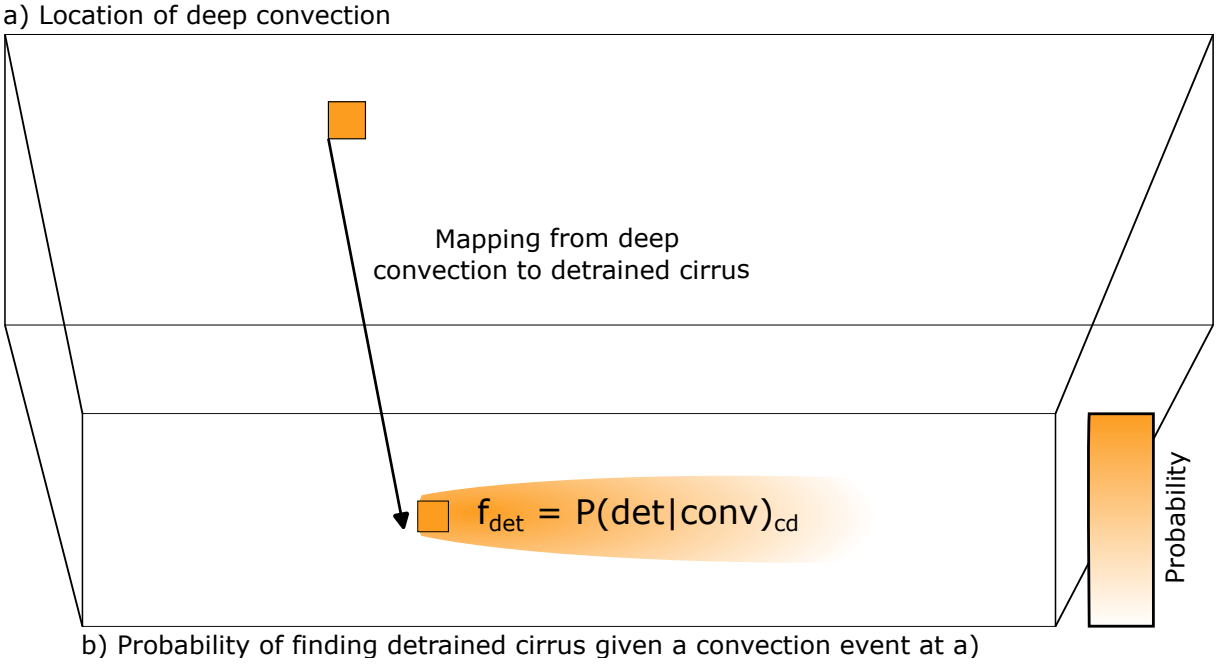


Figure 5.2: Schematic showing a) convection occurring at some location, and b) the associated probability of finding convection, given that some convection occurred at a).

of detrained air parcels at any location that have originated from convection at a given location, divided by the number of convective events $\left(\frac{N(det)_d}{N(conv)_c}\right)$ at a given location in the tropics, where the subscripts c and d denote the convective space and detrained space. This can then be calculated for every gridbox in the tropics where convection occurs.

To calculate f_{det}, a new flag is introduced into the TSC dataset in order to keep track of where a given air parcel originated from. When convection occurs, the latitude and longitude of the convective location are flagged, and these remain with the air parcel until it is replaced by new convection (much like how the land ocean flag works). Across the entire 17 year dataset, a map of the probability of finding detrained cirrus from a given location of convection is generated. Figure 5.3 shows an example of these probability maps, for three 10x10 deg convective regions. This highlights how detrained cirrus from convection can travel far from the source of convection. This shows the importance of considering the non-local radiative impact that changes in the prop-

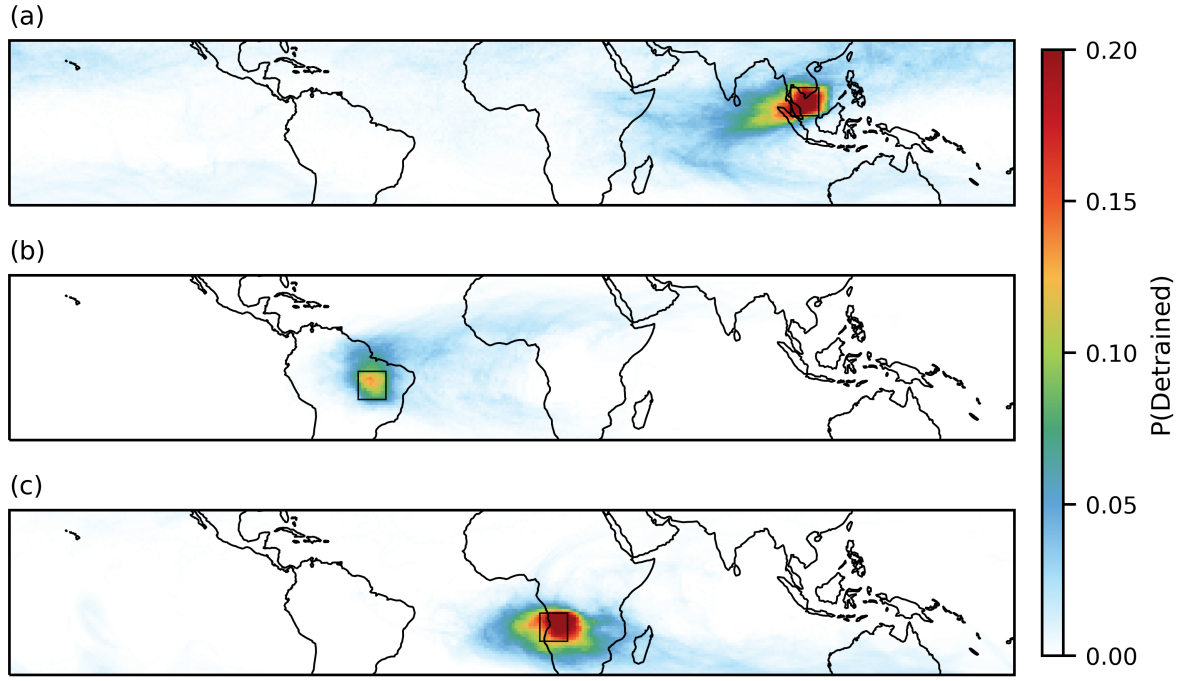


Figure 5.3: Heatmap of the probability of finding detrained cirrus which originated from 10x10°gridboxes between (a) (0N-10N, 60E-70E), (b) (20S-10S, 120E-130E), (c) (20S-10S, 10E-20E). These maps are for the year 2002.

erties of convection could have in regions far from the convection itself, providing this change in convection translates to some change in the cirrus properties themselves.

Equation 5.1 can then be expanded to include the f_{det} ($= P(det|conv)$) term, and thus calculated the non-local sensitivity not captured in Equation 5.1. This equation now maps the AOD-CTP sensitivity in convective space c, to the CRE-CTP sensitivity in convective space d:

$$\Delta CRE_d = \sum_c \left[P(det|conv)_{cd} \times P(conv)_c \times CTP \frac{dlnCTP}{dlnAOD}\bigg|_c \times \Delta lnAOD_c \right] \times \frac{dCRE}{dCTP} \quad (5.2)$$

The summation over c in Equation 5.2 represents summing over each convective gridbox in Figure 5.2a, where $P(det|conv)_{cd}$ is a map of the probability distribution of de-

trained cirrus given a convective event from each gridbox (Figure 5.2b). The $P(conv)$ term also has to be included to account for the fact that convection does not occur at all times in all gridboxes. The sensitivity of CTP to AOD is for each gridbox in Figure 5.2a. The $\Delta lnAOD$ is estimated by Bellouin et al. (2013).

Note, the sum of the $P(det|conv)$ and $P(conv)$ is simplified as:

$$P(det|conv)_{cd}P(conv)_c = \frac{N(det)_d}{N(conv)_c}\frac{N(conv)_c}{N(tot)_c} = \frac{N(det)_d}{N(tot)_c} = P(det)_{cd} \tag{5.3}$$

where $N(tot)$ is the total number of data points for each grid box. This equation simplifies to give $P(det)_{cd}$, which is the probability of finding detrained cirrus in detrained space, given some convection at a given grid box in convective space.

This means that the final equation becomes:

$$\Delta CRE_d = \sum_c \left[P(det)_{cd} \times CTP \left.\frac{dlnCTP}{dlnAOD}\right|_c \times \Delta lnAOD_c \right] \times \frac{dCRE}{dCTP} \tag{5.4}$$

With this equation, it is possible to link the change of CRE of detrained cirrus, via the CTP, to a given change in the AOD at the location of convection. This approach is vital to link local change at the location of convection to a non-local response in the cirrus cloud properties away from the initial perturbation.

5.2.1 Convective strength flag

The convective strength flag bins each convective event according to its cloud-top pressure (CTP), where the CTP serves as a proxy for the convective strength. Much like the land-ocean flag introduced in the previous chapter, this flag is a property of the air parcels as they are advected from convection. This allows the evolution of air parcels from deep convection to be separated and investigated according to the initial CTP of the deep convection from which they came.

Four CTP bins are used, shown in the table below, with their associated flag value:

Flag label	**CTP bin (hPa)**	**Flag value**
Shallow	$175 \leq Pc \leq 200$	1500
Mid-shallow	$150 \leq Pc < 175$	500
Mid-deep	$125 \leq Pc < 150$	-500
Deep	$100 \leq Pc < 125$	-1500

Table 5.1: Convective strength bins and associated flag value of each bin.

It is necessary to assign discrete, evenly spaced flag values to the initial convection because interpolation occurs where pixels diverge as the air parcels advect along trajectories from convection. This means that, much like the land-ocean flag and the TSC values themselves, the interpolated flag value in a divergent gridbox is the mean of the surrounding gridboxes. This introduces some uncertainty - for example, if the gridboxes surrounding a divergent air parcel contain an equal number of shallow (flag value 1500) and deep air parcels (flag value -1500), the resulting flag value of the divergent grid box will be zero. This will incorrectly represent some mid-shallow or mid-deep convection. In practice, the likelihood of this happening is low. However, it does mean that the confidence in the flag value decreases further along trajectories, such that there is less trust in the flag value accurately representing the origin of the air parcel. By binning the initial convective strength, rather than assigning the air parcel with the actual CTP, the statistical confidence of each pressure level is increased as

there is more data in each bin, and the impact of uncertainty due to interpolated divergent gridboxes is reduced. In the case of convergence, the flag value that fills the gridbox is the value associated with lowest TSC that also fills the gridbox.

5.2.2 Sensitivity of detrained cirrus CRE to initial convective CTP

In order to investigate the relationship between the initial convective strength and the CRE of the detrained cirrus clouds, the sensitivity of CRE to CTP is calculated. The CRE of detrained cirrus along trajectories from deep convection is calculated in the same way as in Chapter 4, here for each separate convective strength bin. As in previous chapters, the lifetime CRE values are calculated as the weighted mean of the CRE along trajectories. The sensitivity of CRE to CTP is calculated as the slope of the linear regression of the CRE for each CTP bin. This is calculated for each year from 2000-2016, excluding 2009. The sensitivity's final value is the mean of the sensitivity across the whole study period.

5.2.3 Sensitivity of CTP to AOD

The sensitivity of CTP to AOD is calculated in order to bridge the sensitivity of the detrained cirrus CRE to the AOD at the location of convection. 17 years (2000-2016) of MODIS Terra aerosol (Remer et al., 2005) daily level 3 data are used at 1x1° between 30S-30N to retrieve the AOD. The dark-target MODIS AOD retrieval 'Optical Depth Land and Ocean Mean' is used.

The CTP is retrieved from the 1x1 degree ISCCP-H (Rossow et al., 2017) cloud product used in the previous chapters. The native 3-hourly resolution of the ISCCP data is

converted to a daily mean in order to compare directly to the MODIS AOD retrieval. The sensitivity is also defined as the slope of the linear regression between the lnCTP and lnAOD in each 1x1 degree gridbox. The sensitivities are calculated seasonally in order to avoid errors (Grandey et al., 2018), and combined using a standard error weighted mean.

5.3 Results

5.3.1 Convective strength contrasts

Figure 5.4 shows the probability density of the CTP of convection for the period 1984-2017, coloured by each convective strength bin in the TSC dataset. The majority of convection that occurs in the highest two CTP bins (weakest convection), peaking in the 175-180hPa bin, with the smallest amount in the strongest CTP bin. There is very little interannual variability in the distribution of CTP across the study period (not shown).

Figure 5.5 shows the probability density of the regional distribution of detrained cirrus arising from convection in each of the four convective strength bins. The probability density maps are normalised such that each map sums to 1. This allows for a direct comparison between bins that contain different amounts of total detrained cirrus. Panels (a,b,d,e) show the absolute probability density, whilst panels (c,f,g,h,i) show the differences between panels, as labeled above each panel).

It is evident from panels (a,b,d,e) that the overall distribution of detrained cirrus is similar for each convective strength bin, however there is a clear difference in the land and

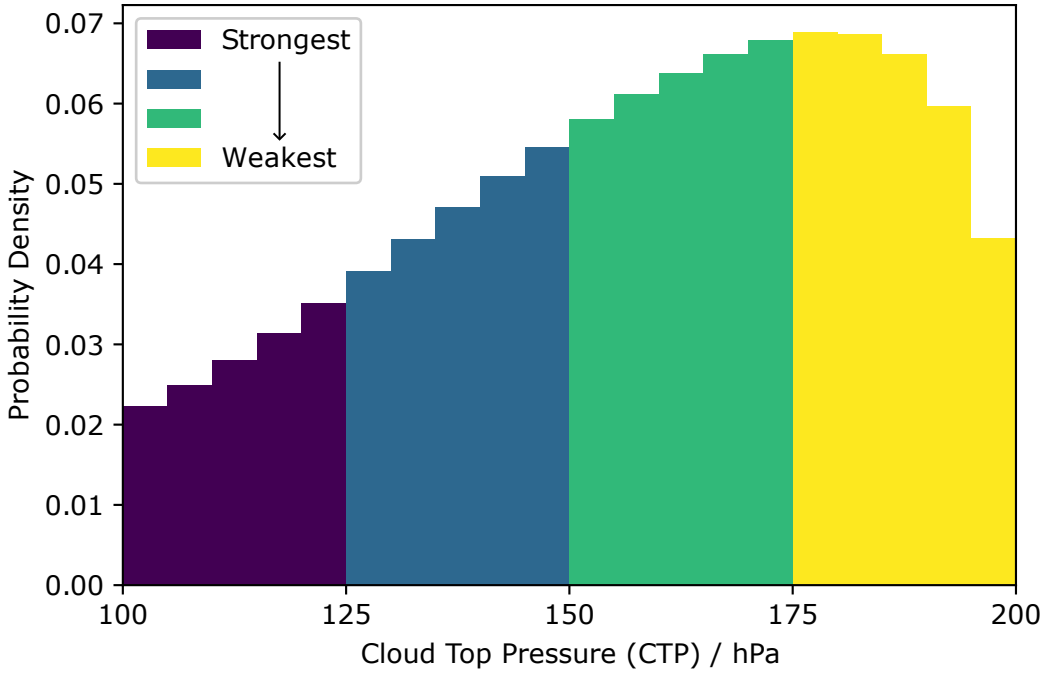


Figure 5.4: Probability density of the cloud top pressure of convection between 1984-2017. The coloured bins represent the convective strength bins used in the TSC dataset.

ocean distribution between weak convection and strong convection. Panel (i) shows the difference in the distribution of detrained cirrus between the strongest convection bin, panel (a), and the weakest convection bin (panel (e)). The detrained cirrus flags also include the locations of the original convection, therefore these comparisons also account for differences in the amount of convection in each bin, as well as differences in the detrained cirrus. Panel (i) shows that the strongest convection and associated cirrus occur much more predominantly over central Africa, and southern South America, and South and South East Asia, including parts of China. In general, stronger convection and detrained cirrus from strong convection, occurs more often over land than ocean, with most of the shallower convection occurring over the Maritime Continent, the ITCZ and to a lesser extent over northern South America.

Stronger convection is more likely to occur over land than ocean, as shown in multiple observational studies (Cecil et al., 2014; Christian et al., 2003; Liu et al., 2007; Taka-

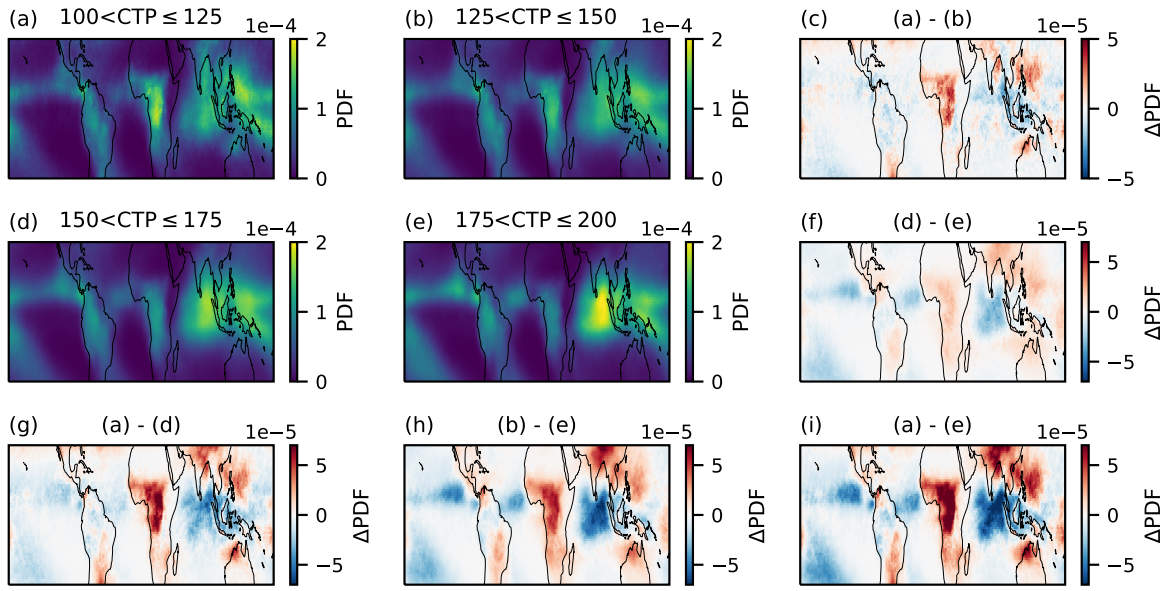


Figure 5.5: (a,b,d,e) shows the regional probability density of detrained cirrus originating from each convective strength bin. (c,f,g,h,i) shows the difference between the probability density for specific convective strength bins. The probability density is normalised such that each map adds up to one, allowing for a direct comparison between bins that contain different amounts of detrained cirrus.

hashi et al., 2017). There is some suggestion that the land-ocean contrast in convective strength may be due in part to differences in aerosol concentrations (Fan et al., 2013; Rosenfeld et al., 2008; Tao et al., 2012).

5.3.2 Diurnal cycle of land and oceanic convection

Figure 5.6 shows the diurnal cycle of convection for the four convective strength bins of all, land, and ocean-origin convection. The probability density (i.e. the probability of convection occurring in that hour) is calculated from the mean diurnal cycle between 1984-2017. Panel (a) shows the diurnal cycle for all origin convection. There is a significant difference in the diurnal cycle between convection strengths. The weakest convection peaks in the mid-afternoon, with a significantly smaller peak in the morning at around 09:00 LST. There is very little convective activity for the weakest con-

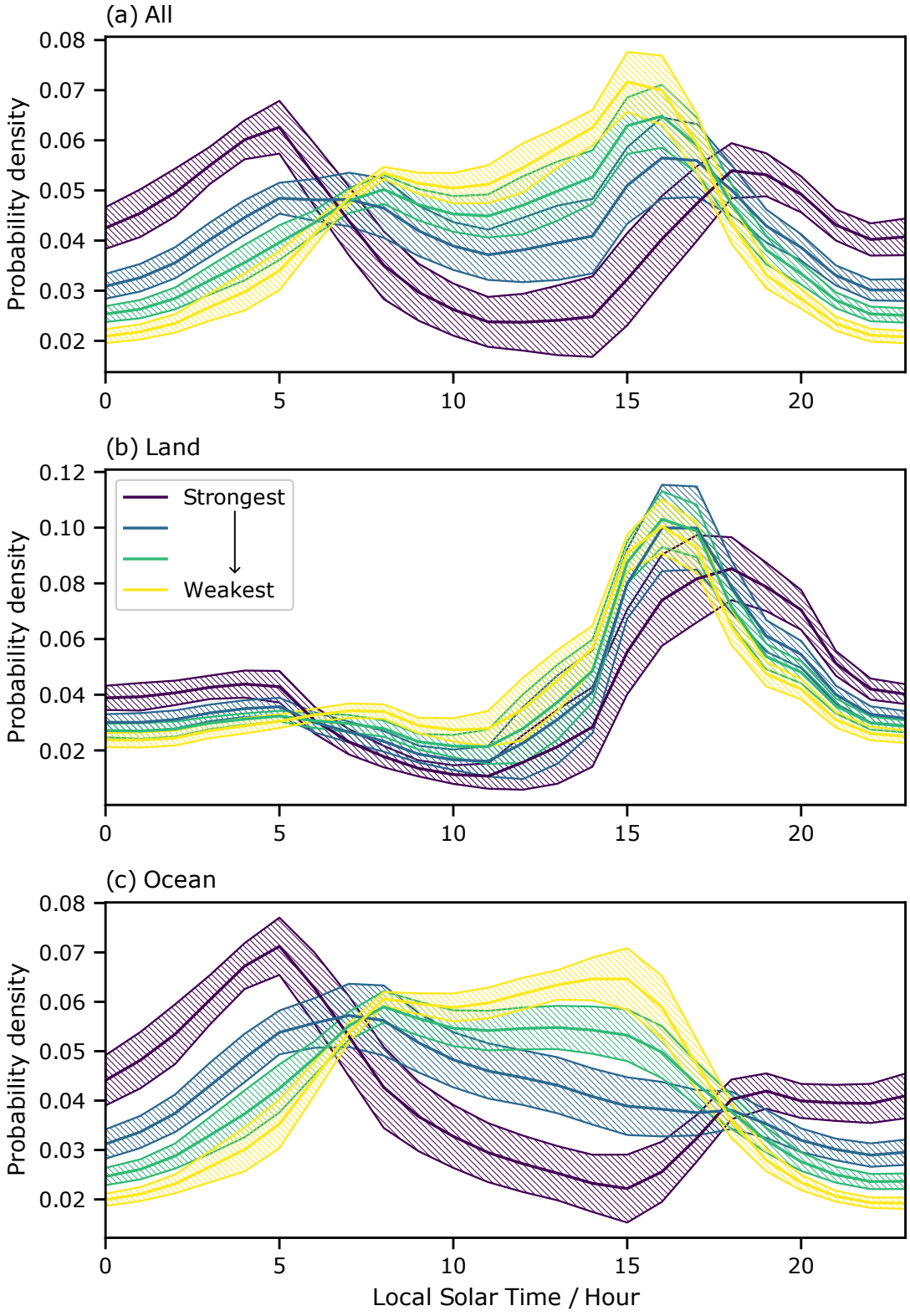


Figure 5.6: The diurnal cycle of convection, binned by convective strength, for a) all convection, b) land convection, and c) ocean convection. The diurnal cycles are normalised such that they all sum to 1, to allow for direct comparison between different weighted bins.

vection during the solar night. As convective strength increases, the afternoon peak in convective activity decreases and shifts later into the afternoon, and the morning peak increases in intensity and shifts earlier. There is also significantly less stronger convection in the middle of the solar day. The strongest convection bin has a markedly different diurnal cycle than the weaker three bins, with the largest peak in the morning at around 05:00 LST. This is followed by a minima in the day, a smaller peak in late afternoon convection, and significantly more nighttime convection.

Panel (b) shows the diurnal cycle for land convection. Here, as shown in Chapter 4, the diurnal cycle is significantly different from the all convection case. All land convection, regardless of strength, peaks in the mid-late afternoon. Generally, the weaker convection peaks earlier in the afternoon, with the strongest convection peaking around 17:00LST. The peak is much broader for strong convection, showing that these cases occur much more variably throughout the afternoon. By contrast, the weakest convection has a much more concentrated peak in activity. As with panel (a), there is more weak convection during the day and less during night. However, this contrast is less pronounced than panel (a).

The diurnal cycle of oceanic convection (Figure 4.4c) looks markedly different to the land convection, but accounts for much of the pattern seen in the all convection case, since there is much more oceanic convection than land. As with all convection, weaker oceanic convection peaks in the afternoon, at 15:00 LST, with a smaller peak in the morning. As the convection strengthens, the afternoon peak decreases, with the morning peak shifting further into the morning. Unlike all convection, there is no land contribution, and as such, the afternoon convective peak disappears for all but the weakest convection. The strongest convection peaks at 05:00, with very little activity throughout the solar day. As with the two panels above, over the ocean, there is stronger convection at night.

These diurnal cycles are well understood for both oceanic and land convection. Stronger land convection peaks later in the day since land convection is strongly controlled by terrestrial heating. It is also well understood that stronger oceanic convection occurs in the night and early morning, with weaker convection occurring more readily throughout the day (Yang and Slingo, 2001).

Figure 5.7 shows the modal time of convection for a) all convective strength bins, b) the weakest and c) the strongest convection strength bins. From panel (a), the land-ocean diurnal contrast is clear, with land convection peaking in the middle to late afternoon and ocean convection varying more but generally occurring throughout the night and early morning. There are interesting signals along coastlines, particularly visible around the Maritime Continent and the Bay of Bengal, which show oceanic convection occurring later in the morning. This is indicative of offshore breezes leading to deep convective initiation in the morning (Wapler and Lane, 2012). In general, oceanic convection appears to occur earlier in the day in the eastern Pacific and in the southern Indian Ocean than in the Maritime Continent. Perhaps again due to interactions with land.

The weakest oceanic convection generally occurs much later in the day than the strongest convection, with weak convection occurring around solar noon, and the strongest convection occurring in the night and early morning, as shown in Figure 5.6c. The timing of the weakest oceanic convection is more homogeneous throughout the tropics, with almost all the convection occurring during the solar day. Panel (c) shows evidence of sea breezes initiating deep convection around the coastlines. The Bay of Bengal and the Maritime Continent show convection occurring later into the morning than the more isolated oceanic convection in the Atlantic, Pacific and Indian Oceans. Over land, the timing of convection is more uniform across regions, with the stronger convection occurring later in the day than the weakest convection (see Figure 5.6b). These results are

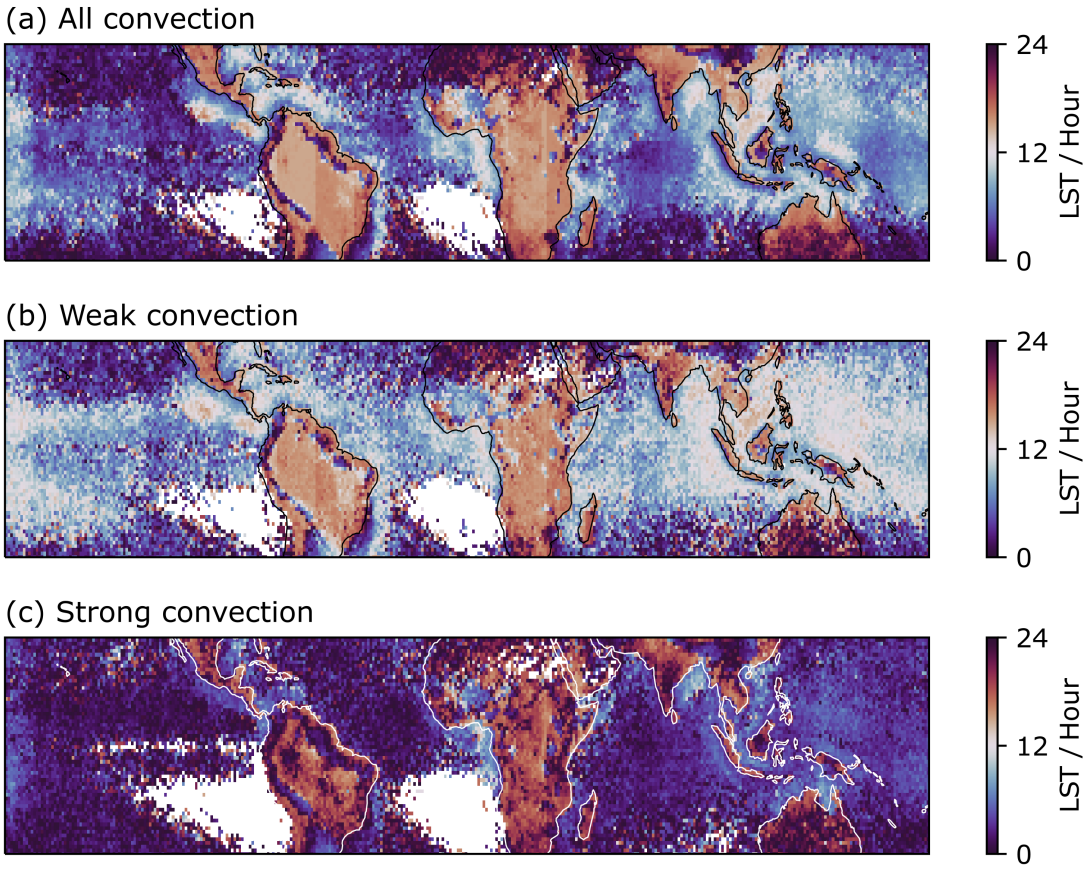


Figure 5.7: The modal local solar time of convection for a) all convection. b) the weakest convective strength bin. c) the strongest convective strength bin.

consistent with those found by Yang and Slingo (2001), particularly regarding the pattern of timing in the Bay of Bengal, however Yang and Slingo (2001) did not separate out the timing of convection by convective strength.

5.3.3 Relationship between convective strength and detrained cirrus CRE

Figure 5.8 shows the net, SW, and LW CRE of detrained cirrus for each convective strength bin and land-origin and ocean-origin bin. In all origin cases (Figure 5.8a,d,g) there is a significant difference in the CRE evolution depending on the initial strength

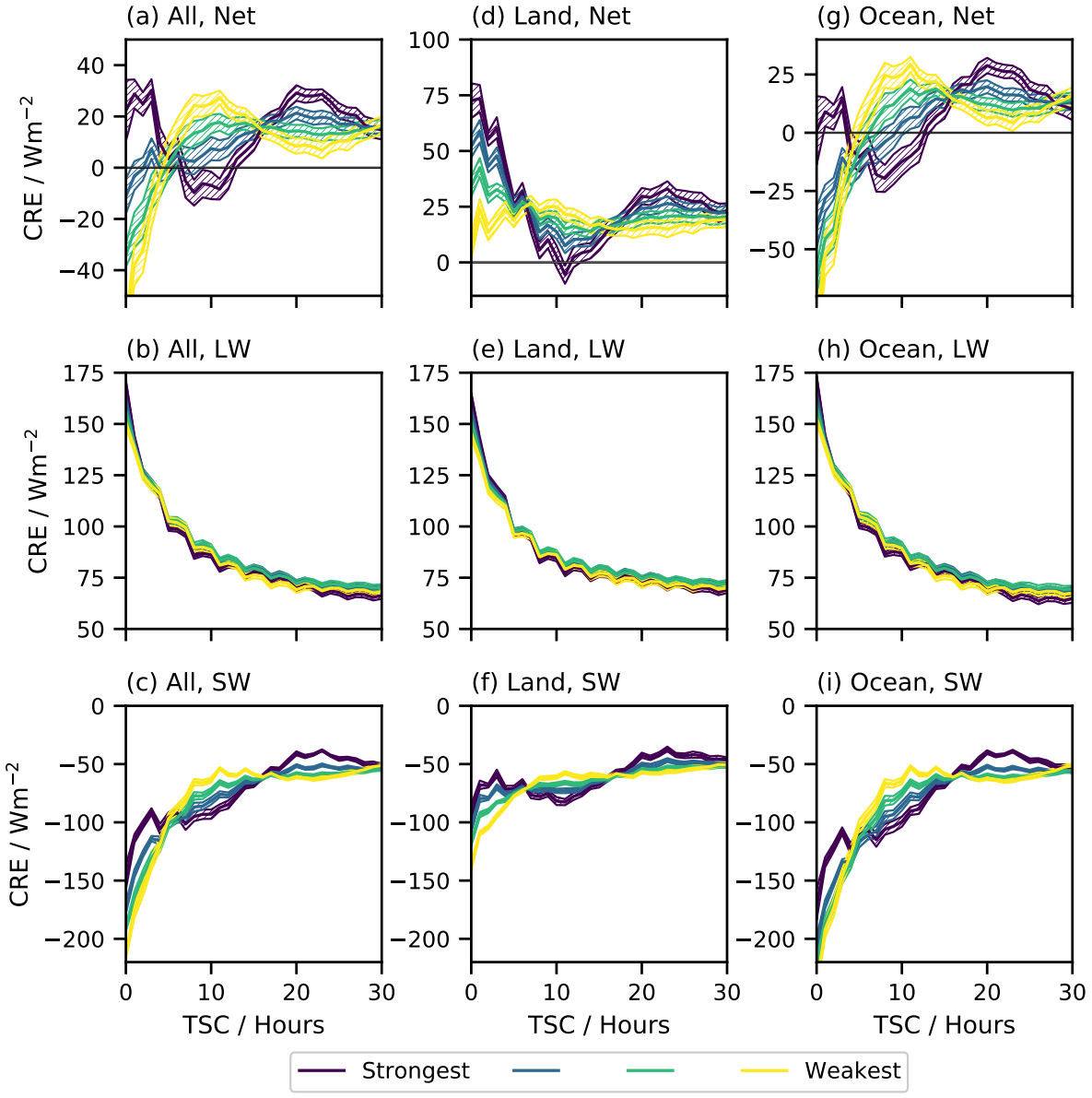


Figure 5.8: Net, LW, SW CRE as a function of TSC for all origin (a,b,c), land-origin (d,e,f), and ocean-origin (g,h,i) detrained cirrus in each convective strength bin. Note the TSC is only up to 30 hours, as this is where the majority of the difference in the CRE occurs.

of the convection. There is also a significant difference in the CRE at TSC-0, i.e. the CRE of the deep convection itself.

The CRE at TSC-0 increases with convective strength for all, land, and oceanic convection. The differences in net CRE are caused overwhelmingly by differences in the SW CRE (Figure 5.8c,f,i), where stronger convection has a smaller SW CRE. This is due to the timing of the initial convection, as shown in Figure 5.6, where the stronger convection occurs during periods when the incoming solar radiation is lower, thus reducing the SW cooling. Over land, this is a shift later (Figure 5.6b). Over ocean, this is a shift earlier in the morning, before sunrise (Figure 5.6c). The LW CRE at TSC-0 also follows a similar pattern. In this case the stronger convection has a greater LW CRE. This difference is around half the difference in the SW CRE.

Considering first the land-origin evolution (panels d,e,f), the evolution of the detrained cirrus heavily depends on the initial strength of convection, with detrained cirrus from strong convection exhibiting a stronger diurnal cycle in the CRE than cirrus from weaker convection. Detrained cirrus from stronger convection initially has a much larger net CRE due to a less negative SW, given that it is much more likely to occur later in the day than weaker convection, thus minimising any SW cooling. By contrast, detrained cirrus from weak convection occurs more uniformly throughout the day (although still peaking in the afternoon, as shown in Figure 5.6a. This minimises any initial warming and reduces the appearance of the diurnal cycle on the subsequent CRE evolution. At 10 hours from convection, the detrained cirrus from strong convection cools more than from weaker convection due to a stronger SW cooling (Figure 5.8a,c). By 25 hours, the detrained cirrus from strong convection is more warming than cirrus from weak convection. These differences are almost entirely due to changes in the timing of initial convection. There is little difference in the detrained cirrus LW CRE evolution between convective strength bins.

As previously mentioned, the ocean-origin evolution (panels g,h,i) accounts for much of the pattern in the all-origin since most convection occurs over the ocean. The ocean-origin CRE evolution is slightly more complex than land-origin, where the diurnal cycle only peaks once in the afternoon. As was the case for the land-origin, the evolution of the net CRE is modulated mostly by changes in the SW CRE, which in turn is determined by the timing of the initial convection. The detrained cirrus from weaker convection shows a more typical CRE evolution, as shown in Figure 3.10 in Chapter 2. That is, an initial cooling from thicker anvils before a combination of cirrus thinning and reduction in the incoming SW solar radiation causes the net CRE to become positive. Figure 5.6c showed that weaker oceanic convection also occurs uniformly throughout the day, meaning that the evolution of the CRE follows a predictable pattern of cooling to warming.

The stronger ocean-origin detrained cirrus CRE evolution follows a different pattern. Beginning with a close to zero net CRE, it initially warms before cooling to a minimum at 10 hours from convection. After this point, it begins to steadily warm to a maximum at 20 hours from convection, warming more than weaker convection. This change in evolution can also be attributed to contrasts in the diurnal cycle, shown in Figure 5.6c. The stronger convection shifts to peaking in the early morning, at 05:00LST, just before sunrise for most of the tropics. This means that the initial convection has a decreased SW cooling during its early evolution; however, it becomes more cooling 5-10 hours from convection when the incoming solar radiation, and thus SW CRE, begins to peak. The stronger convection CRE evolution is essentially out of phase with the weaker convection due to the shift in when the initial convection occurs. These differences, when combined with the natural thinning of the detrained cirrus over the same period, and the changes in decay times due to radiative cooling at night (Gasparini et al., 2022), magnify to give very a different characteristic CRE evolution for strong versus weak initial convection.

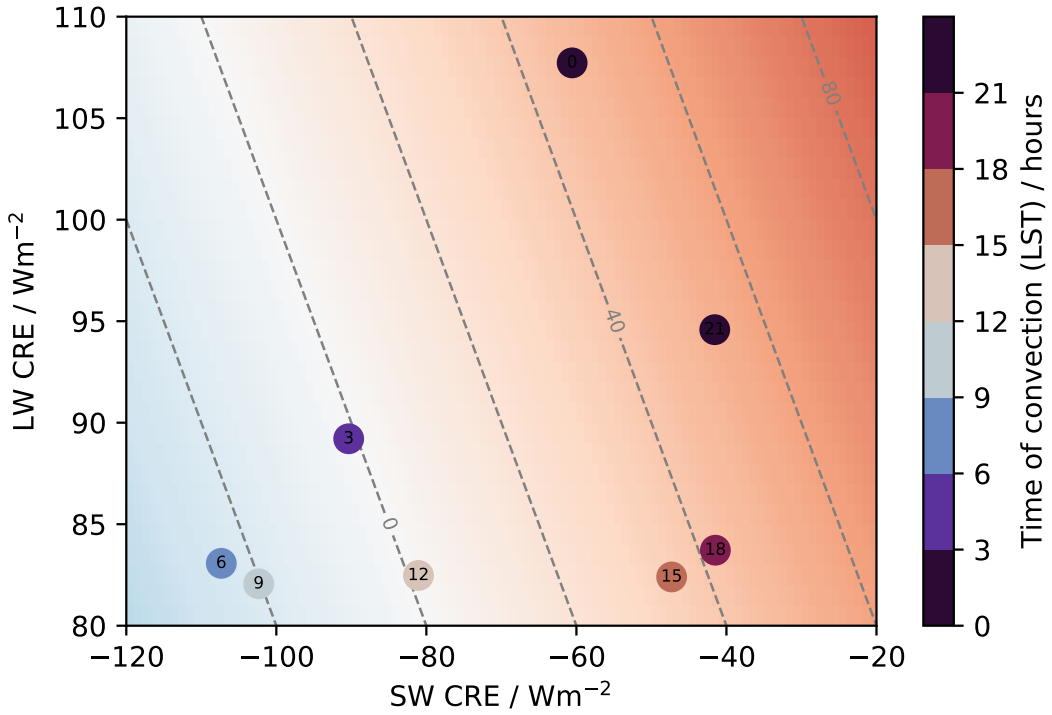


Figure 5.9: LW and SW lifetime detrained cirrus CRE binned by local solar time of convective initiation.

The net CRE is highly sensitive to the initial convective strength in all cases. This sensitivity comes mostly from changes in the SW but also differences in the LW. The SW sensitivity is mostly due to changes in the diurnal cycle of convection of different strengths. The changes in the LW are less dependent on the diurnal cycle, shown by the fact that the LW evolution is very similar for land and ocean-origin cases, where the convection has a different diurnal cycle.

Figure 5.9 shows the mean lifetime SW and LW CRE for detrained cirrus from convection according to the local solar time of convective initiation. This figure, which is an adaptation of a figure from Gasparini et al. (2022), reinforces the argument made above, that the timing of the initial convection strongly impacts the CRE of detrained cirrus. Convection that occurs in the early morning, between 6am and 12pm, generates detrained cirrus with the largest cooling effect. If convection occurs later in the day, the

SW cooling decreases significantly, leading to a net warming CRE. Convection that occurs between 6pm and midnight leads to detrained cirrus with the largest warming. All convection that occurs after midday leads to detrained cirrus having a net warming effect over their entire lifetime.

The LW CRE also varies with the timing of convective initiation, however this variation is much smaller than the SW variation. This LW CRE pattern is due to contrasting diurnal cycles of convection of different strengths as shown in Figure 5.6. Stronger convection occurs more often during the night than weaker convection. This leads to higher altitude deep convection and detrained cirrus outflowing at higher altitudes. This causes an increase in the LW warming due to colder cloud tops. This explains why convection that occurs between 9pm and 6am typically has a larger LW warming. Although not shown, Figure 5.9 looks approximately similar for both land-origin and ocean-origin convection, however there are differences in the LW CRE, due to differences in the diurnal cycle contrasts between strong and weak convection over ocean and land, as shown in Figures 5.6b and c).

As shown in Chapter 4, the contrast in the land-ocean diurnal cycle is responsible for large differences in the cloud radiative effect of land-origin and ocean-origin detrained cirrus, particularly in the early stages of their evolution. Given the significant differences in the diurnal cycle of convection of different strengths, even within land-ocean convective bins, the strength of the initial convection is shown here to greatly impact the evolution and lifetime CRE of detrained cirrus.

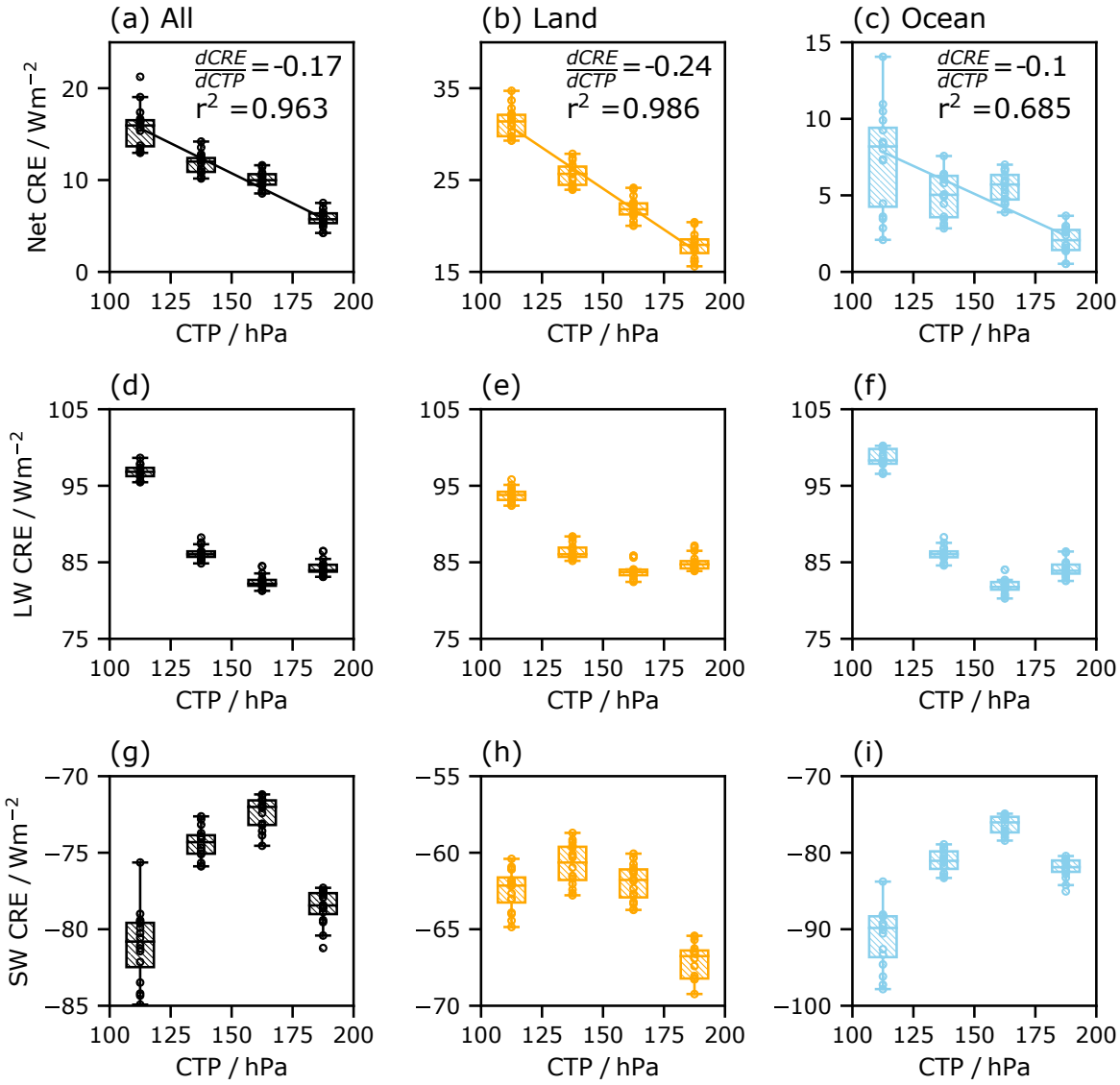


Figure 5.10: Sensitivity of detrained cirrus net CRE to deep convective CTP for a) all origin, b) land-origin, and c) ocean-origin. As above for d,e,f) LW CRE and g,h,i) SW CRE.

5.3.4 Sensitivity of CRE to initial CTP

To understand the impact that convective strength has on the lifetime CRE of detrained cirrus, Figure 5.10 shows the lifetime net, LW and SW CRE for each convective strength bin, for all, land, and ocean-origin. The linear regression shows the relationship between the CRE and CTP. The sensitivity for the all-origin case is -0.17$Wm^{-2}hPa^{-1}$. The sensitivity is higher, with a value of -0.24$Wm^{-2}hPa^{-1}$, for land-origin detrained cirrus. The sensitivity is -0.10$Wm^{-2}hPa^{-1}$ for ocean-origin detrained cirrus. It should be noted that, whilst there is a good linear fit to the sensitivity for the all and land case, the fit is less robust for the ocean case, suggesting that the relationship between CRE and CTP is weaker for oceanic convection. This weakness in the relationship comes from large interannual variability in the SW CRE of the strongest oceanic detrained cirrus.

Figure 5.10d,e,f show the LW CRE binned by convective strength for all, land, and ocean-origin detrained cirrus. There is very little difference in the sensitivity between cirrus of land or ocean-origin. This supports the above results that the LW forcing is less sensitive to the timing of convection and the different diurnal cycles of land and ocean convection and is more a function of the strength of the initial convection, as shown in Figure 5.9. Comparing the strongest and weakest convection bins, there is a clear decrease in the LW CRE across the whole lifetime of the detrained cirrus.

Figure 5.10g,h,i shows the SW CRE binned by convective strength for all, land, and ocean-origin detrained cirrus. Unlike the LW, the SW CRE is very sensitive to the diurnal cycle of convection, and thus, the magnitude of the lifetime CREs are very different for land and ocean-origin detrained cirrus. The land-origin SW CREs are much less negative for all convective strength bins. Interestingly, the shape of the non-linearity between land and ocean-origin sensitivities is different, with the least cooling land bin being 120-150hPa and the least cooling ocean bin being 150-175hPa. This is

due to the contrasting diurnal cycles of convection of different strength for land and ocean, as shown in Figure 5.6b and c).

For land-origin cirrus, the SW sensitivity is straightforward; stronger convection occurs later in the afternoon, and slightly more readily throughout the night, thus reducing the opportunity for SW cooling in the early stages of detrained cirrus evolution. This means that detrained cirrus from stronger convection is typically more warming over the entire lifetime, as the detrained cirrus will have sufficiently dissipated by the next day. The strongest bin is slightly more cooling than the middle two bins (although still within the uncertainty range of each other). This is because the strongest land bin contains more convection which occurs between 3am and 6am (see Figure 5.6b), therefore there will be more thick, young anvils persisting into the day and cooling than for the weaker bins which have less very early morning convection (Figure 5.9). This is also clear from Figure 5.8f), which shows that the strongest convective bin cools most from around 10 hours from convection, even though it is the most warming during the initial hours of convection. This highlights just how complex the evolution is and the impact that this has when summed to give the lifetime SW CRE values.

For ocean-origin cirrus, the relationship is even more complicated. As shown in Figure 5.6c, the change in diurnal cycle for increasing convective strength is more stark. Stronger convection shifts to the early morning before sunrise (Figure 5.7c), which maximises the SW cooling later in the evolution of the detrained cirrus, when the detrained cirrus will still be optically thick enough to have a large cooling effect. This is clearly shown in Figure 5.9, which shows early morning convection having the largest SW cooling. However, stronger convection also occurs more often at night, meaning that some detrained cirrus from oceanic convection will have a significant warming in the early stages of their evolution. Figure 5.10i shows this impact in the SW CRE sensitivity to the CTP. The strongest convective bin is the most cooling in the SW, due

to the convection occurring just before sunrise. In all cases, the SW cooling over the ocean is greater, likely due to the timing and the difference in albedo between ocean and land.

The SW and LW CRE for land and ocean-origin detrained cirrus (Figure 5.10e,f and 5.10h,i) sum together to give the sensitivities shown in panels b and c. For the ocean case, the SW and LW are almost mirrored, with a small offset such that the net CRE is positive for all convective bins. Stronger oceanic convection leads to a larger LW cirrus warming, likely due to the detrainment height of the cirrus. However, stronger oceanic convection also leads to a larger SW cooling due to the timing of the stronger convection relative to the weaker convection. This is also highlighted clearly in Figure 5.9. The difference in the SW and LW is not the same for each convection bin, leading to the small overall sensitivity seen in Figure 5.10c.

For land-origin cirrus the SW and LW are not mirrored in the same way as the ocean-origin cirrus. For these cirrus the SW and LW CRE add in such a way to increase the sensitivity of CRE to CTP. The absolute magnitude of the net CRE is also much larger due to a smaller absolute SW cooling (again, due to a combination of the timing of convection and the impact of surface albedo on the CRE, see Figure 4.8 in Chapter 4). Interestingly, the two different non-linear sensitivities in the SW and LW CRE sum give a robust relationship between CRE and CTP for land-origin cirrus.

There is much lower interannual variability in the LW CRE than the SW CRE. This is more evidence for the independence of the LW CRE to the timing of convection. Most of the interannual variability in the net CRE comes from the SW CRE, which will be investigated further later in this chapter.

It is clear from Figure 5.10a,b,c that there is a strong relationship, particularly for land-origin cirrus, between the lifetime CRE and the initial CTP of the convection. In gen-

eral, stronger initial convection leads to warmer detrained cirrus are over their whole lifetime. Whilst some of this is down to the timing of the convection, and thus the response in the SW CRE, there is a positive relationship between the LW CRE and the initial convective strength. This is true for both land and ocean convection, showing that when the impact of the diurnal cycle is removed (i.e. the SW CRE contributions), there is little difference in the LW CRE of the land and ocean detrained cirrus.

5.3.5 Trends in the CRE-CTP sensitivity

Figure 5.11 shows the time series of the CRE-CTP sensitivity between 2000 and 2016 for all-origin, land-origin, and ocean-origin detrained cirrus. Interestingly, there is significant divergence between the trends for land-origin and ocean-origin detrained cirrus. The land-origin CRE-CTP sensitivity is essentially constant for the entire time series, ranging between -0.25Wm^{-2}hPa^{-1} and -0.22Wm^{-2}hPa^{-1}. By contrast, the ocean-origin CRE-CTP varies signficantly across the time series, from -0.16Wm^{-2}hPa^{-1} in 2000, to almost zero between 2006 and 2010, before decreasing again down to -0.15Wm^{-2}hPa^{-1} in 2016. This suggest there is some mechanism that provides variability in the CRE-CTP relationship over ocean that doesn't exist over land.

As can be seen from the error bars in Figure 5.10c), most of the variability in the CRE-CTP relationship is driven by variability in the net CRE of the strongest convection bin, which in turn is driven mostly by variability in the SW CRE. This is shown more clearly in Figure 5.12 which shows the change in the net, LW, and SW CRE of each CTP bin across the entire study period, relative to a baseline value of 0 in the year 2000.

Panel (a) shows the net CRE of the land-origin detrained cirrus over the study period relative to the baseline CRE in 2000. In general, there is a decrease in the net CRE

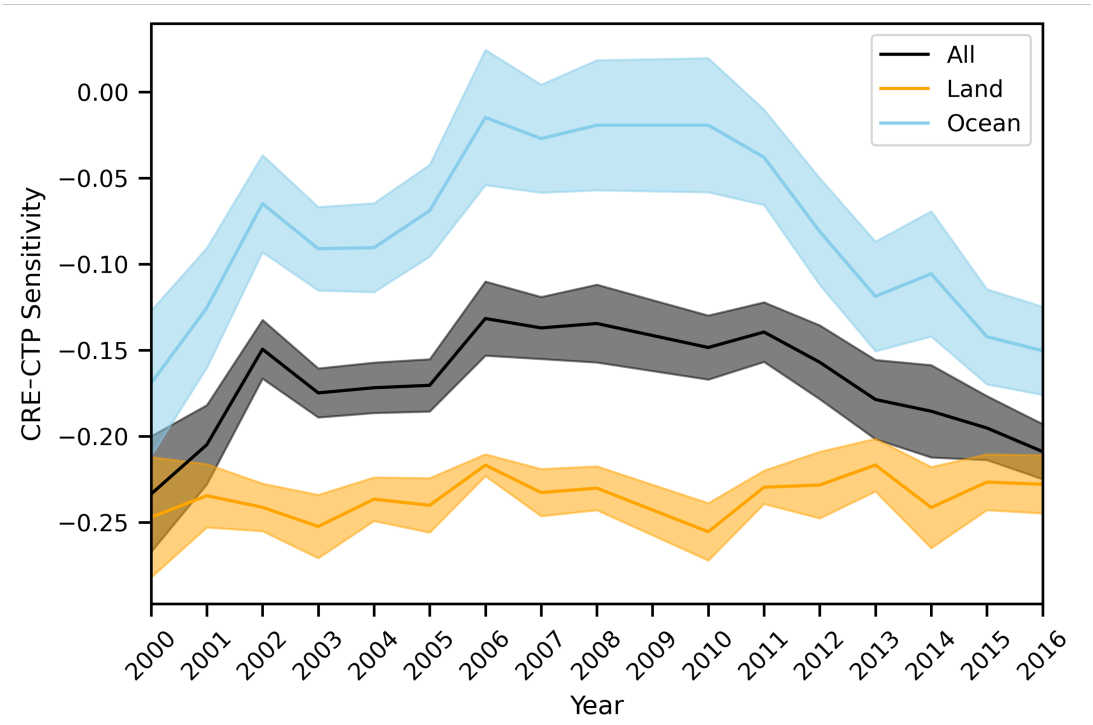


Figure 5.11: Timeseries of the CRE-CTP sensitivity for all origin (black), land-origin (orange line), and ocean-origin (blue) detrained cirrus. The shaded area represents the uncertainty on the linear fit for each year (Note: excluded 2009 data is interpolated).

for all pressure bins, to a minimum between 2006-2010, before increasing slightly by 2016, where the net CRE is around -3Wm^{-2} lower than the year 2000. Given that the difference in the CRE between each pressure bin is relatively constant over the study period (with the strongest convection bin generally decreasing more than the other bins), this accounts for the almost constant sensitivity over land shown in Figure 5.12.

Panels c and e show the separate contributions of the LW and SW to the net CRE over the study period. Over land, there is a similar variability in both LW and SW. After a sharp drop in 2001, the LW CRE does not vary signficantly over the study period. The SW CRE decreased slightly to a minimum between 2006 and 2008, with the strongest convection bin decreasing more than the other 3 bins. In general, there is little variation in the spread of the strength bins over the study period, keeping the sensitivity constant. However there is a decrease in absolute CRE values over this period, driven by both decreases in the LW and decreases in the SW CRE.

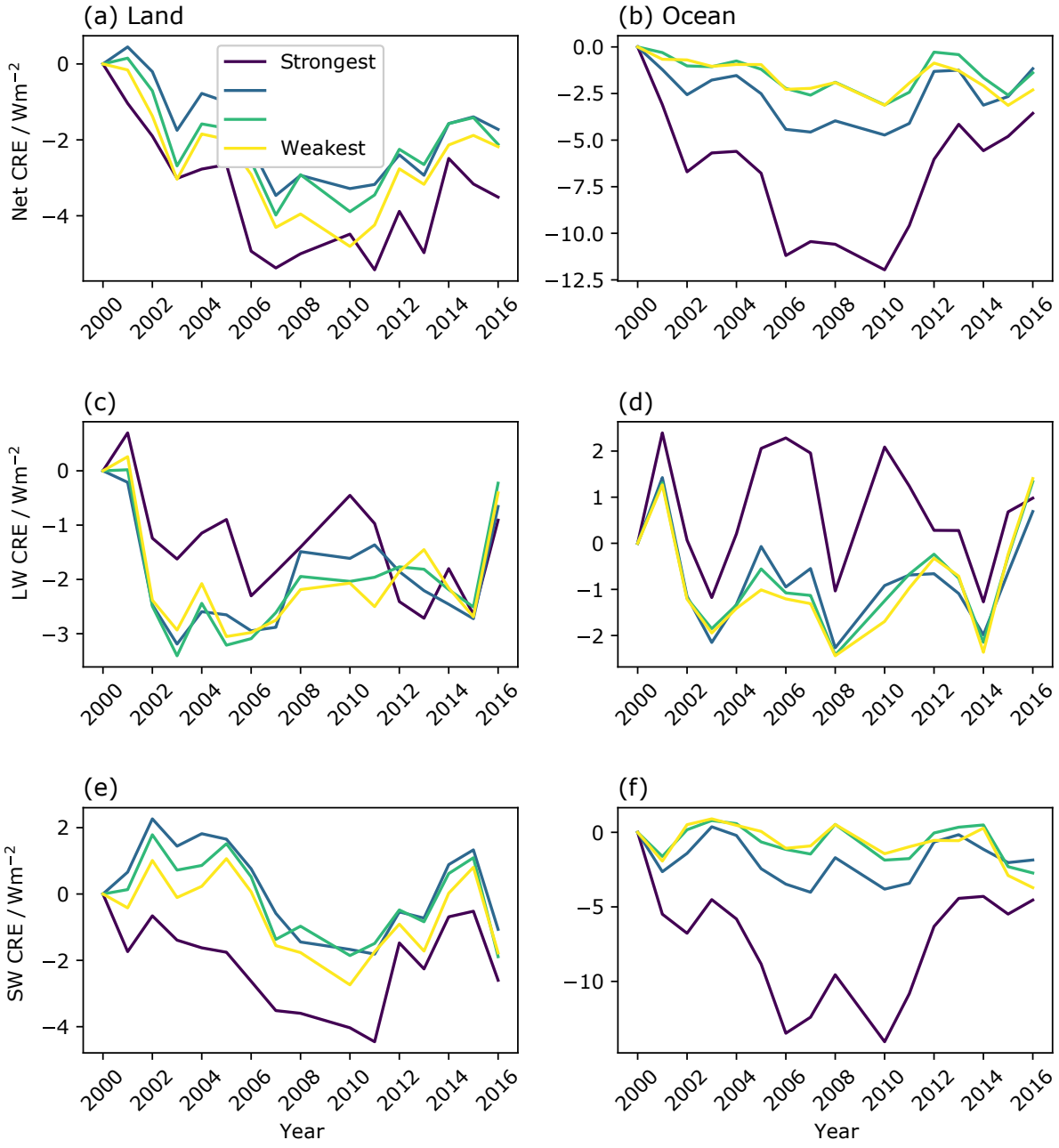


Figure 5.12: Timeseries of the net, LW, SW, CRE for each convective strength bin, for land-origin and ocean-origin detrained cirrus. Results are normalised to a baseline where the CRE in 2000=0 (Note: excluded 2009 data is interpolated).

Panel (b) shows the net CRE of the ocean-origin detrained cirrus over the study period. Interestingly, the decrease in the net CRE of the 3 weaker convective bins is comparable to the decrease in the land-origin net CRE shown in panel (a); however, there is a significantly larger decrease in the strongest convective bin. Between 2006-2010, the net CRE of the strongest convective bin is almost 12Wm^{-2} lower than the baseline year 2000, whereas the weaker 3 bins are between -2Wm^{-2} and -5Wm^{-2} lower. By 2016, the strongest bin is about -4Wm^{-2} lower than the 2000 baseline, in line with the land-origin decrease. As with land-origin detrained cirrus, there is a decrease in the net CRE across all pressure bins of between -1Wm^{-2} and -4Wm^{-2} between 2000 and 2016.

This stark difference in the trend in the strongest bin relative to the weaker 3 bins is driven solely by the changes in the SW CRE, as shown in panel (f). Here, the change is much like panel (b), with the strongest bin cooling substantially more between 2006 and 2010 than the other bins. On the other hand, panel (d) shows the small variation in the LW CRE, where a trend is less clear. There are fluctuations in the strongest bin, with the LW CRE ranging between 2Wm^{-2} and -1Wm^{-2} relative to the baseline. The weaker 3 bins fluctuate between 0.5Wm^{-2} to -2Wm^{-2} relative to the baseline, with much closer agreement within years.

Overall, the variation in the ocean-origin detrained cirrus CRE-CTP sensitivity seen in Figure 5.12 is driven almost entirely by the spread in the SW CRE between the strongest CTP bin and the weaker 3 bins, as shown in Figure 5.11f.

This trend in the SW CRE across the study period is driven by variability in the timing of the strongest ocean convection, in contrast to fairly stable diurnal cycles for the weaker bins, and for land-origin detrained cirrus. Figure 5.13 shows the average diurnal cycle for the 'small SW CRE' years, that is the years 2005-2011, where there is a minima in the SW CRE for the strongest oceanic convection, and all other years. Panel (a) compares the diurnal cycle of the strongest oceanic convection for both of these

groups of years. It is clear that during the 2005-2011 low SW CRE minima, there is greater probability of the strongest oceanic convection occurring during the solar day, and a lower probability of it occurring at during the night, compared to the other years. This would explain the variation in the SW CRE, with the strongest detrained cirrus cooling more throughout it's lifetime, as it spends more of its evolution in the solar day. By contrast, Figure 5.13b shows the same plot as Figure 5.13a but for the weakest convective bin. Here, there is very little difference in the diurnal cycle between the two groups. This explains why there is little variation in the SW CRE of the weakest convective bin in Figure 5.12f).

Panel (c) shows the same as (a) but for land-origin convection. There is a smaller difference here between the two year groups, with the 2005-2011 diurnal cycle exhibiting a slightly greater probability of the strongest convection occurring during the day, and a slightly lower probability at night. This smaller contrast is reflected in panel (e) which shows a slight decrease in the SW CRE of the strongest convective bin, but much smaller than that of the strongest ocean convection. Again, panel (d) shows that in the weakest convective strength bin there is little difference in the diurnal cycle between the years, and as such little change in the SW CRE across the study period (Figure 5.12e). These results also show how important the timing of convection is to determining the lifetime CRE of the detrained cirrus. However, the question still remains as to why this change in the diurnal cycle of convection is seen over the study period, and why this change manifests almost exclusively for the strongest oceanic convection? It is interesting that this change occurs at a similar time to the 'global warming hiatus' (Medhaug et al., 2017) that occurred between 1998-2016. This was a period of relatively slow or no global warming as defined by a plateau in surface and tropospheric temperatures, upper ocean heat content, and sea surface temperatures (Easterling and Wehner, 2009; Meehl et al., 2011; Katsman and van Oldenborgh, 2011). The mechanisms that are thought to have contributed to the global warming

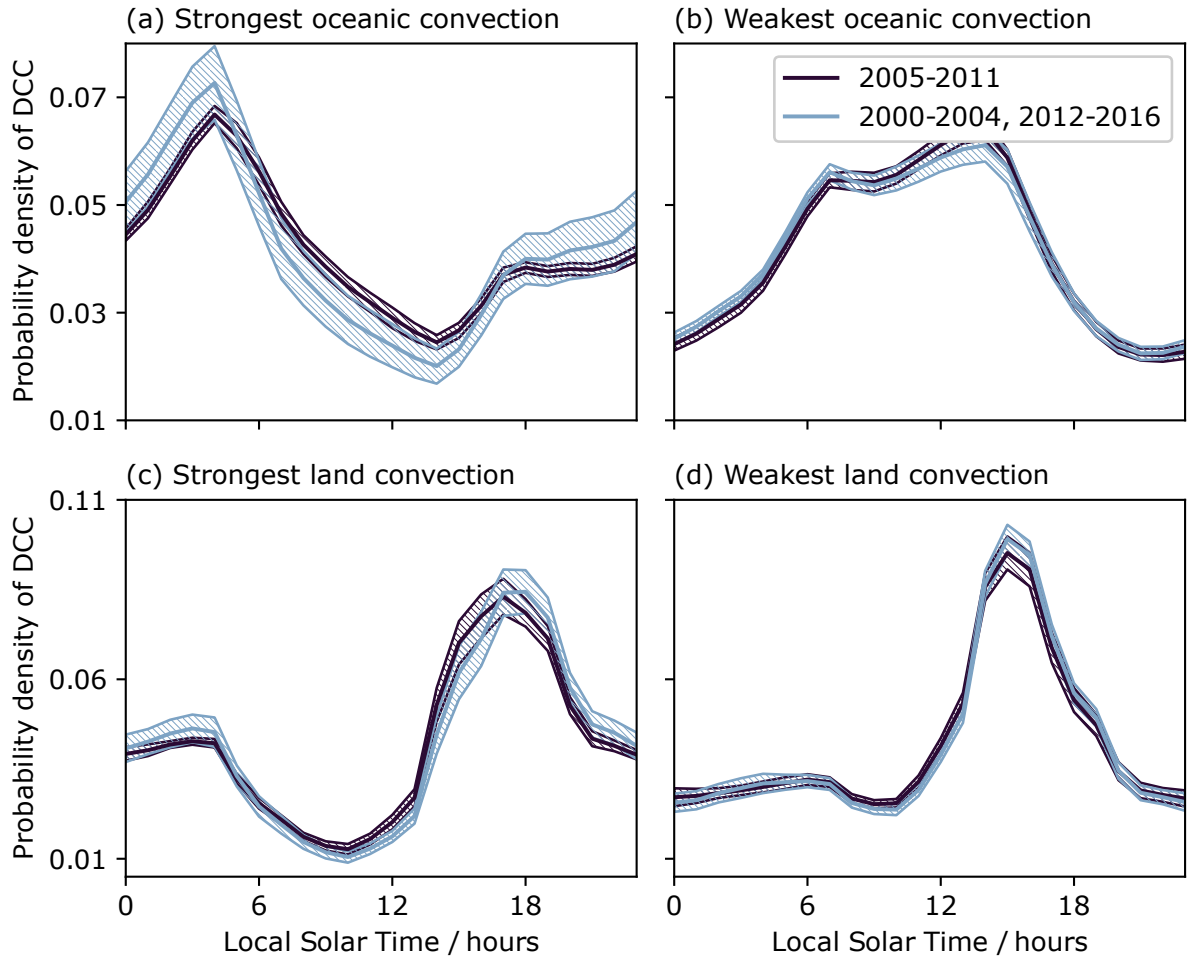


Figure 5.13: Diurnal cycle for low SW CRE years (2005-2011), and all other years. a) Strongest oceanic convection bin. b) Weakest oceanic convection bin. c) Strongest land convection bin. d) Weakest land convection bin

hiatus (hereafter GWH) are varied, from natural atmospheric variability (Kosaka and Xie, 2013), a reduction in radiative forcing due to stratospheric aerosol (Solomon et al., 2010), or related to the solar minimum in 2009 (Kaufmann et al., 2011). One source of natural variability that occurred during the GWH is a cooling of the eastern tropical Pacific relative to warmer periods after, characterised by a strongly negative PDO (Pacific Decadal Oscillation).

Given that the reduction in the net CRE is most pronounced in the strongest convective bin over the ocean and that it is driven exclusively by a reduction in the SW CRE, this points to changes in ocean characteristics impacting the development, and in particular

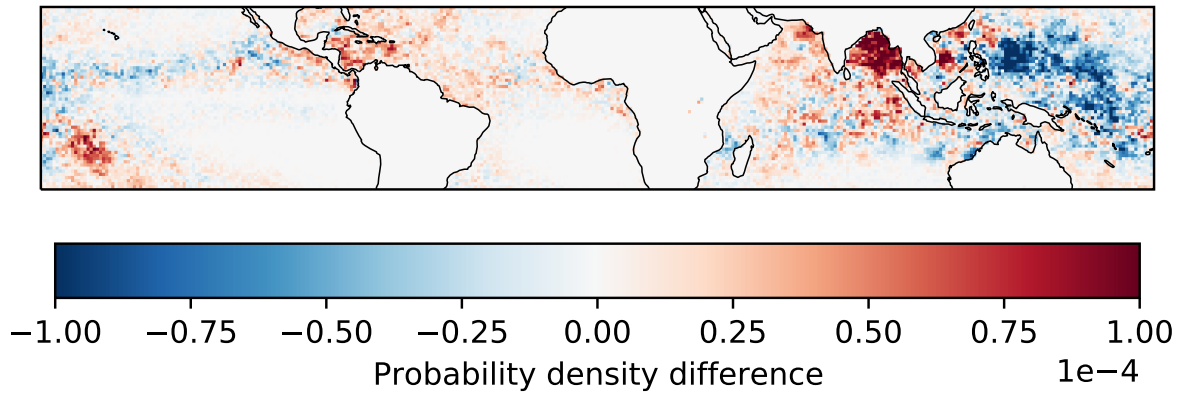


Figure 5.14: Difference in the mean normalised probability density of deep convection for 2005-2011 and the outer years of the study period. The distributions are normalised such that for each period the maps sum to one to account for the fact that there is a varying amount of absolute convection between the periods.

the timing or distribution, of the strongest oceanic convection. Figure 5.14 shows the difference in average distribution of the strongest convection between the 2005-2011 period and the period outside that. There is a significant increase in the probability of convection occurring over the Bay of Bengal and around Central America, and a decrease in the amount of convection occurring in the western Pacific. Recalling Figure 5.7c), convection over the Bay of Bengal and Central America occurs during the late morning, and the western Pacific convection occurs more often during the night. This shift in the distribution, and therefore timing, of the strongest difference explains the difference in the mean diurnal cycle from Figure 5.13a, which in turn explains the increase in the shortwave cooling during the 2005-2011 period, and the change in the CRE-CTP sensitivity.

More work is needed to investigate if the mechanisms associated with the GWH, in particular the strong negative PDO, have impacted the distribution of strong oceanic deep convection and how this impacts the CRE of the detrained cirrus. This future work would provide important constraints on the sensitivity of the detrained cirrus CRE to large-scale atmospheric variability and provide further evidence that the timing and distribution of convection plays a particularly important role in determining

the lifetime CRE of detrained cirrus. If the timing of strong deep convection, and thus lifetime CRE of detrained cirrus, is particularly sensitive to changes in ocean properties, this could have significant implications in a warming climate.

5.3.6 Sensitivity of CTP to AOD

The previous section of this chapter showed how the sensitivity of the CRE to CTP varies throughout the study period, and how the CRE-CTP relationship is sensitive to the timing of the convection, in particular to the strong oceanic convection. In this section, the average CRE-CTP sensitivity is used in an attempt to link a change in the CRE to a change in AOD, moderated through changes in the CTP.

Much like previous studies mentioned in the introduction of this chapter, a strong sensitivity is found between the CTP and the AOD for much of the globe. Figure 5.15a shows the sensitivity between the lnCTP and the AOD. There is a mostly negative relationship, particularly over the ocean, between the CTP and AOD, suggesting a decrease in the CTP (higher cloud tops) for an increasing AOD. This is strongest over oceanic regions of convection in the Maritime Continent and along the ITCZ. There is a positive relationship for some coastal regions, and notably off the west coast of Africa and around India and the Bay of Bengal. These results contrast to Gryspeerdt et al. (2014) who found stronger negative correlations between the MODIS CTP and AOD, with no positive regions. These differences are due to the differences in the CTP between ISCCP and MODIS, including the the fact that the ISCCP values are daily means and the MODIS values are instantaneous. However, they broadly agree on where the strongest negative sensitivity occurs.

The sensitivity of cloud top pressure of optically thick high clouds to the AOD is shown

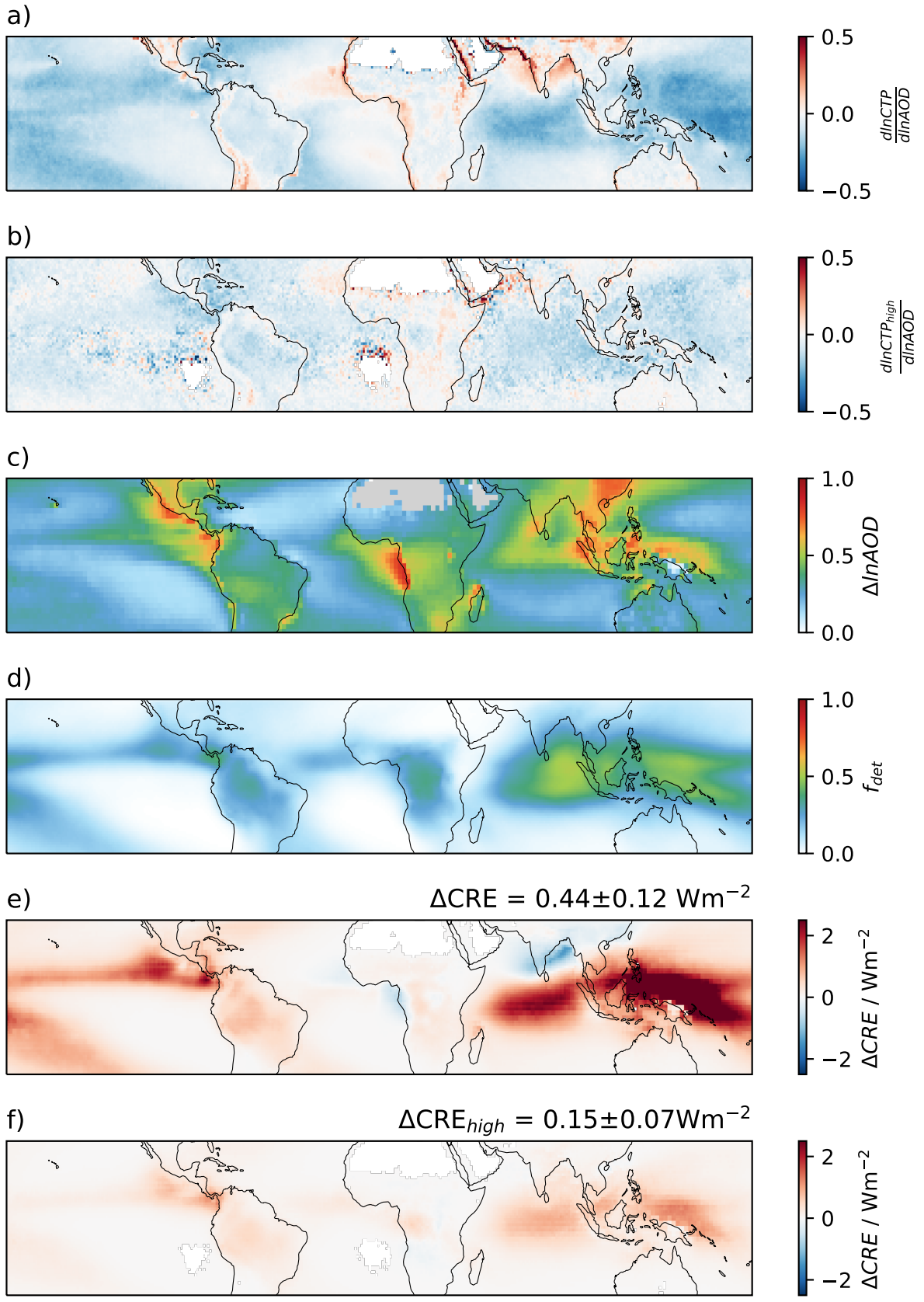


Figure 5.15: a) Sensitivity of the log of the cloud top pressure CTP to the log of the aerosol optical depth AOD. b) Same as a) for high cloud. c) A given change in the log of the AOD according to Bellouin et al. (2020). d) The f_{det} term, described in the methods section, which maps the dCRE/dCTP sensitivity to the detrained space. e) The change in the CRE for a given change in the AOD. f) Same as e) but for high cloud.

in Figure 5.15b. As in previous chapters the high clouds are isolated using only the thickest optical thickness bin and the top three cloud top height bins from the ISCCP τ-pc joint histograms. The sensitivity of the high CTP to AOD is much smaller than that of all CTP, naturally this is is the case due to the smaller range of high cloud top pressures. The sensitivity of the high CTP is more uniform than the all CTP across the tropics, indicating that high clouds have a similar sensitivity wherever they occur in the tropics. Contrast this to the sensitivity of the all cloud CTP, where the response varies depending on the cloud distribution. Interestingly, the one region where the sensitivity of high thick clouds is more negative than the sensitivity of all clouds is over South America, and a small region of central Africa. This indicate a strong negative relationship between the high cloud top pressure and the AOD in these regions.

Isolating the high cloud sensitivity from the all-cloud removes large regions of positive sensitivities, particularly over the Bay of Bengal, the Andes, and the west African Atlantic coast. These positive sensitivities are potentially due to retrieval errors where high MODIS AOD values are characterized as clouds in the ISCCP dataset. There are still some regions with a positive AOD-CTP relationship in Figure 5.15b, namely around the Sahara, throughout central Africa, and the coastal region around the Arabian Peninsula. These are likely due to a combination of noise (low number of high cloud retrievals), and a large AOD concentration causes the bias mentioned above.

The high cloud sensitivity has more noise due to the difficulty in colocating AOD retrievals and high CTP clouds, even when using daily mean values and the interpolated MODIS AOD product, regions of high thick clouds and retrieved aerosol optical depths. These results must be considered carefully, given that the influence of a retrieval bias towards less optically thick high clouds will be more impactful than on the all-cloud sensitivity due the smaller sample size.

5.3.7 Constraining changes in the detrained cirrus CRE with aerosol

Figure 5.15c shows the estimated change in the lnAOD from pre-industrial to present day from Bellouin et al. (2013). The largest increases in the AOD occur over China, in the Maritime Continent, off the west coast of central Africa, and along the west coast of Central America. Generally, the regions of large increases in the AOD collocate with regions of high CRE to AOD sensitivity, this is particularly true for the Maritime Continent.

By combining the above figures using Equation 5.4, an estimate for the change in the detrained cirrus CRE between pre-industrial and present AOD amounts is calculated and shown in panel (e) using the all cloud CTP sensitivity, panel (a), and panel (f) for the high cloud CTP sensitivity (panel (b)). The mean tropical ΔCRE is 0.44 ± 0.12 Wm^{-2} using the all cloud CTP sensitivity and 0.15 ± 0.07 Wm^{-2} using only the high cloud CTP sensitivity. In both the all cloud and high cloud sensitivity (panel (e) and (f)), the largest sensitivities occur over the Maritime Continent. The ΔCRE is largest over this region due to it being the most likely place to find detrained cirrus, combined with a large increase in the AOD (Figure 5.15c) in this region and a large negative AOD-CTP sensitivity (Figures 5.15a and b). There is a large sensitivity over the Amazon in both the all cloud and high cloud cases compared to central Africa. These contrasts are also due to a larger negative sensitivity of high CTP to AOD, reinforcing studies that have shown some evidence of potential aerosol invigoration over the Amazon (Andreae et al., 2004; Herbert and Stier, 2023).

As shown in Figure 5.10, there is a significant difference in the sensitivity of CRE to CTP for land-origin and ocean-origin detrained cirrus. It is therefore sensible to also calculate the change in the CRE for land and ocean-origin cirrus separately, using the two different sensitivities given in Figure 5.10.

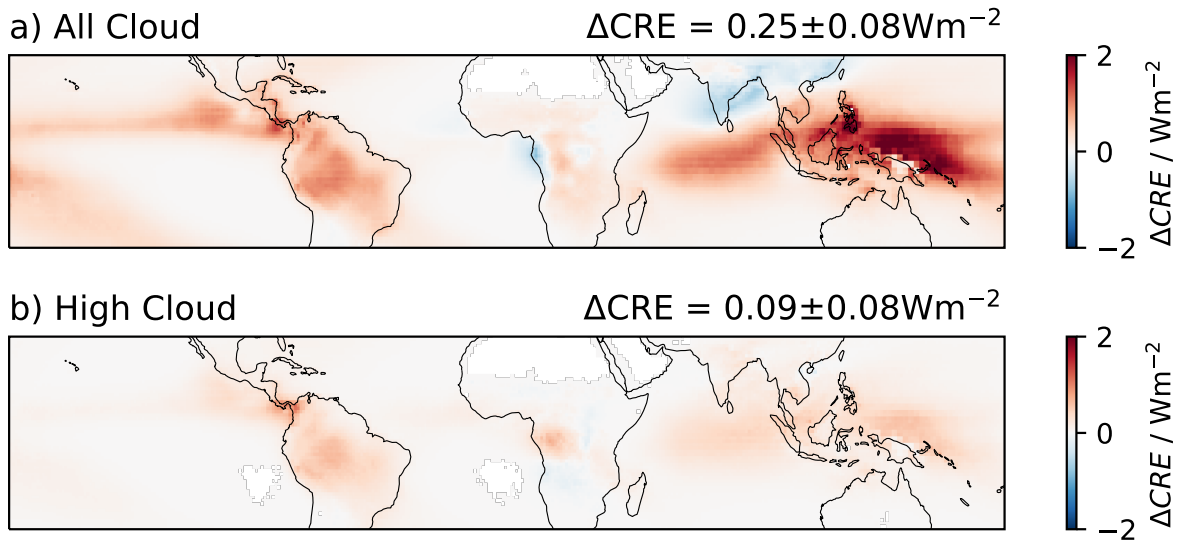


Figure 5.16: The change in the CRE for a given aerosol change, as for Figure 5.15e) and f), but using the separate land and ocean CRE-CTP sensitivity values from Figure 5.10b) and c). Note the scale on panel (b) is half that of panel (a).

Figures 5.16a,b show the same as Figures 5.15e,f, but using separate sensitivities over land and ocean. Using these sensitivities, -0.25Wm^{-2}hPa^{-1} for land-origin detrained cirrus and -0.10Wm^{-2}hPa^{-1} for ocean-origin detrained cirrus, rather than the all-origin sensitivity (-0.17Wm^{-2}hPa^{-1}), the change in the CRE given a change in aerosol is found to be smaller. Using the all cloud AOD-CTP sensitivity the tropical ΔCRE is 0.25 ± 0.08 Wm^{-2}, whereas the high cloud AOD-CTP gives a tropical ΔCRE of 0.09 ± 0.08 Wm^{-2}. This is a reduction of 44% and 40% respectively.

The reduction in ΔCRE is driven by the reduction in the sensitivity of CRE-CTP over ocean, in particular over the Maritime Continent, where the majority of the convection occurs. By contrast, the CRE over land is higher due to the larger land-origin sensitivity compared to the global mean. This means that the mean contribution to the tropical CRE is similar for both ocean and land compared to in Figures 5.15e,f. These plots, and this chapter more generally, highlight the importance of considering land-ocean convection separately, given their contrasting properties sensitivities to changes in both CTP and AOD.

5.4 Discussion

This chapter has shown that the lifetime CRE of detrained cirrus is heavily dependent on the initial strength of the convection from which it originated. There are strong regional differences in where the differing strength convection occurs, with large land versus ocean contrasts. The differences in the lifetime CRE of detrained cirrus originating from convection of varying strength are predominantly driven by changes in the SW CRE, which in turn is driven by the timing of the initial convection. This CRE-CTP sensitivity is then combined with a calculated all-cloud and high-cloud AOD-CTP sensitivity to derive a a value for the change in CRE for a change in AOD from pre-industrial to present day. These two sensitivities are combined in a novel equation that links the local change in the properties of the convection (AOD-CTP sensitivity), to the non-local change in the detrained cirrus induced by a change in the properties of the convection (CRE-CTP sensitivity). Whilst this chapter arrives at a value for the change in the CRE that is within the range already given in the literature (Christensen et al., 2014), there are uncertainties present that should be addressed.

One source of uncertainty arises when calculating the CRE-CTP sensitivity. The TSC algorithm works better when fewer distinct convective strength bins exist, given that a necessary amount of interpolation occurs, and any averaging between bins will change the flag value. This is why binning is necessary, and each convective event cannot be assigned its actual cloud top pressure as its flag value. However, having only four bins means that fitting a straight line and assigning a sensitivity could potentially miss out on any non-linearity within each bin and over-confidently predict a linear relationship. This is a necessary trade-off to account for the uncertainty of the interpolation in the TSC algorithm. There is no clear alternative, within the confines of the TSC algorithm, to calculating the sensitivity in this way, but it might explain the very high r-values calculated in Figure 5.10.

This chapter assumes that the AOD-CTP sensitivity calculated is likely an upper bound on the true sensitivity. Gryspeerdt et al. (2014) demonstrated that much of the observed AOD-CTP sensitivity can be reconstructed through the CTP-CF-AOD relationship, suggesting that aerosol invigoration may not be the cause. This conclusion applies to the all-cloud AOD-CTP relationship. In contrast, the same analysis was not performed for high-cloud AOD-CTP, however there is no reason to suggest that the same reconstruction would not be possible.

For high-cloud AOD-CTP, there are limitations because it is not always possible to simultaneously retrieve collocated high optically thick clouds and aerosols. As a result, the data tends to favour collocating only the thinner high clouds and aerosols, which may lead to underestimating the observed sensitivity. This, combined with the fact that the statistics used to calculate the regression for the CRE-CTP sensitivity have artificially limited variability (only four bins), means that the final retrieved CRE-AOD sensitivity for all clouds is likely an upper bound, while the sensitivity for high clouds is likely a lower bound, suggesting that the actual sensitivity falls between these two values.

The value for the change in the AOD is taken from Bellouin et al. (2013). The present day AOD can be measured, but the pre-industrial is estimated, leading to some uncertainty in the change in AOD from pre-industrial to present day. The Bellouin et al. (2013) estimate of a change between 0.02 and 0.04 is supported by reanalysis and large scale modelling, however there are of course uncertainties associated with these estimates, and using other estimates would yield different results for our change in high cloud CRE. For example, the estimate from McCoy et al. (2017) is larger than Bellouin et al. (2020).

Whilst there are uncertainties with the terms used in Equation 5.4, it still provides a useful theoretical framework for approaching the problem of reconciling local changes

in cloud properties to non-local ones, through the mapping f_{det} term.

5.5 Conclusion

This chapter has built on the work of the previous two chapters by expanding the TSC methodology to include a flag that bins by convective strength and tracks this convective origin, the bins are shown in Figure 5.4. It was found that the regional distribution of convection varies depending on the strength of convection, with stronger convection occurring more readily over central Africa and continental Asia than the Maritime Continent (Figure 5.5).

The diurnal cycle of convection was also found to vary with convective strength, with distinct variations for land and ocean convection (Figure 5.6). It was found that for land-origin convection, stronger convection occurred slightly later in the afternoon, and more readily at night than weaker convection. For ocean, the difference in diurnal cycles was larger for convection of different strength, with the strongest convection occurring in the early morning before sunrise and throughout the night. In contrast, weaker oceanic convection occurred more steadily throughout the day. This was shown clearly in Figure 5.7, which showed the contrast in the peak time of convection for weak and strong convection.

The impact that the timing of convection had on the radiative evolution of the detrained cirrus was also investigated, and it was found that there were very large differences in the SW CRE evolution depending on the location and timing of the initial convection (Figure 5.8c,f,i). In contrast, the LW CRE was shown not to vary as much with convective strength. This highlights that most of the changes seen in the CRE of detrained cirrus with convective strength are due to changes in the diurnal cycle

(Figure 5.9).

These results enabled an investigation into how the convective strength of the deep convection impacts the lifetime CRE of detrained cirrus clouds (Figure 5.10). This chapter found significant contrasts in the lifetime CRE of detrained cirrus clouds from strong versus weak convection, which as previously shown, are driven mostly by changes in the SW CRE due to the timing of the convection. The CRE-CTP sensitivity is found to be -0.17$Wm^{-2}hPa^{-1}$. This sensitivity is stronger for land-origin convection, at -0.24$Wm^{-2}hPa^{-1}$, than for ocean-origin convection, at -0.10$Wm^{-2}hPa^{-1}$.

The sensitivity is almost constant over the study period for land-origin cirrus; however, it varies significantly for ocean-origin cirrus, ranging between -0.16$Wm^{-2}hPa^{-1}$ and -0.03$Wm^{-2}hPa^{-1}$ (Figure 5.11). The weak sensitivity period occurs between 2005-2011, and is driven by a decrease in the SW CRE of cirrus from the strongest convective bin. It is found that this decrease in the lifetime SW CRE between 2005-2011 is driven by changes in the diurnal cycle, with stronger convection occurring more readily during the day and less often at night compared to the rest of the study period (Figure 5.13). This, in turn, is driven by changes in the distribution of the convection, as shown in Figure 5.5, with stronger convection occurring more in the Bay of Bengal and the ocean around Central America (which tends to occur later into the day, and so has a weaker SW cooling), and less convection occurring in the western Pacific, where convection usually occurs during the very early morning. These changes may be linked to the global warming 'hiatus' period, and potentially the strongly negative PDO that occured during the middle of this period, however much more work is needed to test this hypothesis.

The CRE-CTP relationship is then linked to a retrieved AOD-CTP sensitivity for both all cloud CTP and high cloud only CTP (Figure 5.15), in order to calculate an estimate for a detrained cirrus CRE-AOD relationship. As the detrained cirrus is advected away

from the location of the original convection, a method is developed to map the non-local (CRE-CTP) sensitivity to a local (AOD-CTP) sensitivity (schematic of which is shown in Figure 5.2), where a change in the properties at the source of the deep convection is connected to a change in the properties of cirrus that flow from the deep convection, a novel equation is developed that introduces a mapping term, f_{det}, that links the two sensitivities. The global change, estimated to be half the tropical change, in the detrained cirrus lifetime CRE due to aerosol changes from pre-industrial to present day is found to be between +0.3 Wm^{-2} to 0.0 Wm^{-2}.

This chapter has shown that the detrained cirrus lifetime CRE is very sensitive to the strength of convection. This pathway is via changes in the diurnal cycle for convection of different strength, impacting the SW CRE evolution of detrained cirrus, which thus impacts the lifetime CRE. There are smaller changes in the LW CRE due to the altitude at which the detrained cirrus flow out. However, more work is needed to investigate the LW response. This chapter builds on work in the previous chapter to show the importance that the timing of the initial convection has in determining the CRE of the detrained cirrus, and the impact that a change in the distribution of convection has on this response. This chapter has also introduced a novel attempt at reconciling local sensitivities to non-local sensitivities and therefore been able to bound estimates of the sensitivity of detrained cirrus lifetime CRE to the aerosol concentration at the location of the initial convection. Further applications of this novel approach will be discussed in the thesis conclusion.

Chapter 6

Conclusion

Tropical deep convection plays a vital role in modulating the energy balance of the atmosphere, transporting large amounts of water and energy out of the tropics to higher latitudes. Regions in areas of active tropical convection have a net CRE close to zero. This net CRE is the sum of a large SW cooling from optically thick deep convective cores and their anvils and a large LW warming from ubiquitous thin cirrus arising out of deep convection that cover large areas of the tropics. It follows, therefore, that any small percentage change in the LW or SW components of deep convection or detrained cirrus in the tropics, be this due to changes in microphysical or spatiotemporal properties of these clouds, could have potentially very large impacts of the net CRE of the tropics.

The processes that govern the properties of deep convection and the evolution of detrained cirrus are not well constrained, leading to poor representation and development of deep convection and tropical cirrus in our current climate models. This is particularly true when it comes to the distribution of convection and the timing of its initiation. The impact that the timing and distribution of deep convection has on the

radiative evolution of detrained cirrus is also poorly understood. This thesis has improved our understanding of how sensitive detrained cirrus are to initial conditions and timing of deep convection, and as such highlighted the importance of improving model representation of deep convection.

The interaction between aerosols and deep convection is also poorly understood and notoriously difficult to observe. In particular, there is much uncertainty regarding the impact that aerosols have on the cloud radiative effect of deep convection and detrained cirrus. This is due to the difficulty posed when attempting to simultaneously observe aerosols and deep convection, or other cloud properties such as CCN, in satellite data (Koren et al., 2005; Stier, 2016; Veals et al., 2022), and the difficulty of controlling for meteorological factors that would allow for robust causal studies (Boucher and Quaas, 2013). This is so much so the case that recent studies bounding the radiative forcing from aerosol-cloud interaction do not attempt to include any estimate for the radiative forcing that arises from aerosol-deep convection interactions (Bellouin et al., 2020).

Previous work investigating the impact of aerosols on deep convection have also often been regionally limited, and have relied on proxies for aerosol concentration where retrievals of aerosols are not available at the locations of deep convection. More importantly, they have also often limited their studies to the impact that aerosols may have on the deep convection, and not the subsequent detrained cirrus clouds that evolve out of them. It is clear that, whilst the impact that aerosols have on the deep convection is important, the entire lifecycle of the deep convective system must be considered to understand the full impact that aerosols may have on the radiative effect of deep convective cores and detrained cirrus clouds. This thesis helps tackle this issue by introducing a novel methodology that links the local change in the properties of deep convection that is correlated to aerosol concentration, to the non-local impact that

these changes have on the radiative impact of detrained cirrus clouds. This non-local approach, combined with the novel tracking methodology introduced in this thesis, has applications, beyond just deep convection studies, which will be discussed in the future work section of this chapter.

6.1 Conclusion

Chapter 3 of this thesis introduced the novel 'time since convection' tracking methodology used to investigate the evolution of air parcels flowing from deep convection. As mentioned above, this method improved on previous studies that track individual convective events. By tracking all air parcels from all convective events identified in the geostationary data, whilst remaining computationally efficient, this allowed for a composite study into the evolution of detrained cirrus clouds from all tropical convection that was unbiased in space and time.

The deep convective cores were identified in 1x1 degree ISCCP-H data at a 3 hourly resolution. The convective cores were identified using a nearest neighbour algorithm that sorted each pixel into a different cloud regime. Once convective cores were identified they were advected forward in time using an ERA5 wind field between 200-300hPa. At each time step the time since convection (TSC) value was increased by one hour at all locations in the tropics. Where convection occurred, the TSC value was reset back to zero.

The TSC dataset was evaluated against individual HYSPLIT trajectories to assess its performance. The TSC dataset was accurate, insofar as it matched the trajectories from HYSPLIT, for the entire lifetime of detrained cirrus clouds. It was also shown that TSC is independent of latitude. That is to say, for a given TSC bin, the zonally averaged

cloud amount was the same across all tropical latitudes. For example, the vertically resolved cloud amount at 6 hours from convection did not look significantly different at 0N as it did at 25N. This was an important results, as it showed that looking at cloud evolution as a function of TSC wasn't simply showing the evolution of air parcels as they moved from the centre of the tropics out to the extra-tropics.

Cloud properties were shown to be a very strong function of TSC, in particular for high clouds. After a sharp initial decay in the cloud optical thickness and vertically resolved cloud fraction associated with the dissipated of the deep convective core, changes in the cloud properties of the detrained cirrus cloud were observed throughout their lifetimes. Cloud properties were also shown to change after the detrained cirrus had dissipated, showing changes in the in situ cirrus cloud properties as a function of TSC up to 120 hours after the initial convection had dissipated. Gradual thinning of the detrained anvil is seen in the vertically resolved cloud amount from DARDAR, as expected from previous studies on anvil evolution.

The changes in these cloud properties explain the observed evolution of the tropical high cloud CRE as a function of TSC. After a large initial net cooling from the deep convective cores and thick anvils, made up of a very large SW cooling and LW warming, the net high cloud CRE becomes warming, maintaining this warming at all further TSC values, albeit reducing towards zero as the detrained cirrus thin. This warming effect is not seen when including low clouds, which exert a continuous large SW cooling at all TSC values. This highlights the importance of isolating just the high cloud CRE to obtain a clear picture of the radiative evolution of deep convection and detrained cirrus in the tropics. At all TSC values, the net CRE is made up of larger SW and LW values. Understanding the controls on high cloud evolution as a function of TSC is essential to constrain the processes governing the tropical radiation balance. This chapter showed the merits of this novel TSC tracking methodology. Previous studies

which tracked individual convective cores and anvil cirrus often underestimated the warming across the lifetime, as they stopped tracking when the detrained cirrus optical thickness dropped below a certain value. This meant that many results did not include very thin cirrus which couldn't be tracked in traditional methods, which have a large impact on the overall tropical CRE.

After introducing the novel TSC methodology in Chapter 3 and evaluating its methods, Chapter 4 further advanced the methodology by first investigating how the origin of the deep convection, namely whether it occurred over land or ocean, impacted the radiative evolution of the air parcels from deep convection. The lifetime of detrained cirrus from deep convection was also measured, and the impact that detrained cirrus lifetime had on the radiative effect of tropical high clouds was investigated.

Land and ocean origin air parcels were tracked by assigning a flag value to each convective event depending on where it occurred. This flag value was then advected forward with the air parcels along with the TSC and whether the air parcel contained a detrained cirrus cloud or not. The detrained cirrus cloud was determined to have dissipated when the cloud fraction along a trajectory first dropped below 10%. The TSC methodology had three unique tracking flags incorporated into it; 1) a TSC flag which is dynamic and changes at each timestep, 2) a land-ocean origin flag that does not change along trajectories that denotes the specific conditions of convection as it occurred, 3) a binary detrained/not detrained cirrus flag that changes according to the specific conditions along the trajectory, and does not change again after. These three methods highlight the flexibility of the TSC tracking approach, and the ease with which new flags can be introduced into the methodology to answer different questions.

After introducing the new aspects of the TSC methodology, the impact of land-ocean origin was investigated. It was found that air from land-origin convection often exists over the ocean, and vice versa. This shows that analysis of the impact that convective

origins have on detrained cirrus is not simply the case of applying a land-ocean mask and investigating the evolution of air parcels within each mask.

It was shown that the radiative evolution of air parcels along trajectories from convective were substantially different depending on whether the the convection occurred over land or ocean. The radiative evolution of land-origin air parcels were found to be warming for all TSC values, starting with a higher warming before flattening towards zero at high TSC values. By contrast, the ocean-origin detrained cirrus displayed a similar cooling-to-warming-to-zero CRE pattern observed in the previous chapter. The differences in the net CRE were found to be driven predominantly by differences in the SW CRE. This SW CRE contrast is due to the timing of the initial convection being significantly different for ocean and land convection, and the impact of differences in surface albedo between land and ocean. The influence that the diurnal cycle has on the SW radiative evolution of air parcels from deep convection was found to be considerably larger than any difference in the LW CRE. The all-origin tropical high cloud lifetime CRE was found to be 5.0 ± 0.4 Wm^{-2}. The land-origin and ocean-origin high cloud lifetime CRE were found to be 7.7 ± 0.6 Wm^{-2} and 4.4 ± 0.4 Wm^{-2}, respectively. As mentioned above, these differences are predominantly due to differences in the SW CRE due to the timing of the initial convection.

The lifetime of land and ocean origin detrained cirrus were also found to differ, with land-origin detrained cirrus have a shorter lifetime than ocean-origin detrained cirrus (modal lifetime of 15 hours versus 30 hours, respectively.) These results suggest that land origin detrained cirrus, which originate just before night and persist throughout the night, are subjected to conditions that shorten their lifetime, such as entrainment of dry air, compared to their ocean origin counterparts. These results support findings in previous modelling work that suggests anvil cirrus decay quicker in the night than during the day. These are important results that show another pathway through which

the diurnal cycle of convection impacts the lifetime CRE of detrained cirrus, beyond just their altered SW CRE.

The second half of Chapter 4 explored the impact that changes to the lifetime of detrained cirrus had on the total high cloud CRE in the tropics. By modelling the lifetime of detrained cirrus as a distribution along TSC, and altering this distribution, the lifetime of detrained cirrus could be extended by any defined amount. The total high cloud CRE in the tropics is calculated as the weighted average of both the detrained cirrus CRE, and the in-situ air parcel CRE - that is the CRE of clouds in gridboxes with a detrained flag, and the CRE of air parcels in gridboxes without. The detrained cirrus distribution was extended at the expense of the in situ distribution, and the new CRE was calculated with this extended distribution. The lifetime high cloud CRE was then calculate for each percentage extension of the detrained cirrus lifetime, and the change in CRE was calculated. It was found that extending the lifetime of the detrained cirrus by 100% increased the all-origin high cloud CRE by 0.7 ± 0.1 Wm^{-2} for the tropics. For land-origin and ocean-origin detrained cirrus this extension lead to a 2.0 ± 0.1 Wm^{-2} and 0.3 ± 0.1 Wm^{-2} increase in the lifetime CRE, respectively. This land-ocean contrast in the increased warming is due to the fact that the detrained cirrus are warming at all points in their lifetime, compared to ocean-origin detrained cirrus, and as such any extension to their lifetime increases the warming by a larger degree.

Chapter 4 showed that changes in the detrained cirrus lifetime have an impact on the overall high cloud CRE in the tropics, however this impact is found to be relatively small. More work is needed to put these lifetime adjustments into context regarding mechanisms that are proposed to change the lifetime of detrained cirrus, such as changes in the timing of convection or aerosol invigoration. This chapter has provided an important constraint to these estimates, putting an upper bound on the impact that a doubling in the lifetime of detrained cirrus may have on the tropical high cloud CRE.

The first two chapters laid the groundwork for the final chapter of this thesis. Extending the TSC methodology even further, Chapter 5 introduces a cloud top pressure (CTP) flag that separates every convective event into four distinct CTP bins in order to investigate how the initial strength of convection (here using CTP as a proxy for convective strength), impacts the radiative evolution of the detrained cirrus clouds.

This thesis finds a strong linear relationship between the initial CTP of the deep convection, and the detrained cirrus net CRE. The lower the initial CTP (higher cloud tops), the more warming the detrained cirrus are throughout their lifetime. This is true for both land-origin and ocean-origin detrained cirrus, however there is a much stronger relationship for land-origin than ocean-origin detrained cirrus. The sensitivity of CRE to CTP is -0.17$Wm^{-2}hPa^{-1}$ for all-origin detrained cirrus, and -0.24$Wm^{-2}hPa^{-1}$ and -0.10$Wm^{-2}hPa^{-1}$ for land-origin and ocean-origin, respectively. These novel results show that it is vital to consider the behaviour of detrained cirrus that originate from land separately to those that originate from ocean, and once again shows that the timing of convection plays an integral role in determining the lifetime CRE of detrained cirrus, since the sensitivity of CRE to CTP is predominantly due to differences in the diurnal cycle of convection of differing initial strength.

The variation in the CRE-CTP sensitivity over the study period from 2000-2017 was also investigated in this chapter, finding that there was significant variability in the ocean-origin detrained cirrus sensitivity compared to the land-origin sensitivity. It was found that most of the variability in the sensitivity was due to variability in the SW cooling of detrained cirrus from the strongest convection. This, in turn, was thought to be caused by variability in the diurnal cycle throughout this study period, however more work is needed to verify this. Whilst it is not clear what caused this variability, beyond a changing distribution of the strongest convection, it shows just how sensitive the lifetime CRE of detrained cirrus is to the location and timing of convection, indi-

cating the importance of representing these variables well in climate models if we are to understand how the impact of them changing in the future might have on the cloud radiative effect in the tropics.

The final aim of the thesis, achieved in Chapter 5, was to link the observed sensitivity of detrained cirrus CRE to initial strength (CTP) of the deep convective cores, to an observed sensitivity of high cloud CTP to aerosol concentration, in an attempt to bound potential aerosol impacts on the detrained cirrus lifetime CRE. In order to do this, a novel equation was introduced that linked the non-local impact of detrained cirrus CRE to the local change in CTP due to aerosols. This enabled the calculation of a bound on the aerosol impact on detrained cirrus CRE, but also introduced a framework for more generally matching non-local impacts to local changes in cloud properties. The global change in the detrained cirrus lifetime CRE correlated to aerosol changes from pre-industrial to present day was found to be between +0.3 and 0.0Wm^{-2}. This final chapter has a wide range of applications beyond the work presented in this thesis, and represents an important development in our ability to attribute non-local impacts of local changes.

6.2 Summary

This thesis has introduced a novel method to investigate the evolution of deep convection, in particular the radiative impacts of the detrained cirrus that flow from convective cores. The impact that the initial conditions of the deep convection have on the subsequent evolution of detrained cirrus is shown to be large. The distribution and timing of the initial convection has shown to be particularly important in determining the mean CRE of detrained cirrus across their entire lifetime. Changes in the lifetime of detrained cirrus are shown to impact the overall tropical CRE; however, this impact

is small relative to the changes in the initial conditions mentioned above. Finally, the detrained cirrus CRE is shown to be sensitive to the initial strength of convection via the CTP, with stronger convection leading to warmer detrained cirrus. The high cloud CTP is shown to be sensitive to the aerosol concentration, even though this may be due to meteorological covariations, and these two terms are linked using a novel equation that uses the Lagrangian trajectories to calculate the sensitivity between aerosol concentration (local) and detrained cirrus CRE (non-local).

6.3 Future Work

There are several avenues of potential future research to explore leading on from the work done in this thesis.

6.3.1 Representation of deep convection in climate models

Climate models struggle to accurately represent deep convection, both through the difficulty they have in distributing it accurately across the tropics, and in initiating convection at the correct time of day. This thesis has shown that both of these factors, the distribution and the timing of convection, have a huge impact on the subsequent evolution of the detrained cirrus, both in terms of lifetime and radiative effect.

In future work, it would be useful to apply the TSC methodology using model output, such as ECHAM, and to make comparative studies between observations and models, evaluating the impact of poor model representation of deep convection on the detrained cirrus development. Understanding where models poorly perform regarding deep convection, and the impact that this has on the subsequent anvil evolution will

be important for motivating improvements for future model representation of deep convection.

State-of-the-art high-resolution storm-resolving models are also beginning to become more widely used. The comparative study into the representation of deep convection in model output could be continued by implementing the TSC methodology into these high-resolution models to see how the improved representation of deep convection impacts the evolution of detrained cirrus. This would further help us understand how the distribution and timing of convection impacts the cloud radiative effect of detrained cirrus in the tropics. The distribution of convection of different strengths through cloud top pressure would also make a useful comparative study.

It would also be useful to investigate the impact of initial convective conditions on the evolution of other cloud microphysical processes readily available in climate models. As done in previous work, it would be useful to investigate how ice properties of the detrained cirrus evolve as a function of TSC. These properties all impact cloud lifetimes and cloud radiative effects, so understanding better how these properties evolve with time and how sensitive they are to their initial conditions will help improve understanding of detrained cirrus evolution.

6.3.2 The impact of convective strength on other observed cloud properties

This thesis has focused mostly, although not exclusively, on the radiative evolution of detrained cirrus and how macrophysical properties of the convection impact this evolution. It has been shown that the timing and distribution of convection play a key role in determining the SW CRE of detrained cirrus as a function of TSC. However, there is

still more work to be done to investigate how the initial conditions of deep convection impact the microphysical evolution of the detrained cirrus and what impact this has on radiative evolution. Not only will this help improve understanding of detrained evolution, but it could help better understand causal chains of interaction between cloud properties, and what impact this has on cloud lifetime and related feedbacks. One question, for example, is how does the evolution of cloud optical thickness of detrained cirrus vary depending on the convective strength? Using DARDAR, it would be useful to see how the ice microphysical properties vary in detrained cirrus of different convective strength origin. Whilst we might expect these differences to have a smaller impact on the overall lifetime net CRE than changes in timing and distribution of deep convection, knowing exactly what impact microphysical differences have on the CRE will be vital for our understanding of how the radiative effect of detrained cirrus could change in the future. It will also aid in understanding the contrast between cloud lifetimes and their controls.

6.3.3 Quantifying non-local impacts of local changes

The final section of this thesis introduced a novel method for linking local changes in cloud properties (in this case changes in the cloud top pressure of deep convection with aerosol), to non-local changes (the lifetime CRE of detrained cirrus that flow out of convection). This is just one application of such an approach. Quantifying these non-local impacts has value to many areas of work, and the novel equation introduced in Chapter 5, along with a semi-Lagrangian 'time since...' methodology, can be reworked to answer some of these questions.

One example of a potential area for work using this approach is in the field of geo-engineering, in particular marine cloud brightening and cirrus cloud thinning. Marine

cloud brightening involves increasing the number droplet concentration in shallow stratocumulus cloud decks in order to increase the albedo and reflect sunlight back to place. Cirrus cloud thinning involves seeding cirrus clouds with INP that increases the ice crystal size and encourages deposition, thinning the remaining cloud. Current work in this field focuses on the instantaneous, or short time scale, changes in the cloud properties at times after an aerosol perturbation. However, there are concerns about non-local changes in cloud properties at locations far away from, and at times long after, the initial cloud perturbation. Using a Langrangian framework that tracks air parcels from ship tracks, and the novel equation introduced in this thesis, it would be possible to try to quantify the non-local impact that could occur due to marine cloud brightening. Another application could be for contrail studies. Quantifying the impact that contrails may have on, for example, the development of cirrus clouds at long times after the initial contrail outbreak would also be possible with this approach.

Appendix A

Chapter 4 Supplementary

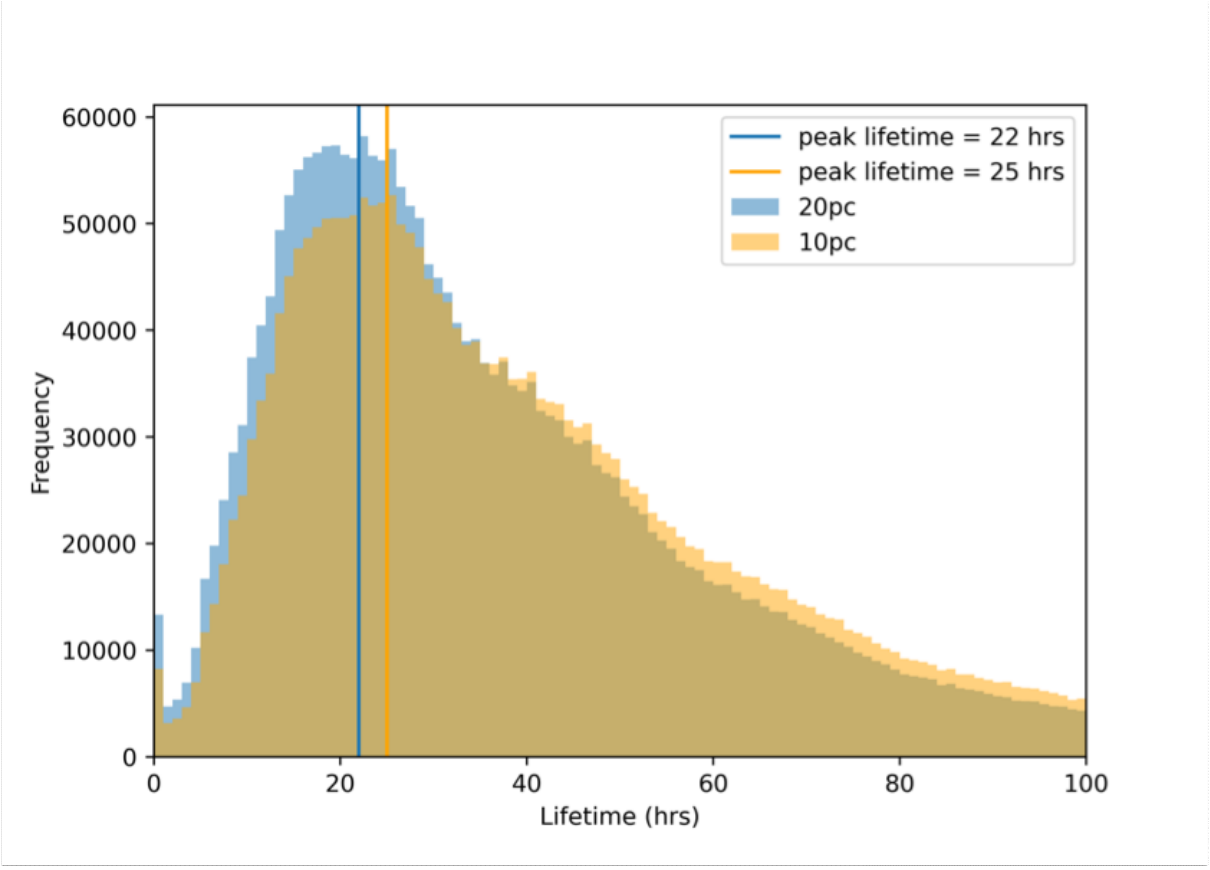


Figure A.1: Histogram of the lifetimes of detrained cirrus using a 20% threshold and a 10% threshold for the lifetime cutoff point.

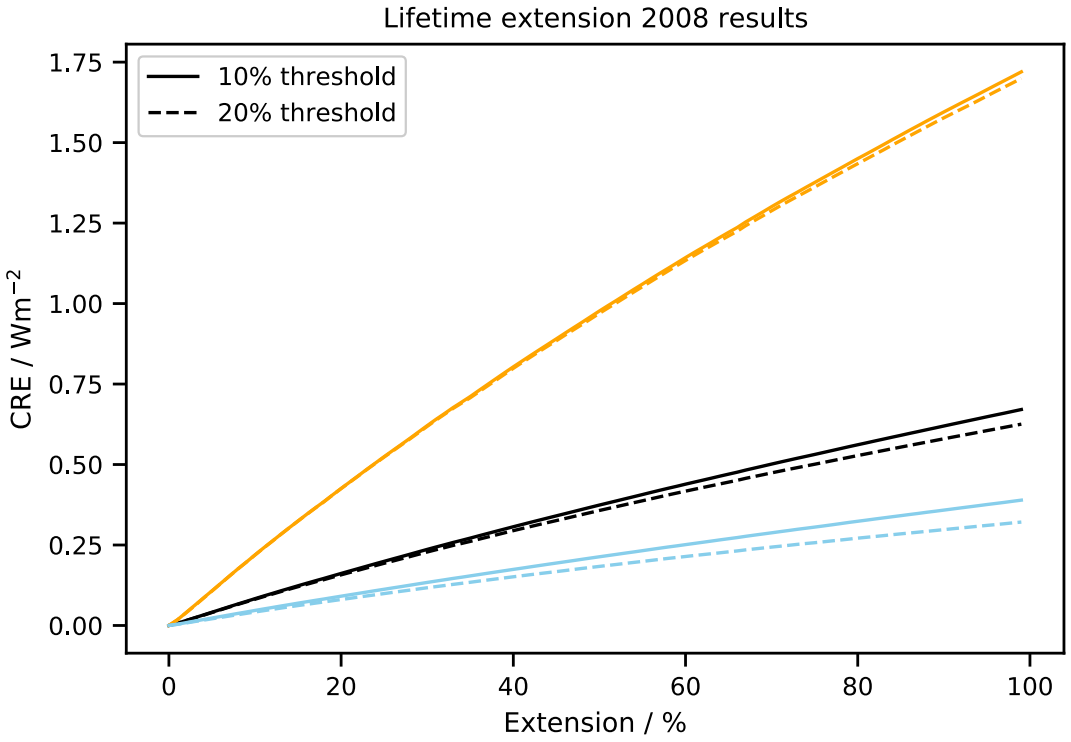


Figure A.2: Change in the lifetime extension CRE using the two different calculated cutoffs from Figure A.1.

Bibliography

Abbott, T. H. and Cronin, T. W.: Aerosol invigoration of atmospheric convection through increases in humidity, Science, 371, 83–85, https://doi.org/10.1126/science.abc5181, 2021.

Ackerman, A. S., Kirkpatrick, M. P., Stevens, D. E., and Toon, O. B.: The impact of humidity above stratiform clouds on indirect aerosol climate forcing, Nature, 432, 1014–1017, https://doi.org/10.1038/nature03174, 2004.

Adler, R. F. and Negri, A. J.: A Satellite Infrared Technique to Estimate Tropical Convective and Stratiform Rainfall, Journal of Applied Meteorology and Climatology, 27, 30 – 51, https://doi.org/10.1175/1520-0450(1988)027¡0030:ASITTE¿2.0.CO;2, 1988.

Aitken, J.: 1. On Dust, Fogs, and Clouds, Proceedings of the Royal Society of Edinburgh, 11, 14–18, https://doi.org/10.1017/S0370164600046666, 1882.

Albrecht, B. A.: Aerosols, Cloud Microphysics, and Fractional Cloudiness, Science, 245, 1227–1230, https://doi.org/10.1126/science.245.4923.1227, 1989.

Albright, M. D., Recker, E. E., Reed, R. J., and Dang, R.: The diurnal variation of deep convection and inferred precipitation in the central tropical Pacific during January–February 1979, Monthly weather review, 113, 1663–1680, 1985.

Andreae, M. and Rosenfeld, D.: Aerosol cloud precipitation interactions. Part 1. The nature and sources of cloud-active aerosols, Earth-Science Reviews, 89, 13–41, https://doi.org/10.1016/j.earscirev.2008.03.001, 2008.

Andreae, M. O., Rosenfeld, D., Artaxo, P., Costa, A. A., Frank, G. P., Longo, K. M., and Silva-Dias, M. A. F.: Smoking Rain Clouds over the Amazon, Science, 303, 1337–1342, https://doi.org/10.1126/science.1092779, 2004.

Bellouin, N., Quaas, J., Morcrette, J.-J., and Boucher, O.: Estimates of aerosol radiative forcing from the MACC re-analysis, Atmospheric Chemistry and Physics, 13, 2045–2062, https://doi.org/10.5194/acp-13-2045-2013, 2013.

Bellouin, N., Quaas, J., Gryspeerdt, E., Kinne, S., Stier, P., Watson-Parris, D., Boucher, O., Carslaw, K. S., Christensen, M., Daniau, A. ., Dufresne, J. ., Feingold, G., Fiedler, S., Forster, P., Gettelman, A., Haywood, J. M., Lohmann, U., Malavelle, F., Mauritsen, T., McCoy, D. T., Myhre, G., Mülmenstädt, J., Neubauer, D., Possner, A., Rugenstein, M., Sato, Y., Schulz, M., Schwartz, S. E., Sourdeval, O., Storelvmo, T., Toll, V., Winker, D., and Stevens, B.: Bounding Global Aerosol Radiative Forcing of Climate Change, Reviews of Geophysics, 58, 2020.

Berry, E. and Mace, G. G.: Cloud properties and radiative effects of the Asian summer monsoon derived from A-Train data, Journal of Geophysical Research: Atmospheres, 119, 9492–9508, https://doi.org/10.1002/2014JD021458, 2014.

Beydoun, H., Caldwell, P. M., Hannah, W. M., and Donahue, A. S.: Dissecting Anvil Cloud Response to Sea Surface Warming, Geophysical Research Letters, 48, e2021GL094 049, https://doi.org/10.1029/2021GL094049, e2021GL094049 2021GL094049, 2021.

Blossey, P. N., Bretherton, C. S., Thornton, J. A., and Virts, K. S.: Locally Enhanced Aerosols Over a Shipping Lane Produce Convective Invigoration but Weak Overall Indirect Effects in Cloud-Resolving Simulations, Geophysical Research Letters, 45, 9305–9313, https://doi.org/10.1029/2018GL078682, 2018.

Bond, T. C., Doherty, S. J., Fahey, D. W., Forster, P. M., Berntsen, T., DeAngelo, B. J., Flanner, M. G., Ghan, S., Kärcher, B., Koch, D., et al.: Bounding the role of black car-

bon in the climate system: A scientific assessment, Journal of geophysical research: Atmospheres, 118, 5380–5552, 2013.

Bony, S., Stevens, B., Coppin, D., Becker, T., Reed, K. A., Voigt, A., and Medeiros, B.: Thermodynamic control of anvil cloud amount, Proceedings of the National Academy of Sciences, 113, 8927–8932, 2016.

Boucher, O. and Quaas, J.: Water vapour affects both rain and aerosol optical depth, Nature Geoscience, 6, 4–5, https://doi.org/10.1038/ngeo1692, 2013.

Boucher, O., Randall, D., Artaxo, P., Bretherton, C., Feingold, G., Forster, P., Kerminen, V.-M., Kondo, Y., Liao, H., Lohmann, U., Rasch, P., Satheesh, S. K., Sherwood, S., Stevens, B., and Zhang, X. Y.: Clouds and aerosols, in: Climate Change 2013: The Physical Science Basis. Contribution of Working Group I to the Fifth Assessment Report of the Intergovernmental Panel on Climate Change, pp. 571–657, Cambridge University Press, Cambridge, UK, https://doi.org/10.1017/CBO9781107415324.016, 2013.

Bourgeois, Q., Ekman, A. M. L., Igel, M. R., and Krejci, R.: Ubiquity and impact of thin mid-level clouds in the tropics, Nature Communications, 7, 12 432, https://doi.org/10.1038/ncomms12432, 2016.

Cecil, D. J., Buechler, D. E., and Blakeslee, R. J.: Gridded lightning climatology from TRMM-LIS and OTD: Dataset description, Atmospheric Research, 135-136, 404–414, https://doi.org/10.1016/j.atmosres.2012.06.028, 2014.

Chen, S. S. and Houze Jr, R. A.: Diurnal variation and life-cycle of deep convective systems over the tropical pacific warm pool, Quarterly Journal of the Royal Meteorological Society, 123, 357–388, https://doi.org/10.1002/qj.49712353806, 1997.

Chen, Y. and Del Genio, A. D.: Evaluation of tropical cloud regimes in observations and a general circulation model, Clim. Dyn., 32, 355–369, https://doi.org/10.1007/s00382-008-0386-6, 2009.

Cherian, R., Quaas, J., Salzmann, M., and Wild, M.: Pollution trends over Europe constrain global aerosol forcing as simulated by climate models, Geophysical Research Letters, 41, 2176–2181, https://doi.org/10.1002/2013GL058715, 2014.

Choi, Y.-S. and Ho, C.-H.: Radiative effect of cirrus with different optical properties over the tropics in MODIS and CERES observations, Geophysical Research Letters, 33, https://doi.org/10.1029/2006GL027403, 2006.

Christensen, M., Suzuki, K., Zambri, B., and Stephens, G.: Ship-track Observations of a Reduced Shortwave Aerosol Indirect Effect in Mixed-Phase Clouds, Geophysical Research Letters, 41, https://doi.org/10.1002/2014GL061320, 2014.

Christensen, M. W., Chen, Y.-C., and Stephens, G. L.: Aerosol indirect effect dictated by liquid clouds, Journal of Geophysical Research: Atmospheres, 121, 14,636–14,650, https://doi.org/https://doi.org/10.1002/2016JD025245, 2016.

Christian, H. J., Blakeslee, R. J., Boccippio, D. J., Boeck, W. L., Buechler, D. E., Driscoll, K. T., Goodman, S. J., Hall, J. M., Koshak, W. J., Mach, D. M., and Stewart, M. F.: Global frequency and distribution of lightning as observed from space by the Optical Transient Detector, Journal of Geophysical Research: Atmospheres, 108, ACL 4–1–ACL 4–15, https://doi.org/10.1029/2002JD002347, 2003.

Cotton, W. R. and Walko, R.: A Modeling Investigation of the Potential Impacts of Pollution Aerosols on Hurricane Harvey, Journal of the Atmospheric Sciences, 78, 2323 – 2338, https://doi.org/10.1175/JAS-D-20-0076.1, 2021.

Cronin, T. W. and Wing, A. A.: Clouds, circulation, and climate sensitivity in a radiative-convective equilibrium channel model, Journal of Advances in Modeling Earth Systems, 9, 2883–2905, 2017.

Dagan, G., Stier, P., Spill, G., Herbert, R., Heikenfeld, M., van den Heever, S. C., and Marinescu, P. J.: Boundary conditions representation can determine simulated

aerosol effects on convective cloud fields, Communications Earth & Environment, 3, 71, https://doi.org/10.1038/s43247-022-00399-5, 2022.

Dai, A.: Global precipitation and thunderstorm frequencies. Part II: Diurnal variations, Journal of Climate, 14, 1112–1128, 2001.

Dai, A., Giorgi, F., and Trenberth, K.: Observed and model simulated precipitation diurnal cycle over the contiguous United States, J. Geophys. Res, 104, 6377–6402, 1999.

Delanoë, J. and Hogan, R. J.: A variational scheme for retrieving ice cloud properties from combined radar, lidar, and infrared radiometer, Journal of Geophysical Research: Atmospheres, 113, https://doi.org/10.1029/2007JD009000, 2008.

Easterling, D. R. and Wehner, M. F.: Is the climate warming or cooling?, Geophysical Research Letters, 36, https://doi.org/10.1029/2009GL037810, 2009.

Evan, A. T., Heidinger, A. K., and Vimont, D. J.: Arguments against a physical long-term trend in global ISCCP cloud amounts, Geophysical Research Letters, 34, https://doi.org/10.1029/2006GL028083, 2007.

Fan, C., Wang, M., Rosenfeld, D., Zhu, Y., Liu, J., and Chen, B.: Strong Precipitation Suppression by Aerosols in Marine Low Clouds, Geophysical Research Letters, 47, e2019GL086 207, https://doi.org/10.1029/2019GL086207, e2019GL086207 2019GL086207, 2020.

Fan, J., Rosenfeld, D., Ding, Y., Leung, L. R., and Li, Z.: Potential aerosol indirect effects on atmospheric circulation and radiative forcing through deep convection, Geophysical Research Letters, 39, https://doi.org/10.1029/2012GL051851, 2012.

Fan, J., Leung, L. R., Rosenfeld, D., Chen, Q., Li, Z., Zhang, J., and Yan, H.: Microphysical effects determine macrophysical response for aerosol impacts on deep convective clouds, Proceedings of the National Academy of Sciences, 110, E4581–E4590, https://doi.org/10.1073/pnas.1316830110, 2013.

Fan, J., Rosenfeld, D., Zhang, Y., Giangrande, S. E., Li, Z., Machado, L. A. T., Martin, S. T., Yang, Y., Wang, J., Artaxo, P., Barbosa, H. M. J., Braga, R. C., Comstock, J. M., Feng, Z., Gao, W., Gomes, H. B., Mei, F., Pöhlker, C., Pöhlker, M. L., Pöschl, U., and de Souza, R. A. F.: Substantial convection and precipitation enhancements by ultrafine aerosol particles, Science, 359, 411–418, https://doi.org/10.1126/science.aan8461, 2018.

Feng, Z., Dong, X., Xi, B., McFarlane, S. A., Kennedy, A., Lin, B., and Minnis, P.: Life cycle of midlatitude deep convective systems in a Lagrangian framework, Journal of Geophysical Research: Atmospheres, 117, https://doi.org/10.1029/2012JD018362, 2012.

Forster, P., Storelvmo, T., Armour, K., Collins, W., Dufresne, J.-L., Frame, D., Lunt, D., Mauritsen, T., Palmer, M., Watanabe, M., Wild, M., and Zhang, H.: The Earth's Energy Budget, Climate Feedbacks, and Climate Sensitivity, in: Climate Change 2021: The Physical Science Basis. Contribution of Working Group I to the Sixth Assessment Report of the Intergovernmental Panel on Climate Change, edited by Masson-Delmotte, V., Zhai, P., Pirani, A., Connors, S. L., Péan, C., Berger, S., Caud, N., Chen, Y., Goldfarb, L., Gomis, M. I., Huang, M., Leitzell, K., Lonnoy, E., Matthews, J. B. R., Maycock, T. K., Waterfield, T., Yelekçi, O., Yu, R., and Zhou, B., book section 7, pp. 923–1054, Cambridge University Press, Cambridge, UK and New York, NY, USA, https://doi.org/10.1017/9781009157896.009, 2021.

Futyan, J. M., Russell, J. E., and Harries, J. E.: Cloud Radiative Forcing in Pacific, African, and Atlantic Tropical Convective Regions, Journal of Climate, 17, 3192 – 3202, https://doi.org/10.1175/1520-0442(2004)017¡3192:CRFIPA¿2.0.CO;2, 2004.

Garrett, T. J., Navarro, B. C., Twohy, C. H., Jensen, E. J., Baumgardner, D. G., Bui, P. T., Gerber, H., Herman, R. L., Heymsfield, A. J., Lawson, P., Minnis, P., Nguyen, L., Poellot, M., Pope, S. K., Valero, F. P. J., and Weinstock, E. M.: Evolution of a Florida

Cirrus Anvil, Journal of the Atmospheric Sciences, 62, 2352 – 2372, https://doi.org/10.1175/JAS3495.1, 2005.

Gasparini, B., Blossey, P. N., Hartmann, D. L., Lin, G., and Fan, J.: What Drives the Life Cycle of Tropical Anvil Clouds?, Journal of Advances in Modeling Earth Systems, 11, 2586–2605, https://doi.org/10.1029/2019MS001736, 2019.

Gasparini, B., Rasch, P. J., Hartmann, D. L., Wall, C. J., and Dütsch, M.: A Lagrangian Perspective on Tropical Anvil Cloud Lifecycle in Present and Future Climate, Journal of Geophysical Research: Atmospheres, 126, e2020JD033 487, https://doi.org/10.1029/2020JD033487, 2021.

Gasparini, B., Sokol, A. B., Wall, C. J., Hartmann, D. L., and Blossey, P. N.: Diurnal Differences in Tropical Maritime Anvil Cloud Evolution, Journal of Climate, 35, 1655 – 1677, https://doi.org/10.1175/JCLI-D-21-0211.1, 2022.

Gasparini, B., Sullivan, S. C., Sokol, A. B., Kärcher, B., Jensen, E., and Hartmann, D. L.: Opinion: Tropical cirrus – from micro-scale processes to climate-scale impacts, Atmospheric Chemistry and Physics, 23, 15 413–15 444, https://doi.org/10.5194/acp-23-15413-2023, 2023.

Gehlot, S. and Quaas, J.: Convection-Climate Feedbacks in the ECHAM5 General Circulation Model: Evaluation of Cirrus Cloud Life Cycles with ISCCP Satellite Data from a Lagrangian Trajectory Perspective, Journal of Climate, 25, 5241 – 5259, https://doi.org/10.1175/JCLI-D-11-00345.1, 2012.

Grandey, B. S., Rothenberg, D., Avramov, A., Jin, Q., Lee, H.-H., Liu, X., Lu, Z., Albani, S., and Wang, C.: Effective radiative forcing in the aerosol–climate model CAM5.3-MARC-ARG, Atmospheric Chemistry and Physics, 18, 15 783–15 810, https://doi.org/10.5194/acp-18-15783-2018, 2018.

Gryspeerdt, E., Stier, P., and Grandey, B. S.: Cloud fraction mediates the aerosol optical

depth-cloud top height relationship, Geophysical Research Letters, 41, 3622–3627, https://doi.org/10.1002/2014GL059524, 2014.

Gryspeerdt, E., Stier, P., White, B. A., and Kipling, Z.: Wet scavenging limits the detection of aerosol effects on precipitation, Atmospheric Chemistry and Physics, 15, 7557–7570, https://doi.org/10.5194/acp-15-7557-2015, 2015a.

Gryspeerdt, E., Stier, P., White, B. A., and Kipling, Z.: Wet scavenging limits the detection of aerosol effects on precipitation, Atmospheric Chemistry and Physics, 15, 7557–7570, https://doi.org/10.5194/acp-15-7557-2015, 2015b.

Gryspeerdt, E., Glassmeier, F., Feingold, G., Hoffmann, F., and Murray-Watson, R. J.: Observing short-timescale cloud development to constrain aerosol–cloud interactions, Atmospheric Chemistry and Physics, 22, 11 727–11 738, https://doi.org/10.5194/acp-22-11727-2022, 2022.

Hansen, J., Sato, M., and Ruedy, R.: Radiative forcing and climate response, Journal of Geophysical Research: Atmospheres, 102, 6831–6864, https://doi.org/10.1029/96JD03436, 1997.

Harrison, E. F., Minnis, P., Barkstrom, B. R., Ramanathan, V., Cess, R. D., and Gibson, G. G.: Seasonal variation of cloud radiative forcing derived from the Earth Radiation Budget Experiment, Journal of Geophysical Research: Atmospheres, 95, 18 687–18 703, https://doi.org/10.1029/JD095iD11p18687, 1990.

Hartmann, D. L. and Berry, S. E.: The balanced radiative effect of tropical anvil clouds, Journal of Geophysical Research: Atmospheres, 122, 5003–5020, https://doi.org/10.1002/2017JD026460, 2017.

Hartmann, D. L. and Larson, K.: An important constraint on tropical cloud-climate feedback, Geophysical research letters, 29, 12–1, 2002.

Hartmann, D. L., Ockert-Bell, M. E., and Michelsen, M. L.: The Effect of Cloud Type on Earth's Energy Balance: Global Analysis, Journal of Climate, 5, 1281 – 1304, https://doi.org/10.1175/1520-0442(1992)005¡1281:TEOCTO¿2.0.CO;2, 1992.

Hartmann, D. L., Holton, J. R., and Fu, Q.: The heat balance of the tropical tropopause, cirrus, and stratospheric dehydration, Geophysical Research Letters, 28, 1969–1972, https://doi.org/10.1029/2000GL012833, 2001a.

Hartmann, D. L., Moy, L. A., and Fu, Q.: Tropical Convection and the Energy Balance at the Top of the Atmosphere, Journal of Climate, 14, 4495 – 4511, https://doi.org/10.1175/1520-0442(2001)014¡4495:TCATEB¿2.0.CO;2, 2001b.

Hartmann, D. L., Gasparini, B., Berry, S. E., and Blossey, P. N.: The Life Cycle and Net Radiative Effect of Tropical Anvil Clouds, Journal of Advances in Modeling Earth Systems, 10, 3012–3029, https://doi.org/10.1029/2018MS001484, 2018.

Heintzenberg, J. and Charlson, R. J.: Deep Convective Clouds, pp. 197–215, 2009.

Herbert, R. and Stier, P.: Satellite observations of smoke–cloud–radiation interactions over the Amazon rainforest, Atmospheric Chemistry and Physics, 23, 4595–4616, https://doi.org/10.5194/acp-23-4595-2023, 2023.

Herbert, R., Stier, P., and Dagan, G.: Isolating Large-Scale Smoke Impacts on Cloud and Precipitation Processes Over the Amazon With Convection Permitting Resolution, Journal of Geophysical Research: Atmospheres, 126, e2021JD034 615, https://doi.org/https://doi.org/10.1029/2021JD034615, e2021JD034615 2021JD034615, 2021.

Hersbach, H., Bell, B., Berrisford, P., Biavati, G., Horányi, A., Muñoz Sabater, J., Nicolas, J., Peubey, C., Radu, R., Rozum, I., Schepers, D., Simmons, A., Soci, C., Dee, D., and Thépaut, J.-N.: ERA5 hourly data on pressure levels from 1959 to present., https://doi.org/10.24381/cds.bd0915c6, 2018.

Howard, L.: I. On the modifications of clouds, and on the principles of their production, suspension, and destruction; being the substance of an essay read before the Askesian Society in the session 1802-3, The Philosophical Magazine, 17, 5–11, https://doi.org/10.1080/14786440308676365, 1803.

Igel, A. L. and van den Heever, S. C.: Invigoration or Enervation of Convective Clouds by Aerosols?, Geophysical Research Letters, 48, e2021GL093 804, https://doi.org/10.1029/2021GL093804, e2021GL093804 2021GL093804, 2021.

Jensen, E. J., van den Heever, S. C., and Grant, L. D.: The Life Cycles of Ice Crystals Detrained From the Tops of Deep Convection, Journal of Geophysical Research: Atmospheres, 123, 9624–9634, https://doi.org/10.1029/2018JD028832, 2018.

Jensen, E. J., Pan, L. L., Honomichl, S., Diskin, G. S., KrÃ€mer, M., Spelten, N., GÃŒnther, G., Hurst, D. F., Fujiwara, M., Vamel, H., Selkirk, H. B., Suzuki, J., Schwartz, M. J., and Smith, J. B.: Assessment of Observational Evidence for Direct Convective Hydration of the Lower Stratosphere, Journal of Geophysical Research: Atmospheres, 125, e2020JD032 793, https://doi.org/ https://doi.org/10.1029/2020JD032793, e2020JD032793 10.1029/2020JD032793, 2020.

Jiang, H., Xue, H., Teller, A., Feingold, G., and Levin, Z.: Aerosol effects on the lifetime of shallow cumulus, Geophysical Research Letters, 33, https://doi.org/10.1029/2006GL026024, 2006.

Jing, X. and Suzuki, K.: The Impact of Process-Based Warm Rain Constraints on the Aerosol Indirect Effect, Geophysical Research Letters, 45, 10,729–10,737, https://doi.org/10.1029/2018GL079956, 2018.

Jones, W. K., Stengel, M., and Stier, P.: A Lagrangian perspective on the lifecycle and cloud radiative effect of deep convective clouds over Africa, Atmospheric Chemistry and Physics, 24, 5165–5180, https://doi.org/10.5194/acp-24-5165-2024, 2024.

Katsman, C. A. and van Oldenborgh, G. J.: Correction to "Tracing the upper ocean's 'missing heat'", Geophysical Research Letters, 38, https://doi.org/10.1029/2011GL049834, 2011.

Kaufmann, R. K., Kauppi, H., Mann, M. L., and Stock, J. H.: Reconciling anthropogenic climate change with observed temperature 1998–2008, Proceedings of the National Academy of Sciences, 108, 11 790–11 793, 2011.

Klein, S. A. and Jakob, C.: Validation and Sensitivities of Frontal Clouds Simulated by the ECMWF Model, Monthly Weather Review, 127, 2514 – 2531, https://doi.org/10.1175/1520-0493(1999)127¡2514:VASOFC¿2.0.CO;2, 1999.

Knapp, K. R., Ansari, S., Bain, C. L., Bourassa, M. A., Dickinson, M. J., Funk, C., Helms, C. N., Hennon, C. C., Holmes, C. D., Huffman, G. J., Kossin, J. P., Lee, H.-T., Loew, A., and Magnusdottir, G.: Globally Gridded Satellite Observations for Climate Studies, Bulletin of the American Meteorological Society, 92, 893 – 907, https://doi.org/10.1175/2011BAMS3039.1, 2011.

Knapp, K. R., Young, A. H., Semunegus, H., Inamdar, A. K., and Hankins, W.: Adjusting ISCCP Cloud Detection to Increase Consistency of Cloud Amount and Reduce Artifacts, Journal of Atmospheric and Oceanic Technology, 38, 155 – 165, https://doi.org/10.1175/JTECH-D-20-0045.1, 2021.

Koren, I., Kaufman, Y. J., Rosenfeld, D., Remer, L. A., and Rudich, Y.: Aerosol invigoration and restructuring of Atlantic convective clouds, Geophysical Research Letters, 32, https://doi.org/10.1029/2005GL023187, 2005.

Koren, I., Martins, J. V., Remer, L. A., and Afargan, H.: Smoke Invigoration Versus Inhibition of Clouds over the Amazon, Science, 321, 946–949, https://doi.org/10.1126/science.1159185, 2008.

Koren, I., Feingold, G., and Remer, L. A.: The invigoration of deep convective clouds over the Atlantic: aerosol effect, meteorology or retrieval artifact?, Atmospheric

Chemistry and Physics, 10, 8855–8872, https://doi.org/10.5194/acp-10-8855-2010, 2010a.

Koren, I., Remer, L. A., Altaratz, O., Martins, J. V., and Davidi, A.: Aerosol-induced changes of convective cloud anvils produce strong climate warming, Atmospheric Chemistry and Physics, 10, 5001–5010, https://doi.org/10.5194/acp-10-5001-2010, 2010b.

Koren, I., Dagan, G., and Altaratz, O.: From aerosol-limited to invigoration of warm convective clouds, Science, 344, 1143–1146, https://doi.org/10.1126/science.1252595, 2014.

Kosaka, Y. and Xie, S.-P.: Recent global-warming hiatus tied to equatorial Pacific surface cooling, Nature, 501, 403–407, https://doi.org/10.1038/nature12534, 2013.

Krishna, U. V. M., Das, S. K., Deshpande, S. M., and Pandithurai, G.: Physical processes controlling the diurnal cycle of convective storms in the Western Ghats, Scientific Reports, 11, 14 103, https://doi.org/10.1038/s41598-021-93173-0, 2021.

Kristjánsson, J. E., Iversen, T., Kirkevåg, A., Seland, , and Debernard, J.: Response of the climate system to aerosol direct and indirect forcing: Role of cloud feedbacks, Journal of Geophysical Research: Atmospheres, 110, https://doi.org/10.1029/2005JD006299, 2005.

Krämer, M., Rolf, C., Luebke, A., Afchine, A., Spelten, N., Costa, A., Meyer, J., Zöger, M., Smith, J., Herman, R. L., Buchholz, B., Ebert, V., Baumgardner, D., Borrmann, S., Klingebiel, M., and Avallone, L.: A microphysics guide to cirrus clouds – Part 1: Cirrus types, Atmospheric Chemistry and Physics, 16, 3463–3483, https://doi.org/10.5194/acp-16-3463-2016, 2016.

Lebo, Z. J. and Seinfeld, J. H.: Theoretical basis for convective invigoration due to increased aerosol concentration, Atmospheric Chemistry and Physics, 11, 5407–5429, https://doi.org/10.5194/acp-11-5407-2011, 2011.

Li, Z., Niu, F., Fan, J., Liu, Y., Rosenfeld, D., and Ding, Y.: Long-term impacts of aerosols on the vertical development of clouds and precipitation, Nature Geoscience, 4, 888–894, https://doi.org/10.1038/ngeo1313, 2011.

Lin, J. C., Matsui, T., Pielke Sr., R. A., and Kummerow, C.: Effects of biomass-burning-derived aerosols on precipitation and clouds in the Amazon Basin: a satellite-based empirical study, Journal of Geophysical Research: Atmospheres, 111, https://doi.org/10.1029/2005JD006884, 2006.

Lindsey, D. T. and Fromm, M.: Evidence of the cloud lifetime effect from wildfire-induced thunderstorms, Geophysical Research Letters, 35, https://doi.org/10.1029/2008GL035680, 2008.

Liu, C., Zipser, E. J., and Nesbitt, S. W.: Global Distribution of Tropical Deep Convection: Different Perspectives from TRMM Infrared and Radar Data, Journal of Climate, 20, 489 – 503, https://doi.org/10.1175/JCLI4023.1, 2007.

Loeb, N. G., Kato, S., Loukachine, K., and Manalo-Smith, N.: Angular Distribution Models for Top-of-Atmosphere Radiative Flux Estimation from the Clouds and the Earth's Radiant Energy System Instrument on the Terra Satellite. Part I: Methodology, Journal of Atmospheric and Oceanic Technology, 22, 338 – 351, https://doi.org/10.1175/JTECH1712.1, 2005.

Lohmann, U., Lüönd, F., and Mahrt, F.: An Introduction to Clouds: From the Microscale to Climate, Cambridge University Press, 2016.

Lopez-Bravo, C., Vincent, C. L., Huang, Y., and Lane, T. P.: The Diurnal Cycle of Rainfall and Deep Convective Clouds Around Sumatra and the Associated MJO-Induced Variability During Austral Summer in Himawari-8, Journal of Geophysical Research: Atmospheres, 128, e2023JD039 132, https://doi.org/10.1029/2023JD039132, e2023JD039132 2023JD039132, 2023.

Luo, Z. and Rossow, W. B.: Characterizing Tropical Cirrus Life Cycle, Evolution, and Interaction with Upper-Tropospheric Water Vapor Using Lagrangian Trajectory Analysis of Satellite Observations, Journal of Climate, 17, 4541 – 4563, https://doi.org/10.1175/3222.1, 2004.

Mace, G.: Level 2 GEOPROF product process description and interface control document, Coop. Inst. for Res. in the Atmos., Fort Collins, Colo, 2004.

Mace, G. and Wrenn, F.: Evaluation of the Hydrometeor Layers in the East and West Pacific within ISCCP Cloud-Top Pressure-Optical Depth Bins Using Merged-CloudSatandCALIPSOData, Journal of Climate, 26, 9429–9444, https://doi.org/10.1175/JCLI-D-12-00207.1, 2013.

Mace, G. G., Deng, M., Soden, B., and Zipser, E.: Association of Tropical Cirrus in the 10–15-km Layer with Deep Convective Sources: An Observational Study Combining Millimeter Radar Data and Satellite-Derived Trajectories, Journal of the Atmospheric Sciences, 63, 480–503, https://doi.org/10.1175/JAS3627.1, 2006.

Massie, S., Gettelman, A., Randel, W., and Baumgardner, D.: Distribution of tropical cirrus in relation to convection, Journal of Geophysical Research: Atmospheres, 107, AAC 19–1–AAC 19–16, https://doi.org/10.1029/2001JD001293, 2002.

McCoy, D. T., Bender, F. A.-M., Mohrmann, J. K. C., Hartmann, D. L., Wood, R., and Grosvenor, D. P.: The global aerosol-cloud first indirect effect estimated using MODIS, MERRA, and AeroCom, Journal of Geophysical Research: Atmospheres, 122, 1779–1796, https://doi.org/https://doi.org/10.1002/2016JD026141, 2017.

Medhaug, I., Stolpe, M. B., Fischer, E. M., and Knutti, R.: Reconciling controversies about the 'global warming hiatus', Nature, 545, 41–47, https://doi.org/10.1038/nature22315, 2017.

Meehl, G. A., Arblaster, J. M., Fasullo, J. T., Hu, A., and Trenberth, K. E.: Model-based

evidence of deep-ocean heat uptake during surface-temperature hiatus periods, Nature Climate Change, 1, 360–364, https://doi.org/10.1038/nclimate1229, 2011.

Murphy, D. M., Solomon, S., Portmann, R. W., Rosenlof, K. H., Forster, P. M., and Wong, T.: An observationally based energy balance for the Earth since 1950, Journal of Geophysical Research: Atmospheres, 114, https://doi.org/10.1029/2009JD012105, 2009.

Myhre, G., Stordal, F., Restad, K., and Isaksen, I. S. A.: Estimation of the direct radiative forcing due to sulfate and soot aerosols, Tellus B: Chemical and Physical Meteorology, 50, 463–477, https://doi.org/10.3402/tellusb.v50i5.16230, 1998.

NASA/LARC/SD/ASDC: CERES and GEO-Enhanced TOA, Within-Atmosphere and Surface Fluxes, Clouds and Aerosols 1-Hourly Terra-Aqua Edition4A, URL 10.5067/TERRA+AQUA/CERES/SYN1DEG-1HOUR$_L$3.004A, 2017.

Norris, J. R. and Evan, A. T.: Empirical Removal of Artifacts from the ISCCP and PATMOS-x Satellite Cloud Records, Journal of Atmospheric and Oceanic Technology, 32, 691 – 702, https://doi.org/10.1175/JTECH-D-14-00058.1, 2015.

Penner, J., Chuang, C., and Grant, K.: Climate forcing by carbonaceous and sulfate aerosols, Climate Dynamics, 14, 839–851, https://doi.org/10.1007/s003820050259, cited By 264, 1998.

Peters, J. M., Lebo, Z. J., Chavas, D. R., and Su, C.-Y.: Entrainment Makes Pollution More Likely to Weaken Deep Convective Updrafts Than Invigorate Them, Geophysical Research Letters, 50, e2023GL103 314, https://doi.org/10.1029/2023GL103314, e2023GL103314 2023GL103314, 2023.

Pincus, R. and Baker, M. B.: Effect of precipitation on the albedo susceptibility of clouds in the marine boundary layer, Nature, 372, 250–252, https://doi.org/10.1038/372250a0, 1994.

Pincus, R., Baker, M. B., and Bretherton, C. S.: What Controls Stratocumulus Radiative Properties? Lagrangian Observations of Cloud Evolution, Journal of the Atmospheric Sciences, 54, 2215 – 2236, https://doi.org/10.1175/1520-0469(1997)054¡2215:WCSRPL¿2.0.CO;2, 1997.

Pincus, R., Platnick, S., Ackerman, S. A., Hemler, R. S., and Hofmann, R. J. P.: Reconciling Simulated and Observed Views of Clouds: MODIS, ISCCP, and the Limits of Instrument Simulators, Journal of Climate, 25, 4699 – 4720, https://doi.org/10.1175/JCLI-D-11-00267.1, 2012.

Platnick, S. and Twomey, S.: Determining the Susceptibility of Cloud Albedo to Changes in Droplet Concentration with the Advanced Very High Resolution Radiometer, Journal of Applied Meteorology and Climatology, 33, 334 – 347, https://doi.org/10.1175/1520-0450(1994)033¡0334:DTSOCA¿2.0.CO;2, 1994.

Quaas, J., Stevens, B., Stier, P., and Lohmann, U.: Interpreting the cloud cover â aerosol optical depth relationship found in satellite data using a general circulation model, Atmospheric Chemistry and Physics, 10, 6129–6135, https://doi.org/10.5194/acp-10-6129-2010, 2010.

Ramanathan, V., Cess, R. D., Harrison, E. F., Minnis, P., Barkstrom, B. R., Ahmad, E., and Hartmann, D.: Cloud-Radiative Forcing and Climate: Results from the Earth Radiation Budget Experiment, Science, 243, 57–63, https://doi.org/10.1126/science.243.4887.57, 1989.

Redington, A. L. and Derwent, R. G.: Calculation of sulphate and nitrate aerosol concentrations over Europe using a Lagrangian dispersion model, Atmospheric Environment, 36, 4425–4439, https://doi.org/10.1016/S1352-2310(02)00420-X, 2002.

Remer, L. A., Kaufman, Y. J., TanrÃ©, D., Mattoo, S., Chu, D. A., Martins, J. V., Li, R.-R., Ichoku, C., Levy, R. C., Kleidman, R. G., Eck, T. F., Vermote, E., and Holben,

B. N.: The MODIS Aerosol Algorithm, Products, and Validation, Journal of the Atmospheric Sciences, 62, 947 – 973, https://doi.org/10.1175/JAS3385.1, 2005.

Remer, L. A., Kleidman, R. G., Levy, R. C., Kaufman, Y. J., Tanré, D., Mattoo, S., Martins, J. V., Ichoku, C., Koren, I., Yu, H., and Holben, B. N.: Global aerosol climatology from the MODIS satellite sensors, Journal of Geophysical Research: Atmospheres, 113, https://doi.org/10.1029/2007JD009661, 2008.

Riihimaki, L. D., McFarlane, S. A., Liang, C., Massie, S. T., Beagley, N., and Toth, T. D.: Comparison of methods to determine Tropical Tropopause Layer cirrus formation mechanisms, Journal of Geophysical Research: Atmospheres, 117, https://doi.org/10.1029/2011JD016832, 2012.

Riley, E. M., Mapes, B. E., and Tulich, S. N.: Clouds Associated with the Madden-Julian Oscillation: A New Perspective from CloudSat, Journal of the Atmospheric Sciences, 68, 3032 – 3051, https://doi.org/10.1175/JAS-D-11-030.1, 2011.

Rolph, G., Stein, A., and Stunder, B.: Real-time Environmental Applications and Display sYstem: READY, Environmental Modelling and Software, 95, 210–228, https://doi.org/10.1016/j.envsoft.2017.06.025, 2017.

Rosenfeld, D., Lohmann, U., Raga, G. B., O'Dowd, C. D., Kulmala, M., Fuzzi, S., Reissell, A., and Andreae, M. O.: Flood or Drought: How Do Aerosols Affect Precipitation?, Science, 321, 1309–1313, https://doi.org/10.1126/science.1160606, 2008.

Rosenfeld, D., Sherwood, S., Wood, R., and Donner, L.: Climate Effects of Aerosol-Cloud Interactions, Science, 343, 379–380, https://doi.org/10.1126/science.1247490, 2014.

Rossow, W., Golea, V., Walker, A., Knapp, K., Young, A., Hankins, B., and Inamdar, A.: International Satellite Cloud Climatology Project (ISCCP) Climate Data Record, H-Series, https://doi.org/10.7289/V5QZ281S, 2017.

Rossow, W. B. and Garder, L. C.: Cloud Detection Using Satellite Measurements of Infrared and Visible Radiances for ISCCP, Journal of Climate, 6, 2341 – 2369, https://doi.org/10.1175/1520-0442(1993)006¡2341:CDUSMO¿2.0.CO;2, 1993.

Rossow, W. B. and Schiffer, R. A.: Advances in Understanding Clouds from ISCCP, Bulletin of the American Meteorological Society, 80, 2261 – 2288, https://doi.org/10.1175/1520-0477(1999)080¡2261:AIUCFI¿2.0.CO;2, 1999.

Ruppert, J. H. and Hohenegger, C.: Diurnal Circulation Adjustment and Organized Deep Convection, Journal of Climate, 31, 4899 – 4916, https://doi.org/10.1175/JCLI-D-17-0693.1, 2018.

Salathé, E. P. and Hartmann, D. L.: A Trajectory Analysis of Tropical Upper-Tropospheric Moisture and Convection, Journal of Climate, 10, 2533–2547, URL http://www.jstor.org/stable/26243410, 1997.

Salomonson, V., Barnes, W., Maymon, P., Montgomery, H., and Ostrow, H.: MODIS: advanced facility instrument for studies of the Earth as a system, IEEE Transactions on Geoscience and Remote Sensing, 27, 145–153, https://doi.org/10.1109/36.20292, 1989.

Schiffer, R. A. and Rossow, W. B.: The International Satellite Cloud Climatology Project (ISCCP): The first project of the World Climate Research Programme, Bulletin of the American Meteorological Society, 64, 779–784, 1983.

Sokol, A. B. and Hartmann, D. L.: Tropical Anvil Clouds: Radiative Driving Toward a Preferred State, Journal of Geophysical Research: Atmospheres, 125, e2020JD033 107, https://doi.org/10.1029/2020JD033107, e2020JD033107 10.1029/2020JD033107, 2020.

Solomon, S., Rosenlof, K. H., Portmann, R. W., Daniel, J. S., Davis, S. M., Sanford, T. J., and Plattner, G.-K.: Contributions of stratospheric water vapor to decadal changes in the rate of global warming, science, 327, 1219–1223, 2010.

Sourdeval, O., Gryspeerdt, E., Krämer, M., Goren, T., Delanoë, J., Afchine, A., Hemmer, F., and Quaas, J.: Ice crystal number concentration estimates from lidar–radar satellite remote sensing – Part 1: Method and evaluation, Atmospheric Chemistry and Physics, 18, 14 327–14 350, https://doi.org/10.5194/acp-18-14327-2018, 2018.

Stephens, G., Winker, D., Pelon, J., Trepte, C., Vane, D., Yuhas, C., LâEcuyer, T., and Lebsock, M.: CloudSat and CALIPSO within the A-Train: Ten Years of Actively Observing the Earth System, Bulletin of the American Meteorological Society, 99, 569 – 581, https://doi.org/10.1175/BAMS-D-16-0324.1, 2018.

Stevens, B.: Rethinking the Lower Bound on Aerosol Radiative Forcing, Journal of Climate, 28, 4794 – 4819, https://doi.org/10.1175/JCLI-D-14-00656.1, 2015.

Stevens, B. and Feingold, G.: Untangling aerosol effects on clouds and precipitation in a buffered system, Nature, 461, 607–613, https://doi.org/10.1038/nature08281, 2009.

Stier, P.: Limitations of passive remote sensing to constrain global cloud condensation nuclei, Atmospheric Chemistry and Physics, 16, 6595–6607, https://doi.org/10.5194/acp-16-6595-2016, 2016.

Storer, R. L., van den Heever, S. C., and L'Ecuyer, T. S.: Observations of aerosol-induced convective invigoration in the tropical east Atlantic, Journal of Geophysical Research: Atmospheres, 119, 3963–3975, https://doi.org/10.1002/2013JD020272, 2014.

Su, H., Jiang, J. H., Neelin, J. D., Shen, T. J., Zhai, C., Yue, Q., Wang, Z., Huang, L., Choi, Y.-S., Stephens, G. L., et al.: Tightening of tropical ascent and high clouds key to precipitation change in a warmer climate, Nature communications, 8, 15 771, 2017.

Takahashi, H., Luo, Z. J., and Stephens, G. L.: Level of neutral buoyancy, deep convective outflow, and convective core: New perspectives based on 5years of

CloudSat data, Journal of Geophysical Research: Atmospheres, 122, 2958–2969, https://doi.org/10.1002/2016JD025969, 2017.

Tao, W.-K., Chen, J.-P., Li, Z., Wang, C., and Zhang, C.: Impact of aerosols on convective clouds and precipitation, Reviews of Geophysics, 50, https://doi.org/10.1029/2011RG000369, 2012.

Textor, C., Schulz, M., Guibert, S., Kinne, S., Balkanski, Y., Bauer, S., Berntsen, T., Berglen, T., Boucher, O., Chin, M., Dentener, F., Diehl, T., Easter, R., Feichter, H., Fillmore, D., Ghan, S., Ginoux, P., Gong, S., Grini, A., Hendricks, J., Horowitz, L., Huang, P., Isaksen, I., Iversen, I., Kloster, S., Koch, D., Kirkevåg, A., Kristjansson, J. E., Krol, M., Lauer, A., Lamarque, J. F., Liu, X., Montanaro, V., Myhre, G., Penner, J., Pitari, G., Reddy, S., Seland, Ø., Stier, P., Takemura, T., and Tie, X.: Analysis and quantification of the diversities of aerosol life cycles within AeroCom, Atmospheric Chemistry and Physics, 6, 1777–1813, https://doi.org/10.5194/acp-6-1777-2006, 2006.

Thornton, J. A., Virts, K. S., Holzworth, R. H., and Mitchell, T. P.: Lightning enhancement over major oceanic shipping lanes, Geophysical Research Letters, 44, 9102–9111, https://doi.org/10.1002/2017GL074982, 2017.

Toll, V., Christensen, M., Quaas, J., and Bellouin, N.: Weak average liquid-cloud-water response to anthropogenic aerosols, Nature, 572, 51–55, 2019.

Tompkins, A. M. and Giuseppe, F. D.: An Interpretation of Cloud Overlap Statistics, Journal of the Atmospheric Sciences, 72, 2877 – 2889, https://doi.org/10.1175/JAS-D-14-0278.1, 2015.

Tselioudis, G., Rossow, W. B., Jakob, C., Remillard, J., Tropf, D., and Zhang, Y.: Evaluation of Clouds, Radiation, and Precipitation in CMIP6 Models Using Global Weather States Derived from ISCCP-H Cloud Property Data, Journal of Climate, 34, 7311 – 7324, https://doi.org/10.1175/JCLI-D-21-0076.1, 2021.

Twomey, S.: Pollution and the planetary albedo, Atmospheric Environment (1967), 8, 1251–1256, https://doi.org/10.1016/0004-6981(74)90004-3, 1974.

Varble, A. C., Igel, A. L., Morrison, H., Grabowski, W. W., and Lebo, Z. J.: Opinion: A critical evaluation of the evidence for aerosol invigoration of deep convection, Atmospheric Chemistry and Physics, 23, 13 791–13 808, https://doi.org/10.5194/acp-23-13791-2023, 2023.

Vaughan, M., Pitts, M., Trepte, C., Winker, D., Getzewich, B., Tackett, J., Cai, X., Detweiler, P., Garnier, A., Kar, J., et al.: Cloud-Aerosol LIDAR Infrared Pathfinder Satellite Observations (CALIPSO)-Data Management System: Data Products Catalog V4. 95, Tech. rep., 2023.

Veals, P. G., Varble, A. C., Russell, J. O. H., Hardin, J. C., and Zipser, E. J.: Indications of a Decrease in the Depth of Deep Convective Cores with Increasing Aerosol Concentration during the CACTI Campaign, Journal of the Atmospheric Sciences, 79, 705 – 722, https://doi.org/10.1175/JAS-D-21-0119.1, 2022.

Wall, C. J. and Hartmann, D. L.: Balanced Cloud Radiative Effects Across a Range of Dynamical Conditions Over the Tropical West Pacific, Geophysical Research Letters, 45, 11,490–11,498, https://doi.org/10.1029/2018GL080046, 2018.

Wang, C.: Impact of anthropogenic absorbing aerosols on clouds and precipitation: A review of recent progresses, Atmospheric Research, 122, 237–249, https://doi.org/10.1016/j.atmosres.2012.11.005, 2013.

Wapler, K. and Lane, T. P.: A case of offshore convective initiation by interacting land breezes near Darwin, Australia, Meteorology and Atmospheric Physics, 115, 123–137, 2012.

Wielicki, B. A., Barkstrom, B. R., Harrison, E. F., Lee, R. B., Smith, G. L., and Cooper, J. E.: Clouds and the Earth's Radiant Energy System (CERES): An Earth Observing

System Experiment, Bulletin of the American Meteorological Society, 77, 853–868, https://doi.org/10.1175/1520-0477(1996)077¡0853:CATERE¿2.0.CO;2, 1996.

Williams, E., Rosenfeld, D., Madden, N., Gerlach, J., Gears, N., Atkinson, L., Dunnemann, N., Frostrom, G., Antonio, M., Biazon, B., Camargo, R., Franca, H., Gomes, A., Lima, M., Machado, R., Manhaes, S., Nachtigall, L., Piva, H., Quintiliano, W., Machado, L., Artaxo, P., Roberts, G., Renno, N., Blakeslee, R., Bailey, J., Boccippio, D., Betts, A., Wolff, D., Roy, B., Halverson, J., Rickenbach, T., Fuentes, J., and Avelino, E.: Contrasting convective regimes over the Amazon: Implications for cloud electrification, Journal of Geophysical Research: Atmospheres, 107, LBA 50–1–LBA 50–19, https://doi.org/10.1029/2001JD000380, 2002.

Xue, H. and Feingold, G.: Large-Eddy Simulations of Trade Wind Cumuli: Investigation of Aerosol Indirect Effects, Journal of the Atmospheric Sciences, 63, 1605 – 1622, https://doi.org/10.1175/JAS3706.1, 2006.

Yang, G.-Y. and Slingo, J.: The Diurnal Cycle in the Tropics, Monthly Weather Review, 129, 784 – 801, https://doi.org/10.1175/1520-0493(2001)129¡0784:TDCITT¿2.0.CO;2, 2001.

Yu, H., Fu, R., Dickinson, R. E., Zhang, Y., Chen, M., and Wang, H.: Interannual variability of smoke and warm cloud relationships in the Amazon as inferred from MODIS retrievals, Remote Sensing of Environment, 111, 435–449, https://doi.org/ https://doi.org/10.1016/j.rse.2007.04.003, 2007.

Zang, L., Rosenfeld, D., Pan, Z., Mao, F., Zhu, Y., Lu, X., and Gong, W.: Observing Aerosol Primary Convective Invigoration and Its Meteorological Feedback, Geophysical Research Letters, 50, e2023GL104 151, https://doi.org/ 10.1029/2023GL104151, e2023GL104151 2023GL104151, 2023.

Zhang, J., Zhao, B., Liu, X., Lin, G., Jiang, Z., Wu, C., and Zhao, X.: Effects of Different Types of Aerosols on Deep Convective Clouds and Anvil Cirrus, Geophys-

ical Research Letters, 49, e2022GL099 478, https://doi.org/10.1029/2022GL099478, e2022GL099478 2022GL099478, 2022.

Zuidema, P.: Convective clouds over the Bay of Bengal, Monthly Weather Review, 131, 780–798, 2003.